8-1-2008

Structure-property quantification and modeling related to crashworthiness

Isha C. Carrasquel Romero

STRUCTURE-PROPERTY QUANTIFICATION AND MODELING

RELATED TO CRASHWORTHINESS

By

Isha C. Carrasquel Romero

A Thesis
Submitted to the Faculty of
Mississippi State University
in Partial Fulfillment of the Requirements
for the Degree of Master of Science
in Mechanical Engineering
in the Department of Mechanical Engineering

Mississippi State, Mississippi

August, 2008

STRUCTURE-PROPERTY QUANTIFICATION AND MODELING

RELATED TO CRASHWORTHINESS

By

Isha C. Carrasquel Romero

Approved:

_____ Mark F. Horstemeyer Center for Advanced Vehicular Systems Chair in Computational Solid Mechanics Professor of Mechanical Engineering (Major Professor)	_____ John T. Berry E. P. Coleman Professor of Mechanical Engineering (Committee Member)
_____ Douglas Bammann Professor of Mechanical Engineering (Committee Member)	_____ Louay M. Chamra Professor of Mechanical Engineering and Department Head
_____ Steven R. Daniewics Professor and Graduate Coordinator Department of Mechanical Engineering	_____ Sarah A. Rajala Dean of the College of Engineering

Name: Isha Carrasquel

Date of Degree: August 9, 2008

Institution: Mississippi State University

Major Field: Mechanical Engineering

Major Professor: Dr. Mark F. Horstemeyer

Title of Study: STRUCTURE-PROPERTY QUANTIFICATION AND MODELING RELATED TO CRASHWORTHINESS

Pages in Study: 107

Candidate for Degree of Masters of Science

The objective of this study is to characterize critical component structure-properties on a Dodge Neon for material response refinement in crashworthiness simulations. Crashworthiness simulations using full-scale finite element (FE) vehicle models are an important part of vehicle design. According to the National Highway Traffic Safety Administration (NHTSA), there were over six million vehicle crashes in the United States during 2004, claming lives of more than 40,000 people.

Crashworthiness simulations on a detailed FE model of a 1996 Plymouth/Dodge Neon were conducted on the NHTSA for different impact crash scenarios. The top-ten energy-absorbing components of the vehicle were determined. Material was extracted from the as-built vehicle and microstructural analyses were conducted. Tension tests at different temperatures and strain rates were performed as well as microhardness tests. Different microstructural spatial clustering and mechanical properties were found for diverse vehicle components. A plasticity model based on microstructure was used to predict the material response of the front bumper.

DEDICATION

I would like to dedicate this research to my grandmother, who has always guided me and supported me throughout my life.

AKNOWLEDGEMENTS

I would like to thank God for guiding me through this journey and for the upcoming experiences He will bring to my life. I would like to thank Dr. Mark F. Horstemeyer, my advisor, for helping me coming to Mississippi State University to pursue my master's degree, and for his guidance throughout this process. I would like to extend special thanks to Dr. John Berry and Dr. Douglas Bammann, for sharing part of their knowledge with me and for helping me understand important aspects that made this Thesis possible. I would also like to thank Dr. Haitham El Kadiri, Dr. Ricolino Carino, Dr. Adrian Pascu, Kiran Solanki and Paul Allison for their help on this research. Additionally, I would like to thank the Center for Advanced Vehicular Systems for their space, financial support and resources. Finally, I would like to thank my family and my friends for their support and trust on me.

TABLE OF CONTENTS

LIST OF TABLES

LIST OF FIGURES

CHAPTER I

INTRODUCTION

Vehicle safety (crashworthiness) and vehicle weight are essential attributes for current vehicle design. In order to meet national safety standards and customer needs, vehicle designers are challenged to improve the crashworthiness of vehicle's structures and reduce weight for energy conservation and emission reduction [Zaouk et al., 1999].

With the purpose of evaluating crashworthiness, previous efforts focused on physical tests. Presently, computational advances allow simulating crash scenarios with the aid of finite element analysis (FEA). The use of finite elements is an attractive alternative for the automotive industry. It can be used to reduce design cycles and to predict an automobile's crashworthiness. Finite element simulations make it easy to vary different parameters and observe the effects on the vehicle in conditions that are otherwise unavailable with physical tests [Van Slycken, 2006].

In order to establish a base line, the analysis data must be compared with physical crash data. To produce accurate analysis results, precise representation of material behavior should be taken into account [Zaouk et al., 1999]. However, most crash simulations do not incorporate these structure property relations of the as-built vehicle into the FEA model.

Recent advances in research and experimentation have yielded several constitutive models that better describe damage and ensuing failure of materials [Bammann et al., 1993]. These models can now be used in finite element analysis to produce results that are more comparable to the actual collected crash data. The primary analysis methods of yesterday are more simplistic and will yield results with more percentage error.

In this research work, a microstructure-based Internal State Variable (ISV) plasticity-damage model was used, first introduced by Bammann and Aifantis [Bammann, 1984; Bammann and Aifantis, 1988]. This model was later modified by Horstemeyer and Gokhale [1999] when they included damage evolution analysis and implemented it into a finite element code [Horstemeyer et al., 2000] based on void nucleation coalescence proposed in Horstemeyer et al. [2000], and void growth by McClintock [1968] and Cocks and Ashby [1982].

A detailed finite element model of a 1996 Plymouth/Dodge Neon was developed at the National Highway Traffic Safety Administration (NHTSA) National Crash Analysis Center as part of the Partnership for a New Generation of Vehicles (PNGV) program. This automobile represents the sub-compact vehicle class. Improvement in the vehicle FE modeling performance is crucial for development of better occupant safety designs [Zaouk et al., 1999].

Zaouk et al. modified the Neon model by including experimental tension data from the engineering stress-strain curves. The true stress-strain curves for specific components were generated to be used in LS-Dyna with type 24 elements (sheet metal). No microstructure properties were included in the mentioned document.

The characterization of the microstructure-property relations of components is vital for implementation into large scale FE codes using a plasticity-damage model. These relations along with application of multi-objective and multi-level optimization techniques will enable industry to develop better design parameters.

A 1995 Dodge Neon, with the same structural design as the 1996 Plymouth Neon model developed by the NTHSA was purchased by the Center for Advanced Vehicular Systems (CAVS) through a local dealership. The vehicle was disassembled and material specimens were extracted from components with more energy absorption. These components were determined with a crashworthiness simulation conducted by the NHTSA using standard values for the metal and not the specific properties of the material. Figure 1.1 shows schematically the process of incorporation of microstructure properties into crashworthiness simulations.

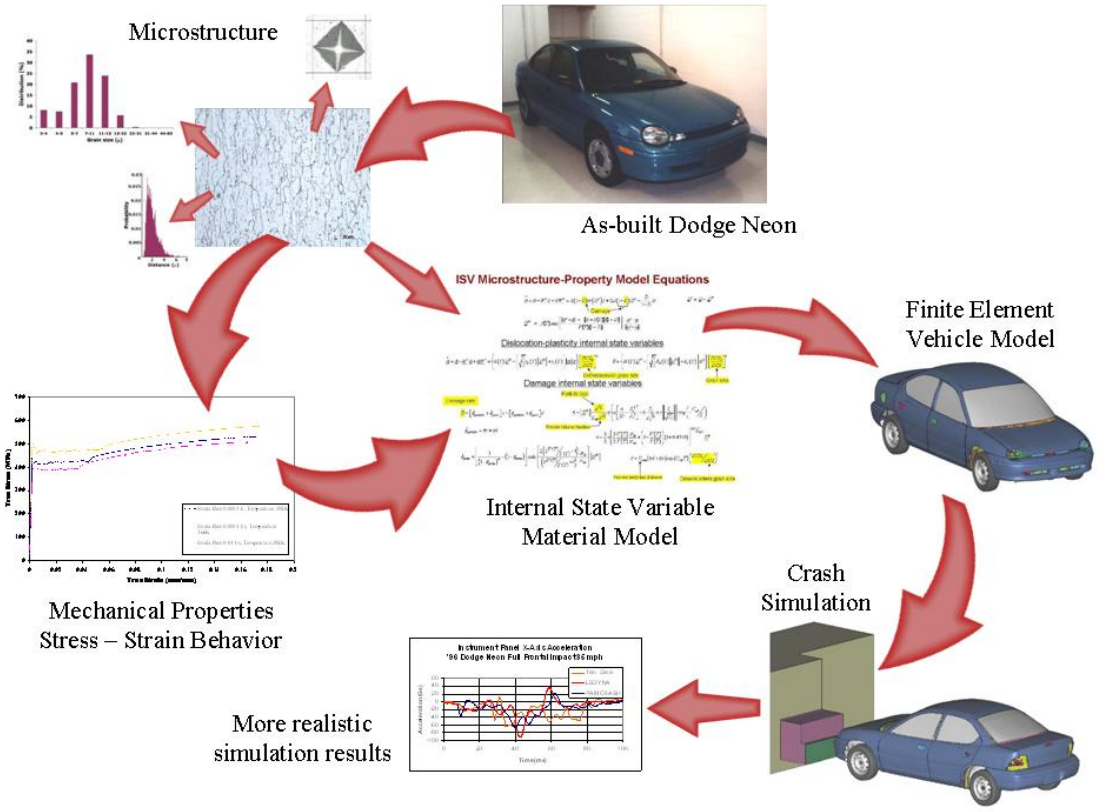

Figure 1.1. Incorporation of microstructure properties into crash simulations.

1.1 Objectives of Study

The objective of this thesis is to perform material characterization on critical Dodge Neon components for material response refinement in crashworthiness simulations. This objective was accomplished during five phases of research. In Phase I of the process critical components of the vehicle were determined based on the most energy-absorbing components during frontal, side, and rear impact crash scenarios. In Phase II, microstructural analyses were conducted on these components to obtain grain size and distribution using the software AxioVision Grains by Zeiss and ASTM E112-96 standard [ASTM Vol. 03.01, 2000]. Microhardness tests were conducted in Phase III to determine the Young's Modulus and Vickers Hardness results for each component.

Phase IV consisted of uniaxial tension tests performed at two different strain rates and at a different temperature (0.01 s^{-1}, 0.0001 s^{-1} at ambient temperature and 200°F) to determine the physical response of the components. The process followed for material characterization of each component is shown schematically in Figure 1.2.

Tension specimens were extracted from the designated parts using ASTM E8 sub size specimen standards [ASTM Vol. 03.01, 2000]. In Phase V these stress-strain curves will be correlated in FE simulations. These refined material response curves will be incorporated into large scale FE codes using a plasticity-damage model.

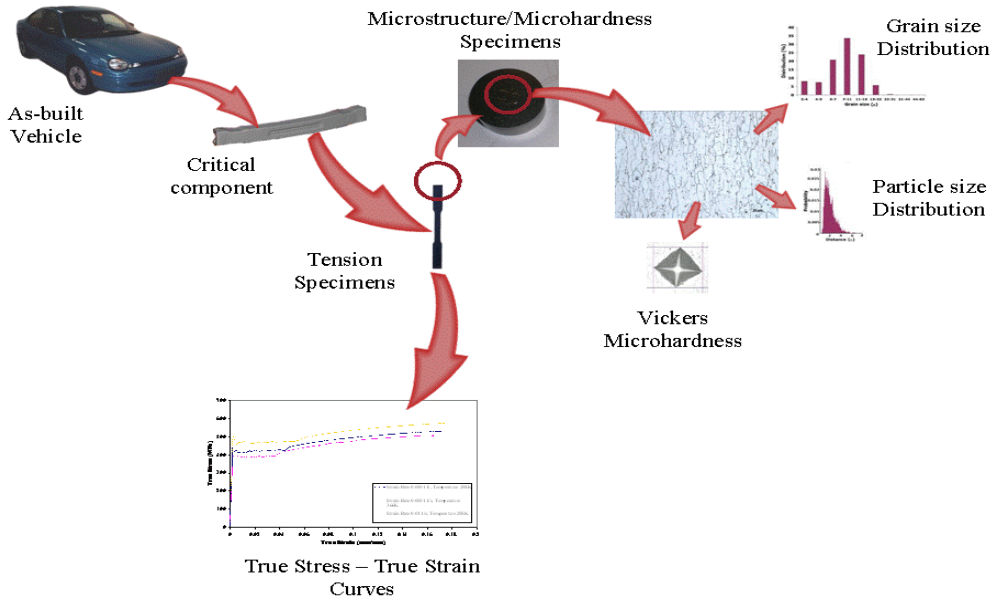

Figure 1.2. Schematic process of structure-property characterization of Dodge Neon critical components.

CHAPTER II

STRUCTURE-PROPERTY EXPERIMENTS

The plasticity parameters used for the Internal State Variable (ISV) model, which will be described in the following chapter, can be correlated utilizing a nonlinear regression analysis of tension or compression test data at constant strain rate [Bamman et al., 1993]. Microstructure properties such as grain size, second phase particles size and volume fraction, among other microstructure properties, have an important influence in void nucleation and growth which cause final failure in ductile materials.

Therefore, in order to correlate the model used in later finite element simulations, several experiments were completed. Mechanical tests such as tension and microhardness, as well as material characterization using mass spectrometry, optical imaging and Scanning Electron Microscopy (SEM) were executed to obtain data to be used in the plasticity model.

In the earlier Dodge Neon simulation, in which the most energy absorbing components were determined, standard values for the metal were used. The specific properties of the materials were not used and microstructure properties were not included. The components studied in this research work, were the front bumper, suspension frame, trunk lid, outer doors, hood, front fenders, front chassis and rear floorboard.

2.1. Material Descriptions

In the last 30 years considerable research has been done regarding alternative materials. However, today's vehicle owners are driving an essentially steel structure which required approximately half a ton of rolled steel to manufacture [Davies, 2003].

Flat rolled steel provides strength and stiffness with good mass to cost ratios, and allow high speed fabrication. In addition, steel exhibits properties that are required for automotive applications such as excellent aging capability, corrosion resistance when coated, paintability, high energy absorption capacity, good fatigue properties, and high work hardening rates. These characteristics, plus the availability of high strength low alloy (HSLA) and alloy steels in a wide variety of sizes, strength levels, chemical compositions, surface finishes, etc., have made sheet steel the material of choice for the automotive industry [Davies, 2003]. Figure 2.1 shows the typical material distribution in a vehicle.

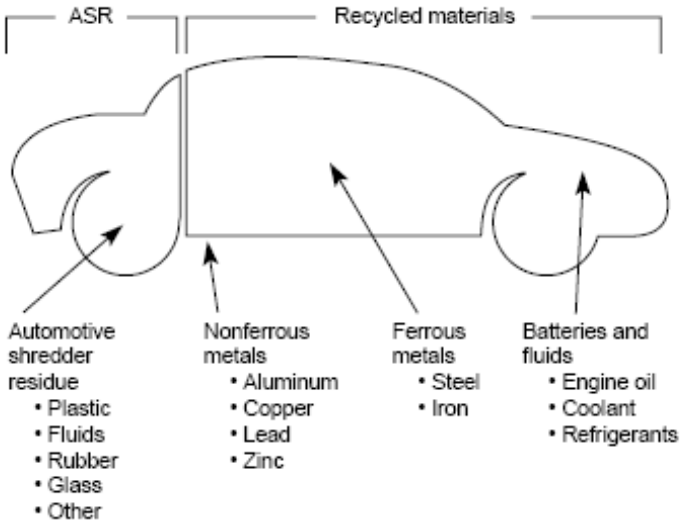

Figure 2.1. Typical materials used in a vehicle [Avallone and Baumeister, 1996].

Steels can be described as alloys which contain iron as the major component [Avner, 1988]. Steels are divided into two main groups; plain carbon steels and alloy steels. The latter can then be subdivided into many groups according to chemistry.

Plain carbon steel is essentially an alloy of iron and carbon which also contains manganese and a variety of residual elements. The American Iron and Steel Institute (AISI) has defined plain carbon steel maximum compositions as follows: Mn below a maximum amount of 1.65 wt. %, less than 0.6 wt. % Si, less than 0.6 wt. % Cu, and does not have any specified minimum content of any other deliberately added alloying element. It is usual for maximum amounts (e.g. 0.05 wt. %) of S and P to be specified.

Alloy steel is produced by the addition of one or more elements to produce specified minimum contents. In general, small additions of rare earth elements such as cerium can be added to plain carbon steel for inclusion control. Table 2.1 shows the influence of some elements on the steels properties.

Low carbon steels generally content less than 0.13% carbon, 0.60% manganese, 0.030% phosphorus, 0.030% sulfur, and greater than 0.02% aluminum. The drawing quality steels have carbon level in the 0.02 to 0.04% range. Some sheet steels used in the automotive industry are available in the following types:

- Commercial Quality
- Low Carbon –Drawing quality
- IF stabilized – Deep drawing quality
- Dent Resistant
- Bake Hardenable
- Non-Bake Hardenable
- High Strength Low Alloy
- High Strength Solution Strengthened
- Ultra High Strength (Dual Phase/ Martensitic)
- Laminated Steels
- Stainless Steels

Table 2.1

Effect of alloying elements in steel [Avallone and Baumeister, 1996].

Element	Strengthening as dissolved in ferrite	Hardenability effect if dissolved in austenite	Effect on grain coarsening in austenite if undissolved as compound	Effect on tempered hardness, strength and toughness
Al	*	*	†	None
Cr	*	†	†	*
Co	†	Negative	None	None
Cu	†	*	None	None
Mn	†	*	*	*
Mo	*	†	†	None
Nb (Cb)	None	†‡	†	†
Ni	*	*	None	None
P	†	*	None	None
Si	*	*	None	None
Ta	‡	†‡	†	†
Ti		†	†	†‡
W	*	†	†	†
V	*	†	†	†

* Moderate to best
† Strong to very strong
‡ Not clear or not used significantly

The interstitial free (IF) steels are stabilized with Ti, Cb, or Cb + Ti, and are normally ultra low carbon (0.005% max). Carbon in solution is used on bake hardenable steels to provide an increase in strength during the paint bake cycle. Therefore, these steels can be produced in a relatively low strength condition and easily formed into parts. However, after forming and paint baking, a significantly stronger part is obtained.

The high strength low alloy steels (HSLA) contain the addition of carbide forming elements Cb, V, or Ti singularly or in combination to a low carbon steel, providing strength through precipitation of fine carbides or carbonitrides of Cb, Ti, and/or V.

In the automotive industry, it is common to find hot-rolled and cold-rolled plain carbon steels, interstitial-free (IF), bake hardening, microalloyed or HSLA and dual-phase.

2.1.1 Steel Classification and Properties

Representatives of automotive companies in cooperation with the Society of Automotive Engineers (SAE) and the American Iron and Steel Institute (AISI) established a classification of steels based on mechanical properties. This classification is shown on Table 2.2 [AISI, 2002].

The specifications containing steels classifications are: SAE J2329 – Categorization and Properties of Low Carbon Automotive Sheet Steels and SAE J2340 – Categorization and Properties of Dent Resistant, High Strength and Ultra High Strength Steels Automotive Sheet Steels.

The old AISI classification was based on deoxidation practice and yield strength whereas the new SAE classification is based on formability.

Table 2.2

SAE Steels Classification

Old AISI Description	New SAE Clasification	Property
Hot Rolled Steels		
CQ Commercial Quality	SAE J2329 Grade 1	N/A
DQ Drawing Quality	SAE J2329 Grade 2	Yield 180 - 290 MPa n value: 0.16 min
DDQ Deep Drawing Quality	SAE J2329 Grade 3	Yield 180 - 240 MPa n value: 0.18 min
Cold Rolled Steels		
CQ Commercial Quality	SAE J2329 Grade 1	N/A
DQ Drawing Quality	SAE J2329 Grade 2	Yield 140 - 260 MPa n value: 0.16 min
DQ Drawing Quality	SAE J2329 Grade 3	Yield 140 - 205 MPa n value: 0.18 min
DDQ Deep Drawing Quality	SAE J2329 Grade 4	Yield 140 - 185 MPa n value: 0.20 min
EDDQ Extra Deep Drawing Quality	SAE J2329 Grade 5	Yield 110 - 170 MPa n value: 0.22 min
SAE J2340		
Old AISI Description	**New SAE Clasification**	
DR Dent Resistant	SAE J2340 Grades 180A, 210A, 250A, 280A Dent Resistant Non Bake Hardenable	
BH Bake Hardenable	SAE J2340 Grades 180B, 210B, 250B, 280B Dent Resistant Bake Hardenable	
High Strength Solution Strengthened	SAE J2340 Grades 300S, 340S High Strength Solution Strengthened	
HSLA High Strength Low Alloy	SAE J2340 Grades 300X, Y; 340X, Y; 380X, Y High Strength Low Alloy 20X, Y; 490 X, Y, 550X, Y	
High Strength Recovery Annealed	SAE J2340 Grades 490R, 550R, 700R, 830R High Strength Recovery Annealed	
DP Dual Phase (HSS)	SAE J2340 Grades DH/DL 500-1000 Mpa Tensile Ultra High Strength Dual Phase	
Martensitic Grade M, HSS	SAE J2340 Grade M 800-1500 MPa Tensile Ultra High Strength Low Carbon Martensite	

2.2. Mechanical Experiments

2.2.1 Material Properties Determined from Tension Tests

Physical material characteristics can be determined from uniaxial tension tests and hardness tests [Avallone and Baumeister, 1996]. Some of the typical characteristics determined from tension tests include the Young's modulus, proportional limit, elastic limit, yield strength, and ultimate strength as described in Figure 2.2. The Young's modulus, or elasticity modulus, is defined by Hooke's law as follows:

$$\frac{\sigma}{\varepsilon} = E \tag{2.1}$$

Another material characteristic is strength. This can be measured as the yield point and the ultimate tensile strength. The fracture point is also important since measures the ductility of the material by giving the elongation to failure, or total strain to failure.

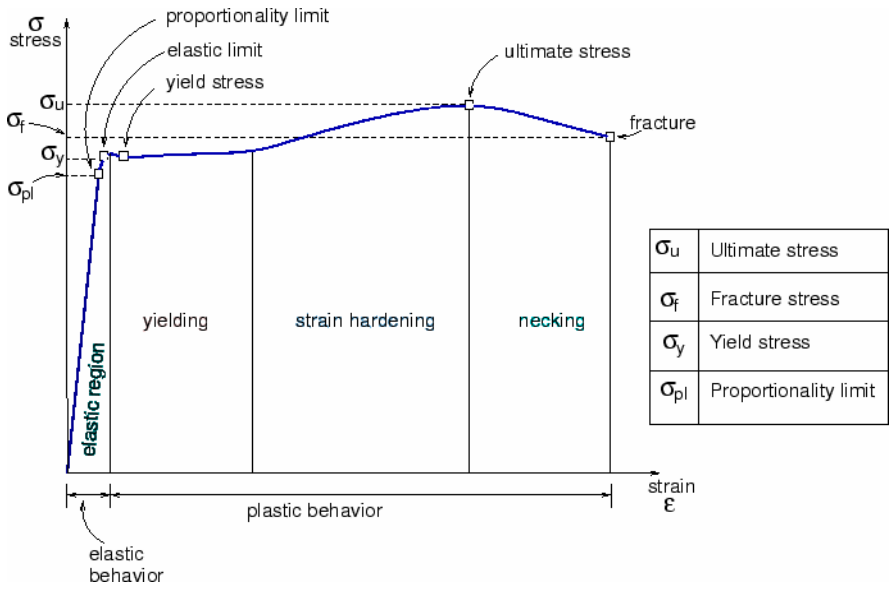

Figure 2.2. Ductile material properties in a stress-strain curve for a low carbon steel [Ugural and Fenster, 1995]

The stress-strain curve and properties derived from it are strongly affected with the change of temperature and strain rate. Generally, the ductility increases and strength decreases as the temperature increases. However, some structure changes occur as strain aging, recrystallization or precipitation take place during the test conditions, modifying or altering this behavior [Dieter, G., 1986].

For tension tests performed during this research work, the uniaxial tensile specimens were extracted from the as-manufactured 1996 Dodge Neon. Specimens were extracted from the designated critical components in areas that were relatively flat and free of spot welds. These specimens were fabricated using a CNC milling machine according to ASTM E8 subspecimen standards [ASTM Standards, 2000].

The flat tension specimen dimensions are shown in Figure 2.3. The thicknesses vary from part to part.

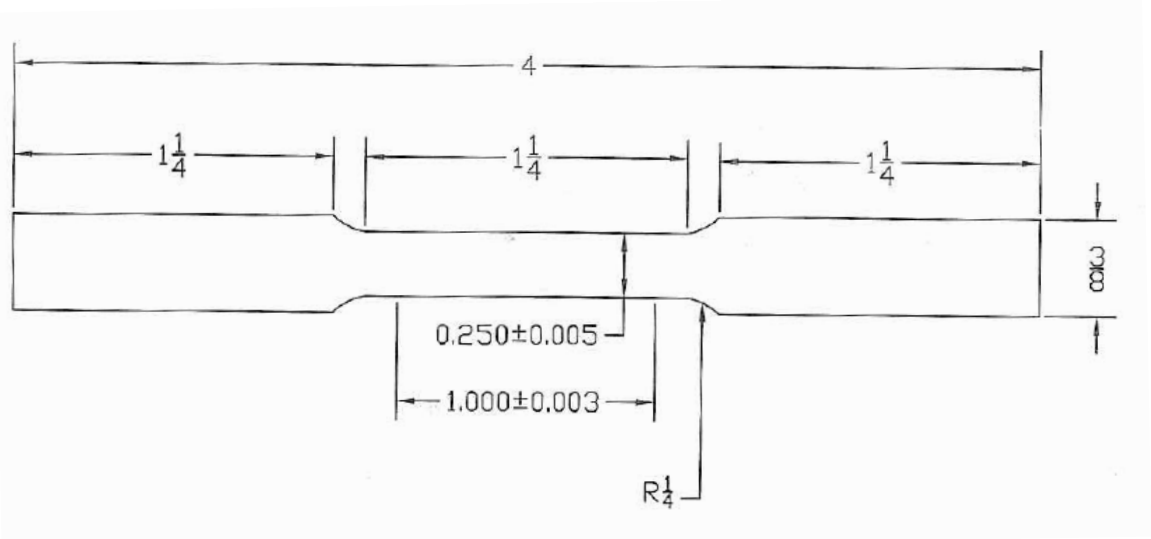

Figure 2.3. Tension specimen dimensions (all dimensions in inches).

Tension tests were performed at three different conditions:

1. Strain rate 10^{-4} s^{-1} and ambient temperature 298 K (77°F)
2. Strain rate 10^{-4} s^{-1} and temperature 366 K (200°F)
3. Strain rate 10^{-2} s^{-1} and ambient temperature 298K (77°F)

The tests at 10^{-4} s^{-1} were performed on an electromechanical machine model *Instron* 5882 and an *Epsilon* extensometer was used. The tests at 10^{-2} s^{-1} were performed on a hydraulic machine model *MTS* 810 using a *MTS* extensometer. All tests were executed under constant strain rate using strain rate control. Figure 2.4 shows photographs of the *Instron* 5882 and *MTS* tension machines.

(a) (b)

Figure 2.4. Photographs of tension machines used: (a) Instron 5882 Electromechanical tension machine (b) MTS 810 Hydraulic tension machine. At the Center for Advanced Vehicular Systems (CAVS).

From the tension tests, mechanical properties as yield strength and elongation to failure play a key role in the Internal State Variable material model. These properties, as

well as other characteristic parameters as hardening or softening of the material were obtained and incorporated into the material model used for crash simulations

2.2.2 Microhardness

Hardness can be defined as a measure of a material's resistance to plastic deformation. It can also be defined as the resistance to local penetration, scratching, machining, wear or abrasion and to yielding [Avallone and Baumeister, 1996].

There are several methods to measure indentation hardness (local penetration) which vary the indenter, load and time used. Some hardness measuring methods are: Brinell, Rockwell and Vickers. These methods can be considered as non-destructive tests [Avallone and Baumeister, 1996]. Figure 2.5 shows a graph with the most used hardness scales.

When the samples are too small, the material availability is limited, or the space to test is reduced; the determination of hardness over small areas is required. For this kind of problems, microhardness is often used. Microhardness is usually measured using the diamond pyramid indenter (Vickers). A distribution of hardness of a surface can be obtained since a better usage of the available space of the sample is used. Vickers hardness is described in ASTM Standard E92-72.

Vickers microhardness was used in this research work. A *LECO* microhardness machine model *LM 300 4T* was used with a load of 500gf.

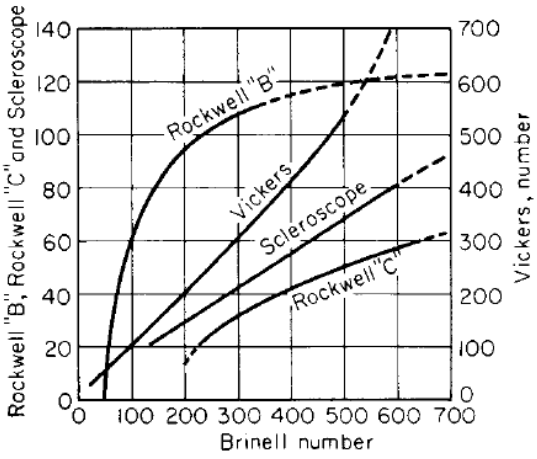

Figure 2.5. Hardness relations

If a material is considered "ideally plastic" (a flat-topped stress – strain curve with a negligible elastic zone) the yield stress can be obtained from the hardness value with the following relation [Tabor, 1951]:

$$\sigma_y = \frac{H}{3} \tag{2.2}$$

For materials that work-harden and conform to $\sigma = K\varepsilon^n$, the yield strength and tensile strength can be obtained using the equations [Cahoon, 1971]:

$$\sigma_y = \frac{H}{3}(0.1)^n \tag{2.3}$$

$$\sigma_{UTS} = \frac{H}{3}(1-n)\left[\frac{12 \cdot 5n}{1-n}\right]^n \tag{2.4}$$

Where n is the hardening coefficient of the material that can be obtained from the stress-strain curves, σ_y is the yield strength and σ_{UTS} is the ultimate strength of the material. The hardness and stress must be expressed in the same units. Vickers hardness is usually expressed in kgf/mm^2, to convert Vickers hardness to MPa, the HV number is multiplied by 9.807 (general conversion of units).

Nine indentations were performed in every sample, as shown in Figure 2.6, in order to get a Vickers hardness distribution through the surface and a mean value of the material. The indentation dimensions and Vickers hardness value were obtained using the software Confident, developed by *LECO*.

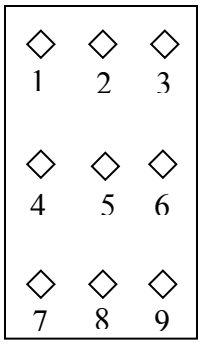

Figure 2.6. Indentation location in every hardness sample

2.3 Microstructure Analyses

2.3.1 Optical Metallography

Optical metallography consists on examination of materials using visible light to obtain a magnified image of the microstructure. This method is used to characterize

structure since the grain boundaries, phases, inclusions and mechanical deformations are revealed [ASM Handbook v.10, 2005].

The behavior of a material is often determined by the micro and macrostructure. The characterization of effects of composition and other variables in the microstructure is often required. Microstructures of metals and alloys are determined by composition, solidification processes and thermomechanical treatment. There are some typical structure-property relationships that have been established using optical metallography, and the study of mechanical properties, such as:

- General increase in yield strength and hardness of metals by decreasing grain size
- Tendency for a decreased ductility with increasing inclusion content
- Association of failure initiation with microstructural inhomogeneities such as second-phase particles
- Anisotropic mechanical behavior associated with elongated grains or grain orientations

A standard procedure to prepare the specimens was used. Metallurgical samples were cut from the undeformed grip area of the uniaxial tension specimens. This ensures that the microstructure data corresponds directly with the mechanical data of each component.

The metallurgical specimens were hot-mounted with epoxy in two different orientations, a top view and side view. The figure 2.7 shows schematically the process followed to obtain the specimens from every car component.

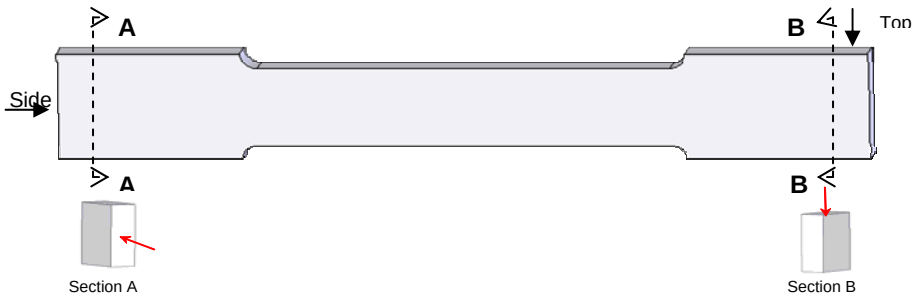

Figure 2.7. Extraction of hardness and microstructure specimens from tensile specimens.

These specimens were polished using standard automatic polishing procedures for steel. After polishing, the samples were etched with a 2% nital solution (nitric acid and alcohol) to expose the grain structure of the specimen for microstructural analysis. Figure 2.8 shows schematically the general process of extraction of these specimens.

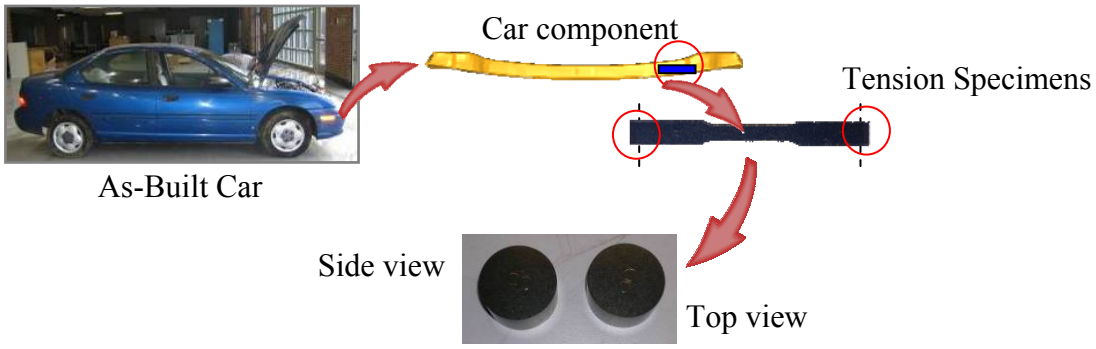

Figure 2.8. Schematic process of specimen extraction from the as-built vehicle.

A *Zeiss* optical microscope model *AxioVert 200M*. Grain size distribution was obtained from these specimens using the *AxioVision Grains* developed by *Zeiss*. Figure 2.9 shows a screenshot of this software. To measure the grain size and distribution, the

ASTM 112-96 can be used following the pattern shown in Figure 2.9, which is used by the AxioVision Grains software.

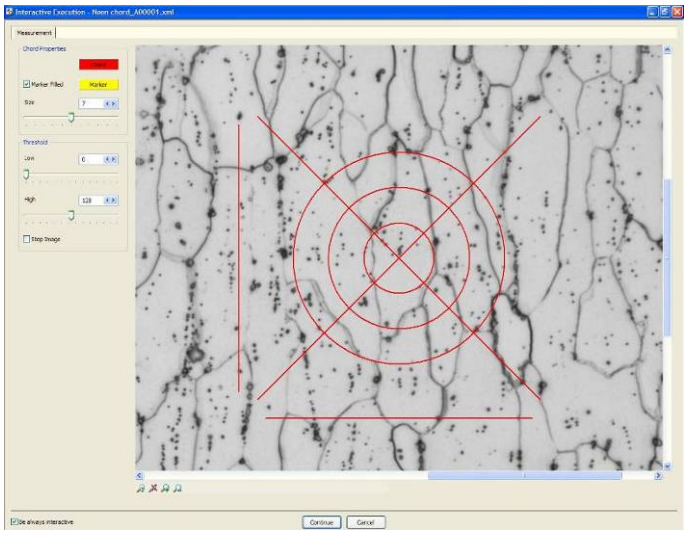

Figure 2.9. AxioVision Grain window illustrating the software used for grain size measurement.

Particle size and distribution was obtained using the *ImageAnalyzer* software developed at *CAVS*. Figure 2.10 shows screenshot of this software and results obtained from it.

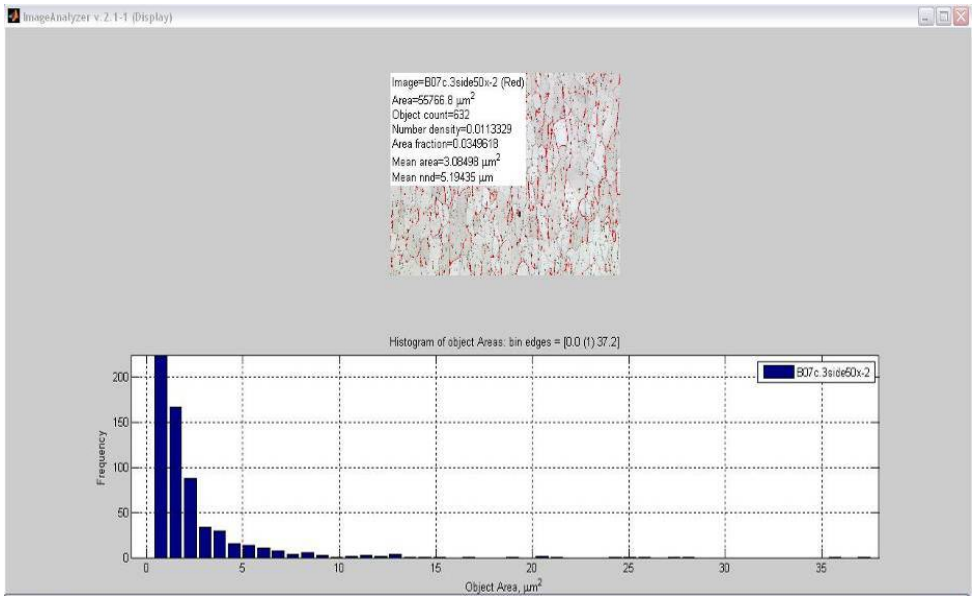

Figure 2.10. ImageAnalyzer window illustrating the software used for particle size distribution.

2.3.2 Mass Spectroscopy

With mass spectroscopy, a quantitative of different elements in a sample can be determined. Thus, the concentration of alloying elements in steels and other alloys can be rapidly obtained using this method [ASM Handbook v.10, 2005].

This method was used to obtain vehicle component material compositions in this research work. A spark analyzer from *Spectro* model *SpectroMaxx* was used.

2.3.3 Scanning Electron Microscopy

In Scanning Electron Microscopy (SEM), the surface of a specimen is bombarded with a beam of electrons to provide information for producing an image. With SEM the surface to be analyzed can be magnified at 10 to 100000X with good resolution of the image up to 3 to 100nm depending on the sample and equipment. The SEM provides two

major advantages over the optical microscope: resolution and depth of field [ASM Handbook v.10, 2002].

SEM was used in this research to obtain images of fractured surfaces of tensile specimens.

2.4. Vehicle Component Experimental Results

2.4.1 Front Bumper

The Dodge Neon front bumper was the most critical component in the frontal impact crash scenarios. The alloy element concentration was obtained using mass spectrometry and the results are presented in Table 2.3.

Table 2.3

Front bumper material element concentration

Element	Concetration %
Fe	98.3
C	0.078
Mn	1.2
Nb	0.103
V	0.063
Al	0.048
Si	0.044
Cr	0.044
W	0.017
Se	0.015
Cu	0.015
Ni	0.012
Zn	0.01
Others	0.061

The material samples of the bumper were extracted from different locations in the component in order to obtain grain size distribution along the vehicle part. The objective of this analysis is to map or distribute this characteristic in the finite element mesh in future studies. Figure 2.11 shows the location of the samples in the front bumper.

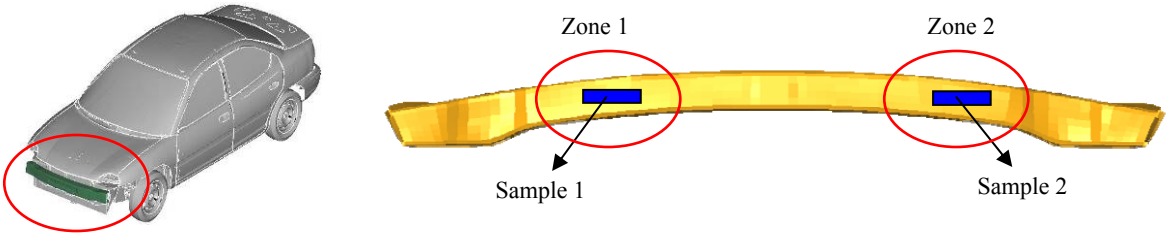

Figure 2.11. Sample location in the front bumper.

The microstructure that corresponds to these locations is shown in Figure 2.12. Grain size distribution of these samples was executed and the values are shown in Figure 2.13.

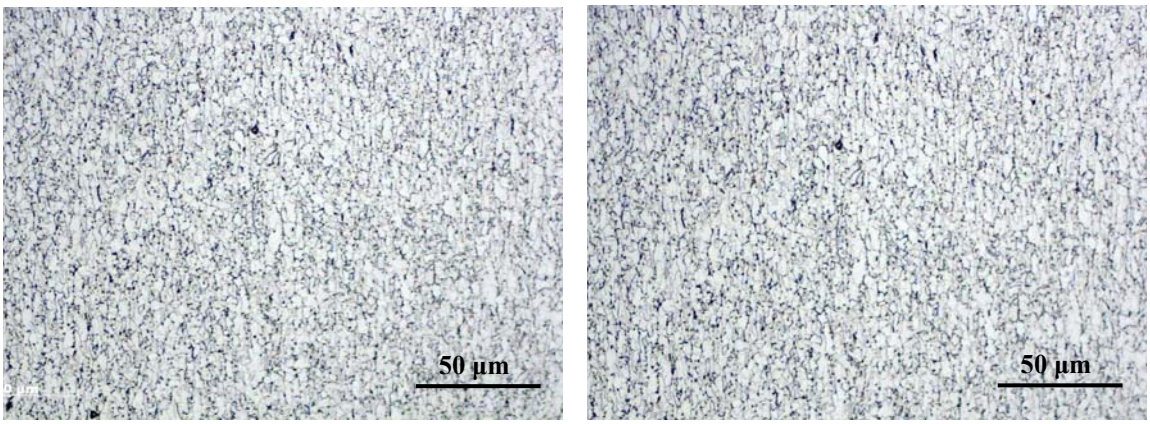

(a) (b)

Figure 2.12. Front bumper material optical micrographs at two different locations (Refer to Fig. 2.10). (a) Sample 1; (b) Sample 2.

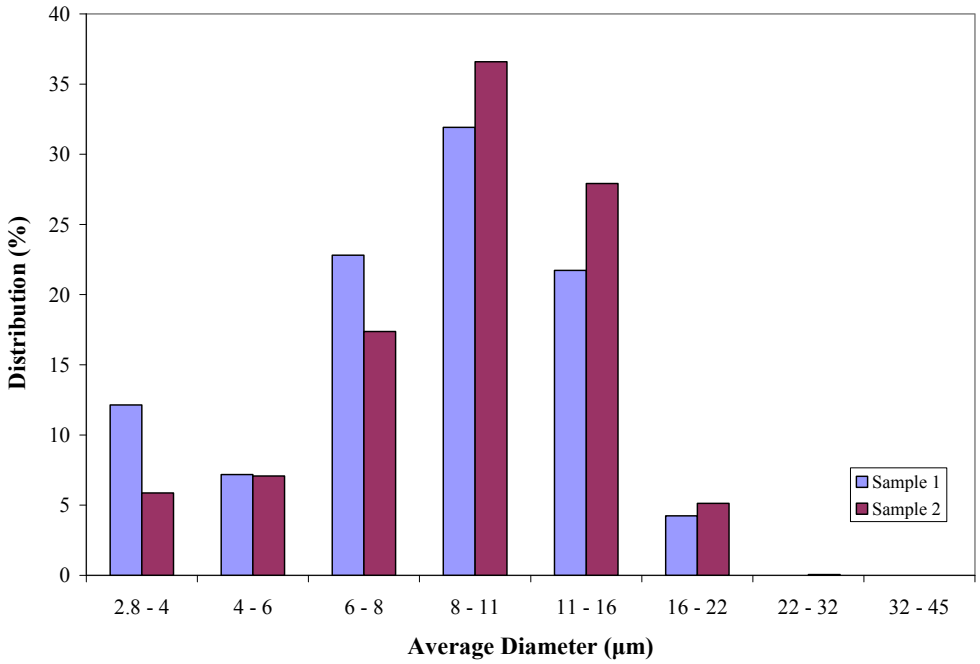

Figure 2.13. Grain size distribution of front bumper Samples 1 and 2.

A very fine grain can be observed in Figure 2.12. The grain sizes varied from 2.8 µm to 22 µm but the greatest distribution of grains corresponded to average diameters of 8 µm to 11 µm.

The microstructure of this material is basically comprised by a ferrite matrix in which particles are precipitated. From the composition of Table 2.3, Nb, V, and Ti are present. With the use of these elements, grain refinement and precipitation strengthening is achieved. They are also strong carbide and nitride formers. Therefore, it is presumed that the precipitates are Nb, V, Ti (C, N). Particle size was obtained from optical micrographs using ImageAnalyzer. The particle sizes obtained varied from 0.2 µm to 4 µm. The Vickers hardness of these samples is shown in Figure 2.14.

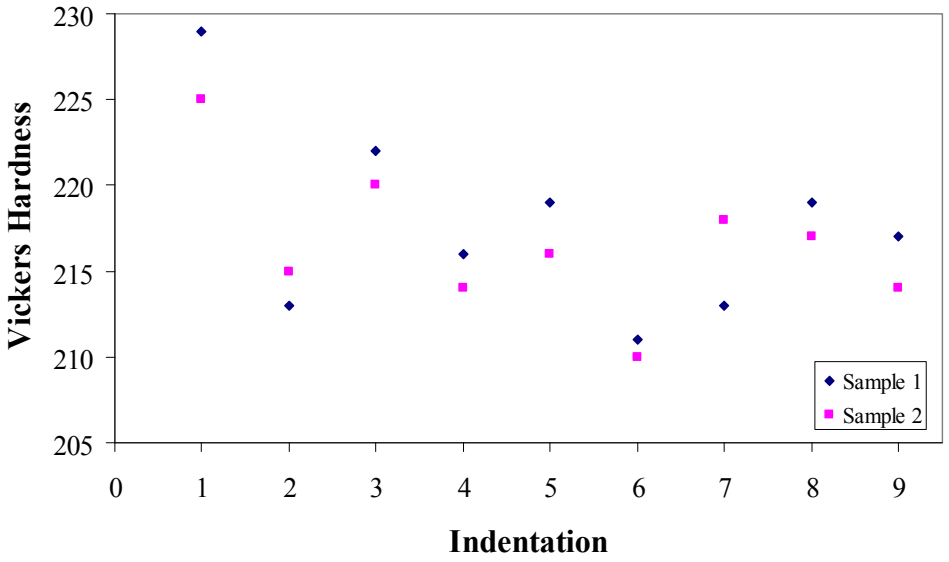

Figure 2.14. Vickers hardness distribution on front bumper Samples 1 and 2.

The Vickers hardness values vary from 210 HV to 229 HV, giving a mean value of 217±5 HV. The hardness distribution was homogeneous with some variations as observed in Figure 2.14. Is important to mention that steels used for automotive applications are usually zinc-coated which might have a slight effect on the properties around the surface close to the coat. Refer to Figure 2.5 for indentation locations.

Using the mean value of the Vickers hardness of these samples, the yield stress was obtained using Equation 2.3. A value of 554MPa was obtained. This value differs about 30 MPa from the 10^{-4} s^{-1} strain rate experimental data (comparing to results presented on Table 2.4

Tension results obtained Sample 1 and 2 (Fig. 2.11) of this material for all the conditions are shown in Figure 2.15.

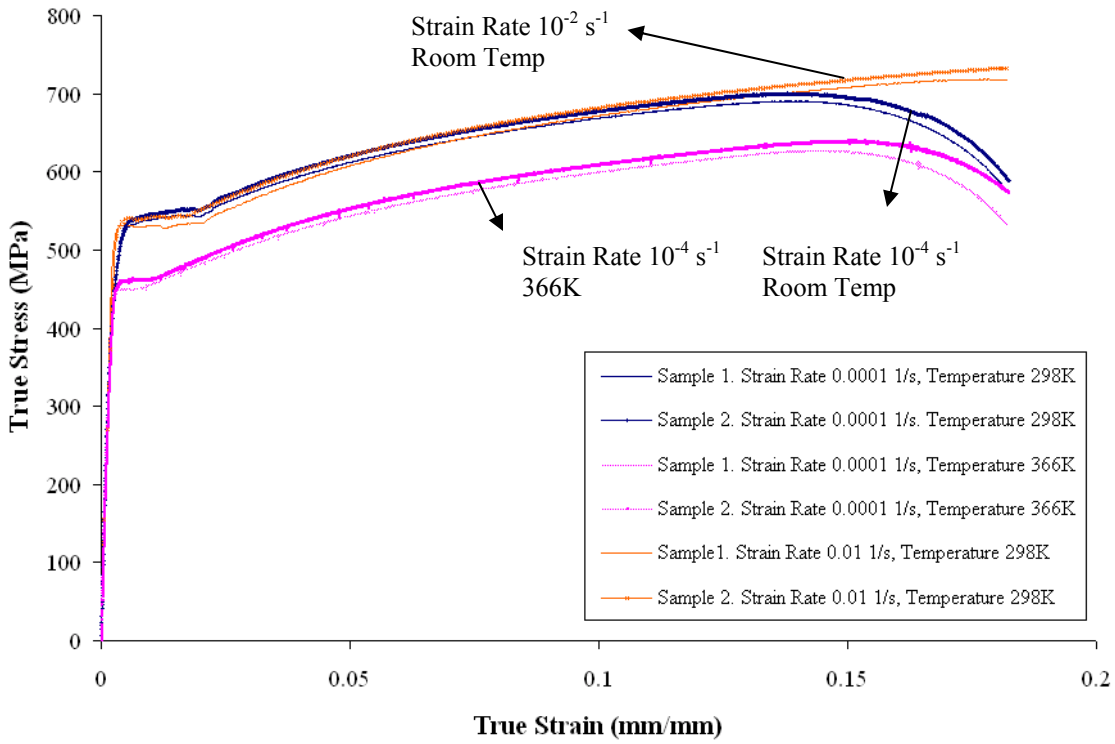

Figure 2.15. True Stress – True Strain behavior of front bumper. Samples located in different zones (Refer to Fig. 2.11).

The yield point value is slightly higher for the higher strain rate (10^{-2} s^{-1}) and is lower for a higher temperature. However, the differences between the lower and higher rates stress-strain behavior (at the same temperature) is not evident. The results correspond to the predicted in the literature for higher temperatures [Avner, 1988]. The results obtained for the front bumper material are off the range for plain carbon steels [Avalone and Baumeister, 1996].

Minor differences in the stress – strain behavior of the samples can be observed. These differences can be attributed to slight changes in the microstructure-properties depending on the location, although these changes are small. The mechanical properties of this material along with the micrsotructure properties are summarized in Table 2.4.

SEM images were taken to analyze the fracture surface of these samples. Figure 2.16 shows an image of the front bumper material and Figure 2.17 shows the image analysis results (object area). The porosity at failure was obtained using ImageAnalyzer. The pores area fraction was 0.19 – 0.21, the pore sizes varied from 0.7μm to 2μm.

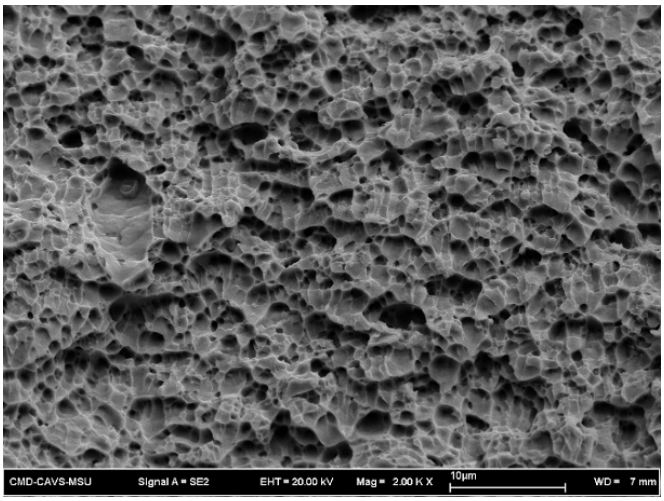

Figure 2.16. SEM image of front bumper uniaxial tension specimen fracture surface at ambient temperature, strain rate of 10^{-4} s^{-1} for Sample 1.

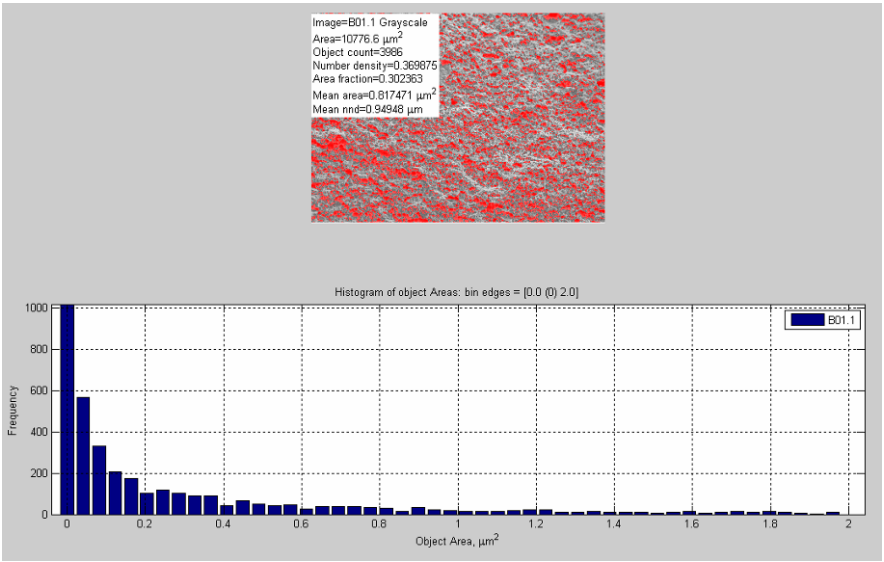

Figure 2.17. Image analysis results of front bumper material with pore area distribution plot of Sample 1, strain rate of 10^{-4} s^{-1} at ambient temperature.

The alloy composition, microstructure and mechanical properties of this material describe a microalloyed High Strength Low Alloy steel [AISI, 2002].

Bringing together the stress – strain behavior and the microstructure-properties of each sample, the material properties of the front bumper can be summarized as shown in Table 2.4.

Some difference in the properties can be observed depending on location, as it was mentioned before in this section. However, these differences are not considerable. Therefore, the property distribution along the vehicle component can be assumed as homogenous.

Table 2.4

Mechanical and structure properties of front bumper material

	Mechanical Properties	***Zone 1***	***Zone 2***
10-4 s-1 Amb. Temp.	Young's Modulus (GPa)	198.3	201.5
	Yield Point (MPa)	527.9	535.4
	Ultimate Strength (MPa)	690.6	698.5
	Strain to failure (%)	19	21
	Energy Absorption (J/m^3*10^6)	131.1	146.6
10-4 s-1 366K	Young's Modulus (GPa)	217.4	209.3
	Yield Point (MPa)	439.5	432.2
	Ultimate Strength (MPa)	546.25	593.2
	Strain to failure (%)	19	20
	Energy Absorption (J/m^3*10^6)	103.7	118.6
10-2 s-1 Amb. Temp.	Young's Modulus (GPa)	214.6	194.1
	Yield Point (MPa)	517.6	501.6
	Ultimate Strength (MPa)	611.2	602.2
	Strain to failure (%)	22	23
	Energy Absorption (J/m^3*10^6)	134.4	138.5
	Vickers Hardness	216.5	217.6
Microstructure Properties			
	Grain Size (main) (μm)	8.34	7.8
	Grain aspect ratio	0.34	0.33
	Particle size (μm)	0.66	0.62
	Particle density	0.136	0.138
	Distance Particle - Particle (μm)	1.53	1.55
	Particle area fraction	0.066	0.069
	Void size (μm)	1.1	0.81
	Void density	0.424	0.486
	Final void area fraction	0.19	0.199

2.4.2 Suspension Frame

The suspension frame was another critical component in the crash scenarios. The alloy element concentration was obtained using mass spectrometry and the results are presented in Table 2.5.

Table 2.5

Suspension frame material element concentration

Element	Concetration %
Fe	98.6
C	0.078
Mn	0.476
Al	0.074
Si	0.05
Nb	0.044
Cr	0.036
Zn	0.036
Cu	0.019
P	0.012
Ta	0.01
Ni	0.0082
W	0.0072
Others	0.066

The material samples of the suspension were extracted from different locations in the component in order to obtain grain size distribution along the vehicle part. Figure 2.18 shows the location of the samples in the suspension frame.

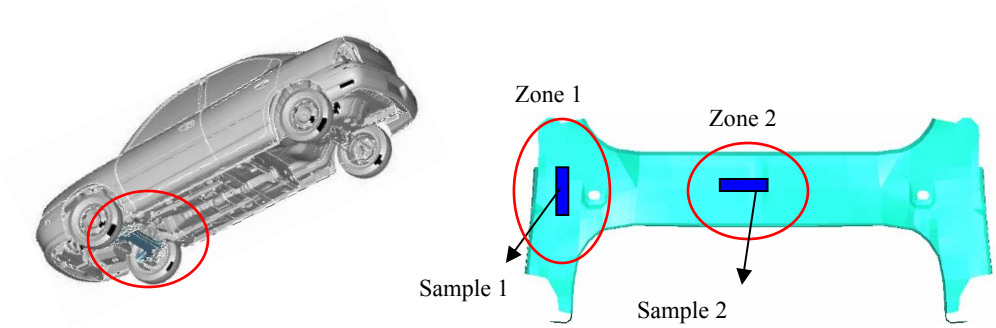

Figure 2.18. Suspension frame specimen location.

The microstructure that corresponds to these locations is shown in Figure 2.19. Grain size distribution of these samples was obtained and the values are shown in Figure 2.20.

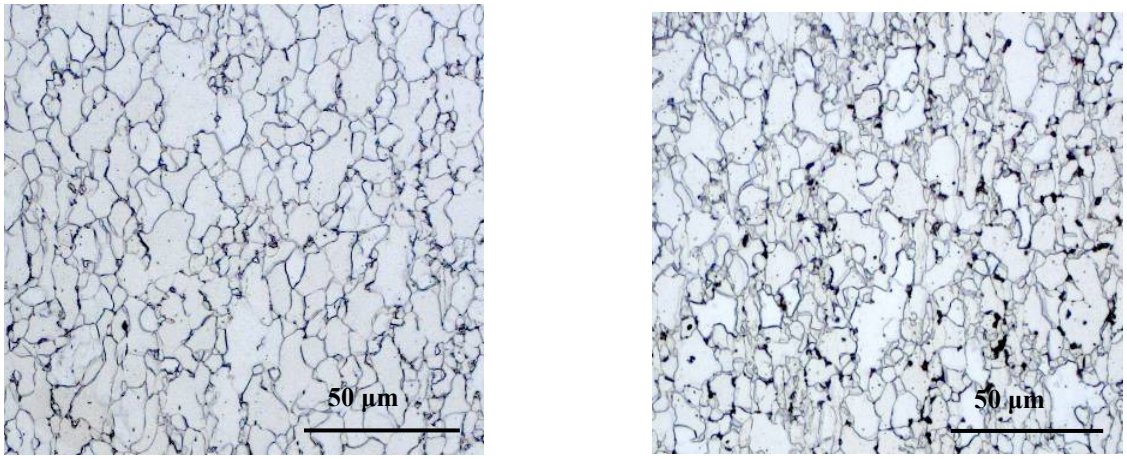

(a) (b)

Figure 2.19. Suspension frame material optical micrographs at two different locations (Refer to Fig. 2.17). (a) Sample 1, (b) Sample 2.

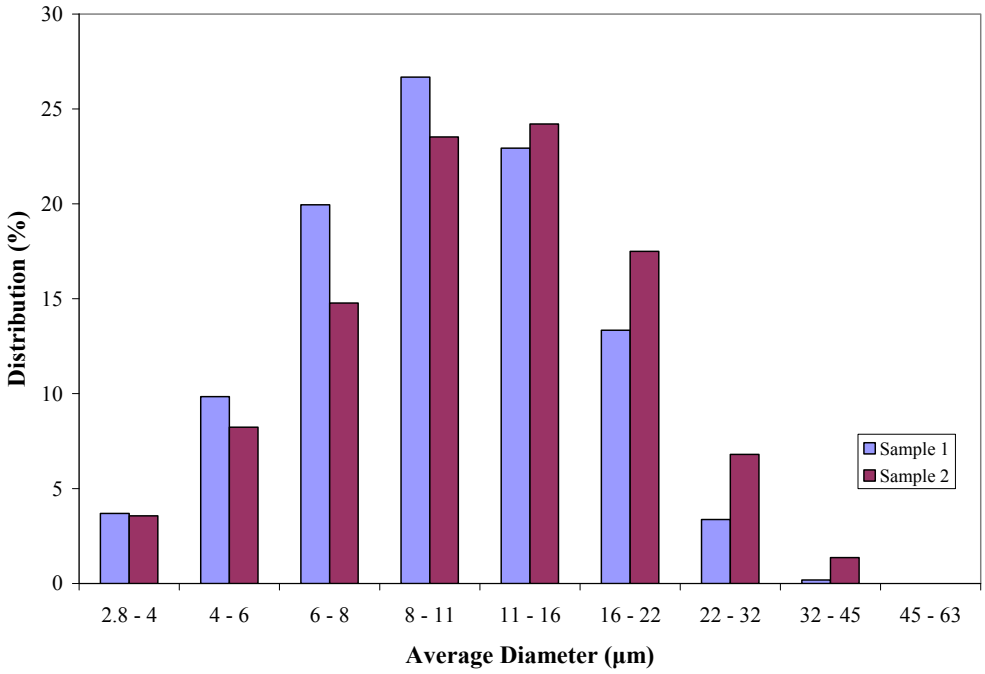

Figure 2.20. Grain size distribution of suspension frame Samples 1 and 2.

The microstructure of the suspension is composed of a ferrite matrix and a second phase particles or precipitates can be observed in the microstructure. A fine ferrite grain can be observed in Figure 2.19 and 2.20. The grain sizes varied from 2.8 µm to 32 µm but the greatest distribution of grains corresponded to average diameters of 8 µm to 16 µm. Particle size was obtained from optical micrographs using ImageAnalyzer. The particle sizes obtained varied from 0.7 µm to 3.1 µm.

This material contains Nb which is carbide former. Thus, it is presumed that the precipitates present in the material are NbC. The Vickers hardness of these samples is shown in Figure 2.21.

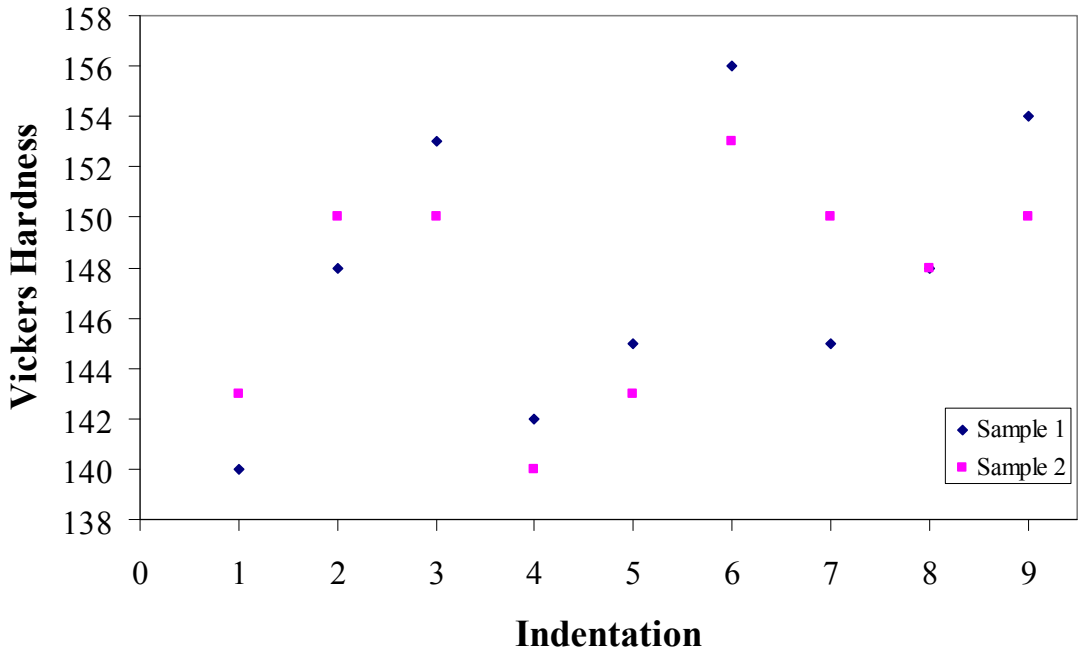

Figure 2.21. Vickers hardness distribution on suspension frame Samples 1 and 2.

The Vickers hardness values varied from 140 HV to 155 HV, giving a mean value of 148±5 HV. The hardness distribution was homogeneous with some variations as observed in Figure 2.21. Refer to Figure 2.6 for indentation locations.

Using the mean value of the Vickers hardness of these samples, the yield stress was obtained using Equation 2.3 to compare results with the experimental data. A value of 360MPa was obtained.

Tension results obtained for the zones (Fig. 2.18) for all the conditions are shown in Figure 2.22.

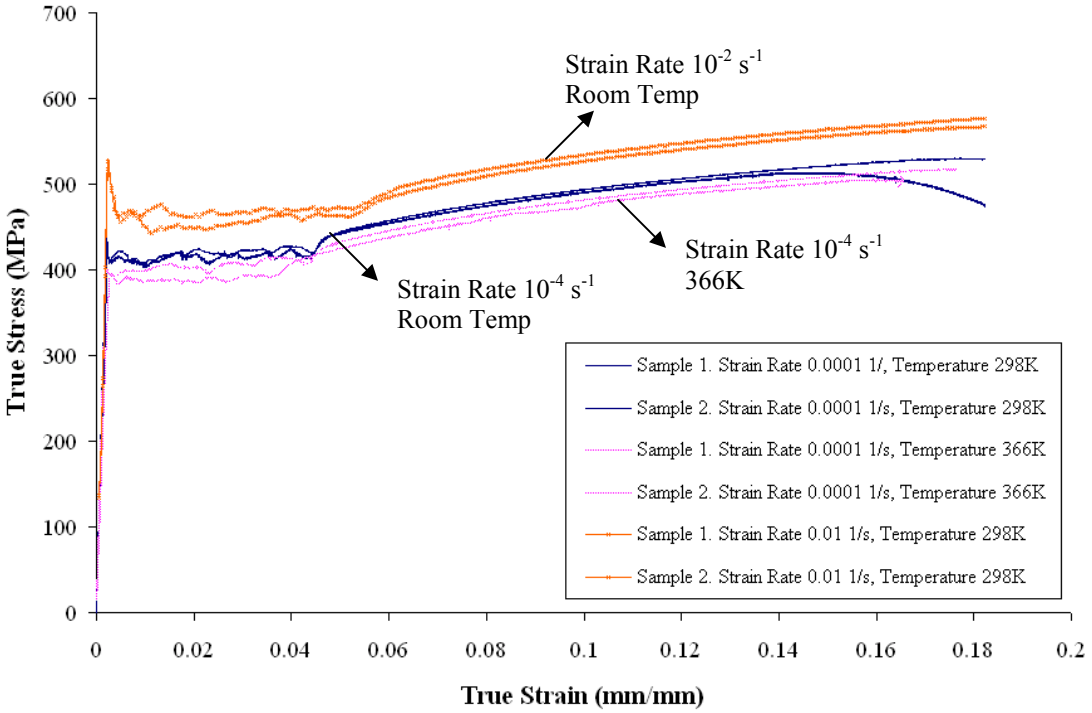

Figure 2.22. True Stress – True Strain behavior of suspension frame. Samples located in different zones (Refer to Fig. 2.18).

The yield point value is higher for the higher strain rate (10^{-2} s^{-1}) and is lower for a higher temperature. These results correspond to the yield dependence on strain rate and temperature predicted in literature for steels. The strain to failure for strain rate 10^{-4} and 10^{-2} s^{-1} at ambient temperature was 22% and for the high temperature test was 24%

Strain rate dependence on yield point can be clearly observed in Figure 2.18. The yield stress obtained for a 10^{-2} s^{-1} strain rate is higher than with 10^{-4} s^{-1} strain rate. Temperature dependence can also be observed but is not as marked as the strain rate dependence. The yield point and ultimate strength are higher than plain carbon steel values for all the conditions in which the material was tested. Some differences can be observed in the stress –strain behavior between the two samples. These differences can be

attributed to slight differences in grain and particle size of each sample corresponding to its location in the component.

SEM images were taken to analyze the fractured surface of these samples. Figure 2.23 shows an image of the suspension material and Figure 2.24 shows the image analysis results (object area). The porosity at failure was obtained using ImageAnalyzer. The pores area fraction was 0.26-0.28, the highest distribution of pore sizes corresponded to sizes 1μm to 4μm.

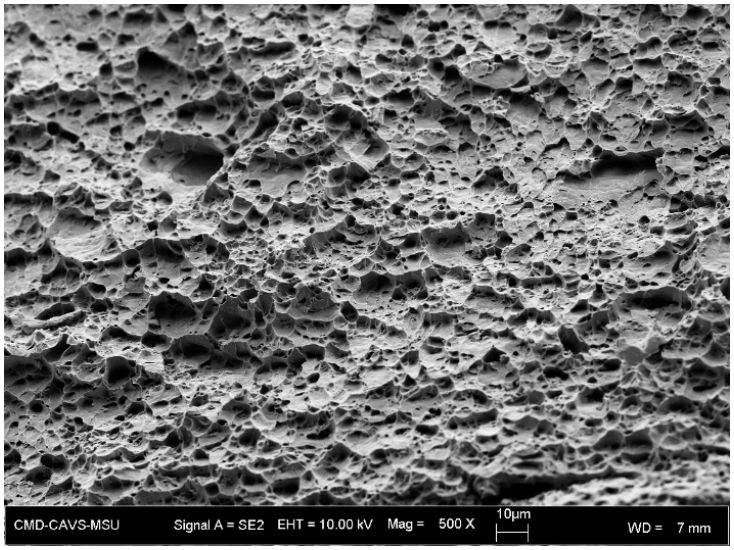

Figure 2.23. SEM image of suspension frame uniaxial tension specimen fracture surface at ambient temperature, strain rate of 10^{-4} s^{-1} for Sample 1.

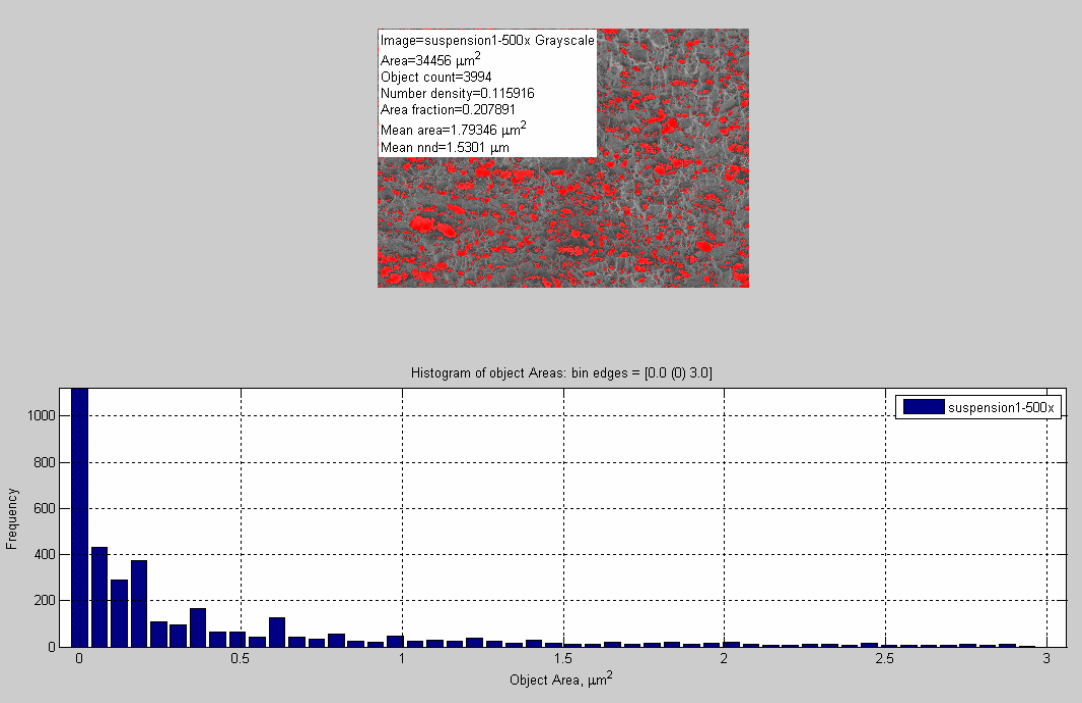

Figure 2.24. Image analysis results of suspension frame material with pore area distribution plot of Sample 1, strain rate of 10^{-4} s^{-1} at ambient temperature.

The alloy composition, microstructure and mechanical properties of this material describe a microalloyed High Strength Low Alloy steel [AISI, 2002].

Bringing together the stress – strain behavior and the microstructure-properties of each sample, the material properties of the suspension frame can be summarized as shown in Table 2.6.

Table 2.6

Mechanical and structure properties of suspension frame material

	Mechanical Properties	***Zone 1***	***Zone 2***
10-4 s-1 Amb. Temp.	Young's Modulus (GPa)	221.2	183.5
	Yield Point (MPa)	400.9	431.6
	Ultimate Strength (MPa)	529.9	530.5
	Strain to failure (%)	19	21
	Energy Absorption ($J/m^3 *10^6$)	100.6	111.4
10-4 s-1 366K	Young's Modulus (GPa)	216.6	142.8
	Yield Point (MPa)	416.2	391.6
	Ultimate Strength (MPa)	512.5	505.3
	Strain to failure (%)	19	20
	Energy Absorption ($J/m^3 *10^6$)	97.3	106.1
10-2 s-1 Amb. Temp.	Young's Modulus (GPa)	214.6	194.1
	Yield Point (MPa)	517.5	526.7
	Ultimate Strength (MPa)	567.2	577.7
	Strain to failure (%)	23	24
	Energy Absorption ($J/m^3 *10^6$)	107.7	121.3
	Vickers Hardness	131.4	133.7
	Microstructure Properties		
	Grain Size (main) (μm)	10.3	9.8
	Grain aspect ratio (with/length)	0.64	0.5
	Particle size (μm)	0.66	0.68
	Particle density	0.049	0.06
	Distance Particle - Particle (μm)	6.2	5.1
	Particle area fraction	0.044	0.049
	Void size (μm)	1.03	0.832
	Void density	0.09	0.14
	Final void area fraction	0.26	0.28

As it was mentioned before, some differences in the properties are observed depending on the sample location. The differences are not large; therefore it can be assumed that the property distribution along the vehicle component is homogeneous

2.4.3 Trunk Lid

The Dodge Neon trunk lid was also a critical component. The alloy chemical composition was obtained using mass spectrometry and the results are presented on Table 2.7.

Table 2.7

Trunk lid material element concentration

Element	Concetration %
Fe	99.2
C	0.065
Mn	0.287
Al	0.076
Cr	0.07
Si	0.064
Zn	0.036
Sb	0.023
Nb	0.004
V	0.0023
Cu	0.013
Ni	0.012
Ca	0.012
Ta	0.01
Others	0.065

Similar to the components presented before, the material samples of the trunk lid were extracted from different locations in the component in order to obtain grain size distribution along the vehicle part. Figure 2.25 shows the location of the samples in the trunk lid.

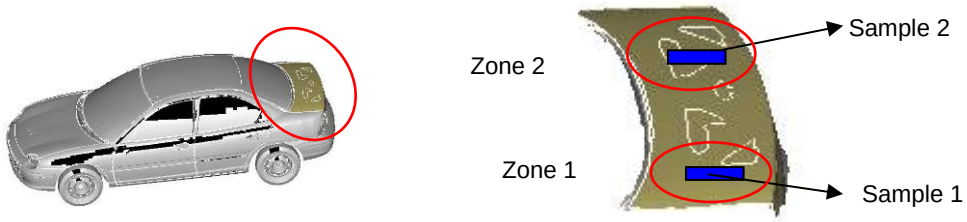

Figure 2.25. Sample location in the trunk lid.

The microstructure that corresponds to these locations is shown in Figure 2.26. Grain size distribution of these samples was determined and the values are shown in Figure 2.27.

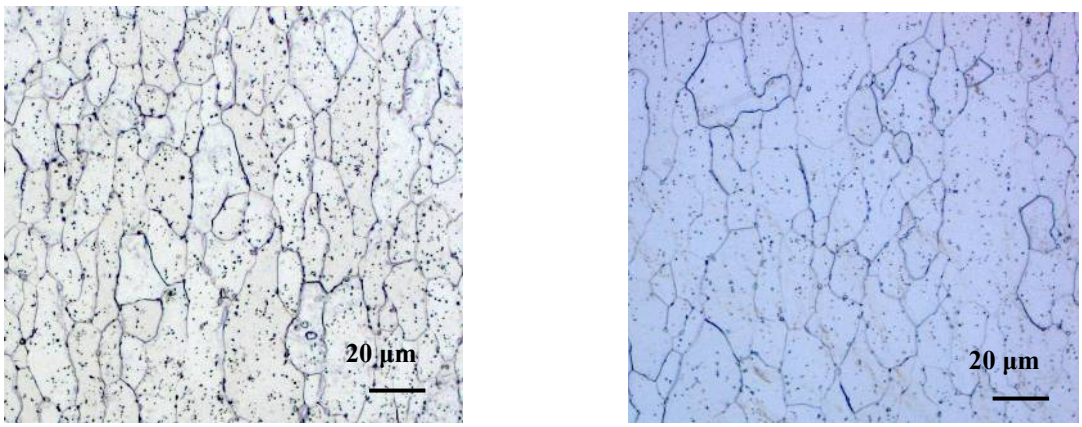

(a) (b)

Figure 2.26. Trunk lid material optical micrographs at two different locations (Refer to Fig. 2.25). (a) Sample 1; (b) Sample 2.

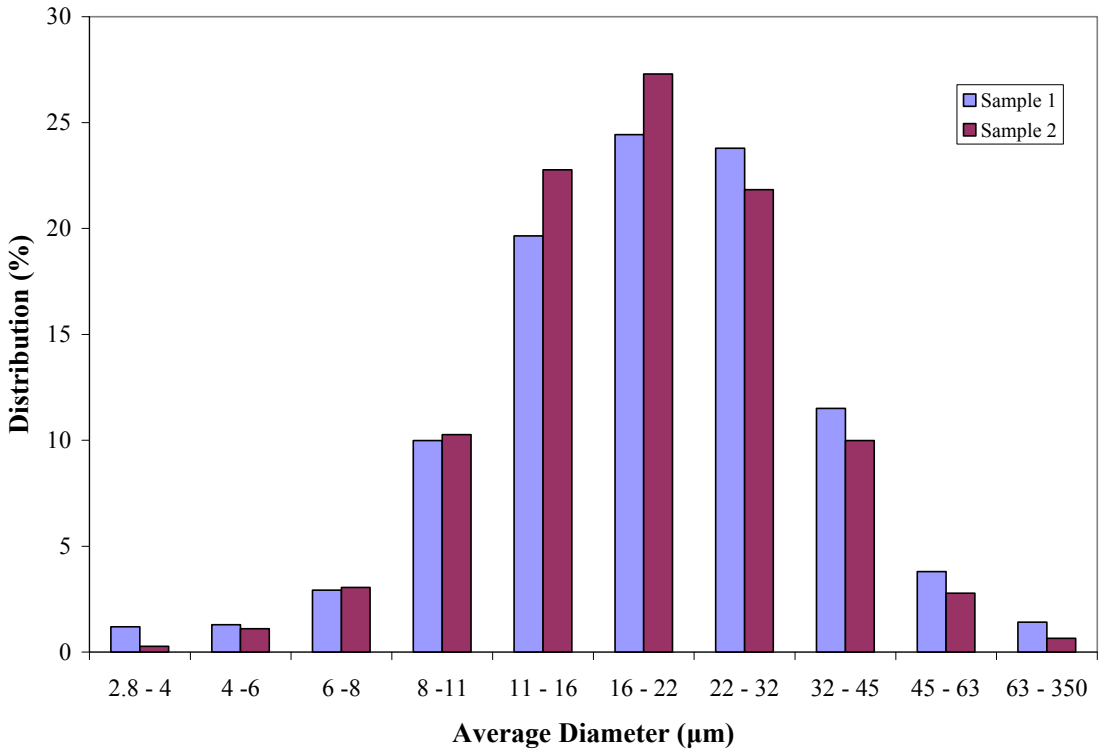

Figure 2.27. Grain size distribution of trunk lid Samples 1 and 2.

This material is also composed by a ferrite matrix with precipitated particles. The ferrite grain sizes varied from 2.8 µm to 63 µm but the greatest distribution of grains corresponded to average diameters of 22 µm to 63 µm. Some elongation of ferrite grains is observed. Since this material is sheet metal, the elongation direction corresponds to the rolling direction of the material.

Very fine precipitates can be observed distributed unevenly inside the grains. This material contains Nb and V, elements that, as has been mentioned before, are carbide and nitride formers and grain refiners. Therefore, it is presumed that the particles are NbC. Particle size was obtained from optical micrographs using ImageAnalyzer. The particle

sizes obtained varied from 1 µm to 4 µm. The Vickers hardness of these samples is shown in Figure 2.28.

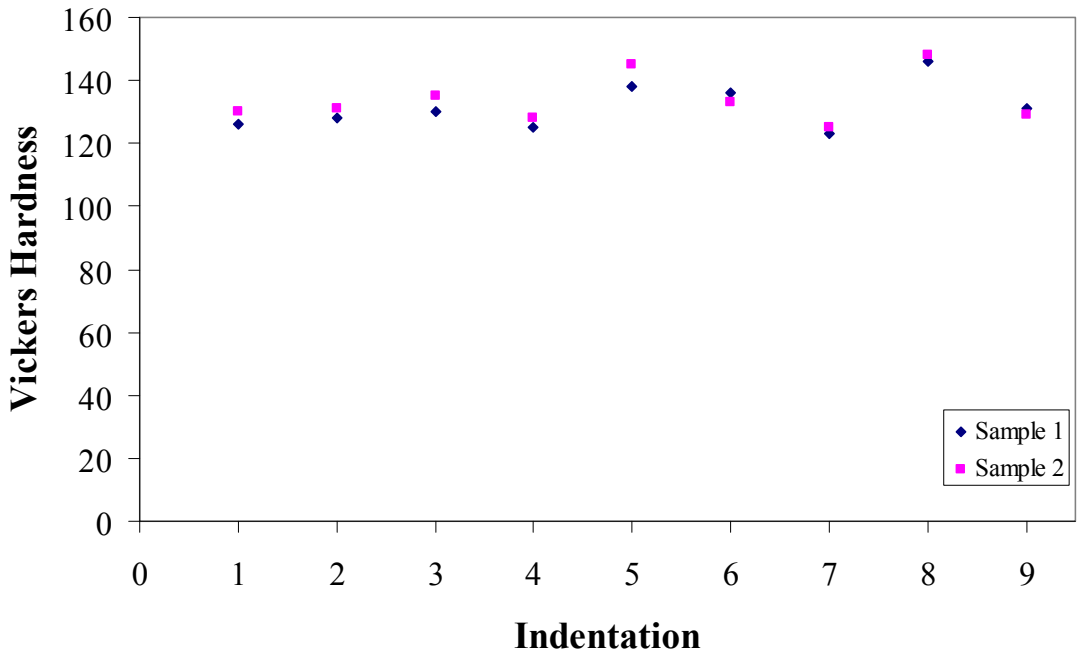

Figure 2.28. Vickers hardness distribution on trunk lid Samples 1 and 2.

The Vickers hardness values varied between 120 HV to 150 HV, giving a mean value of 132±7 HV. The hardness distribution was homogeneous as observed in Figure 2.28. Refer to Figure 2.6 for indentation locations.

Using the mean value of the Vickers hardness of these samples, the yield stress was obtained using Equation 2.3. A value of 383MPa was obtained.

Tension results obtained for both zones. (Fig. 2.25), Figure 2.29 shows the true stress- true strain behavior for all the conditions.

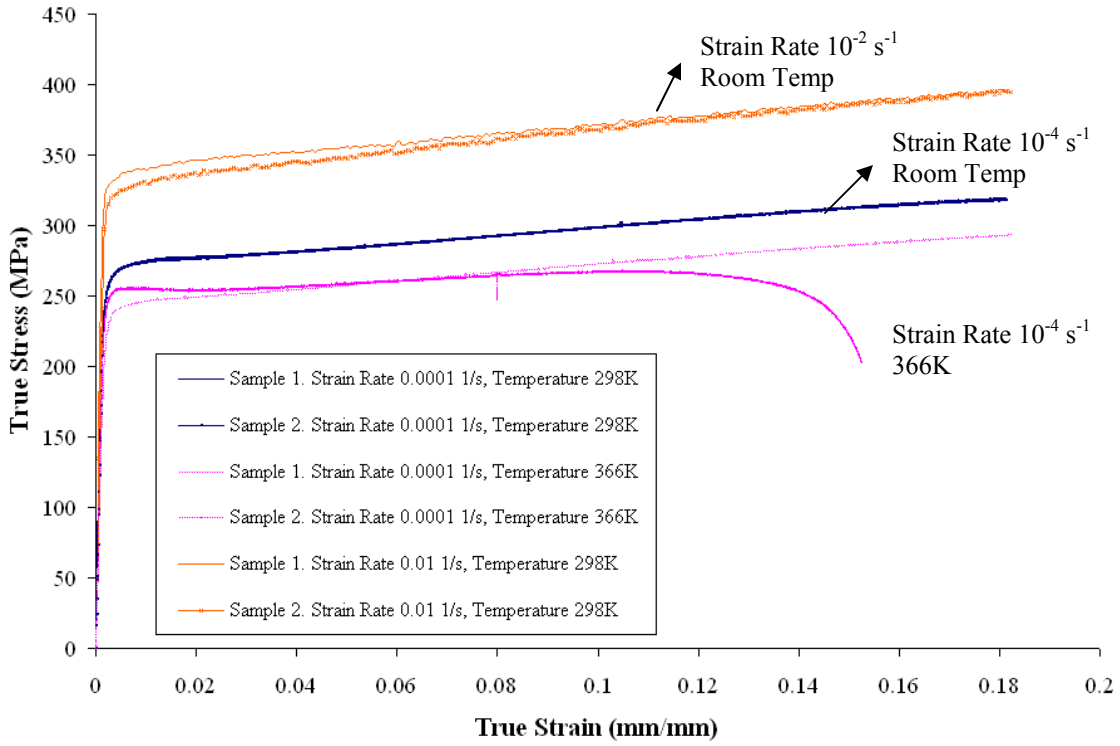

Figure 2.29. True Stress – True Strain behavior of trunk lid. Samples located in different zones (Refer to Fig. 2.25).

The yield point value is higher for the higher strain rate (10^{-2} s^{-1}) and is lower for a higher temperature. These results correspond to the predicted in the literature for higher strain rates and higher temperatures, or yield dependence on strain rates and temperature. Some difference on yield strength and other properties can be observed between the samples.

SEM images were taken to analyze the fractured surface of these samples. Figure 2.30 shows an image of the trunk lid material and Figure 2.31 shows the image analysis results (object area). The porosity at failure was obtained using ImageAnalyzer. The pores area fraction was 0.24, the pore sizes varied from 0.7μm to 4μm.

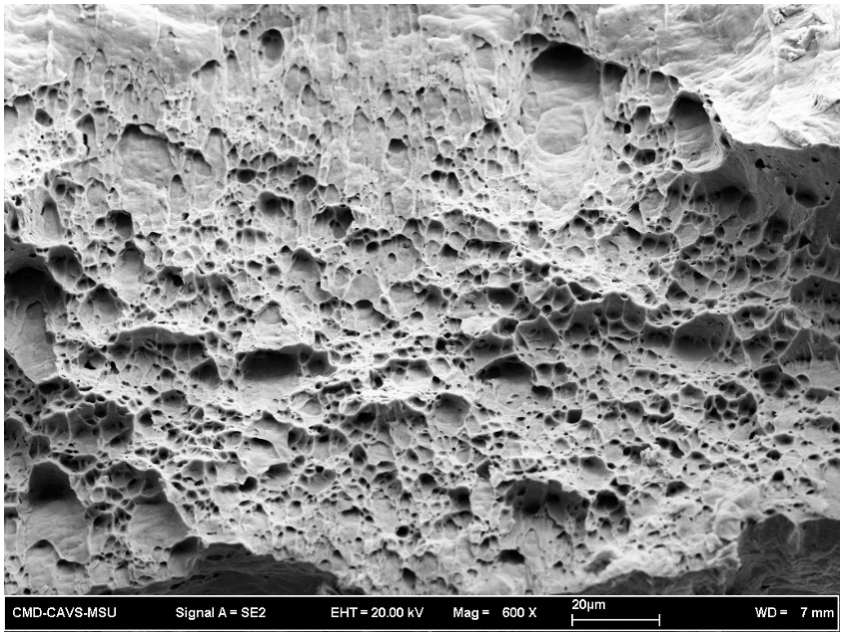

Figure 2.30. SEM image of trunk lid uniaxial tension specimen fracture surface at ambient temperature, strain rate of 10^{-4} s^{-1} for Sample 1

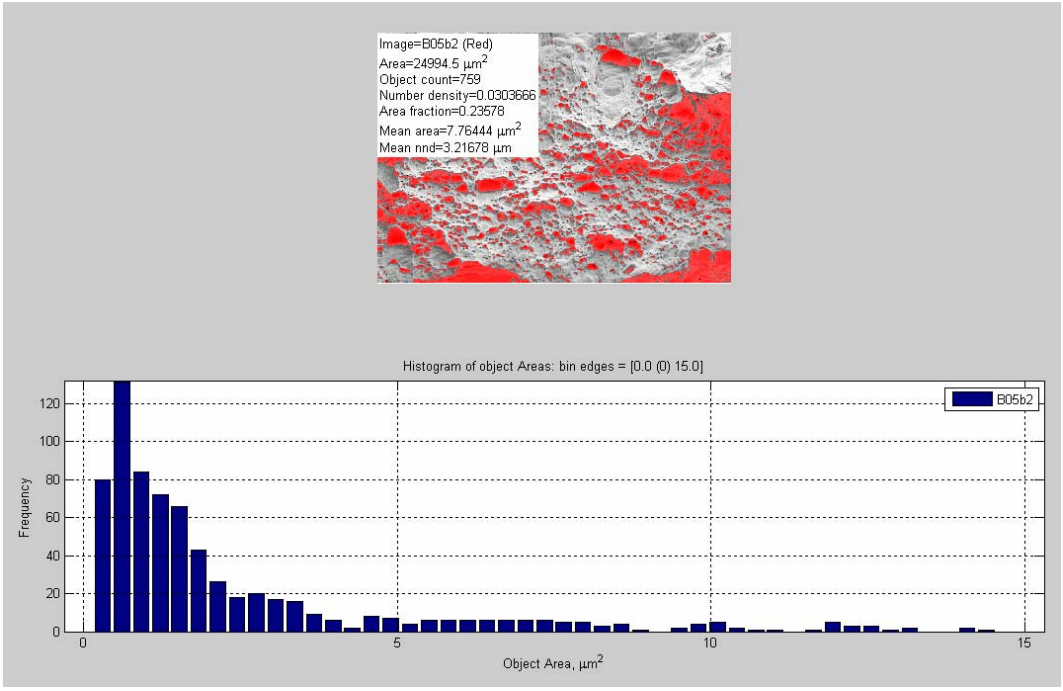

Figure 2.31. Image analysis results of trunk lid material with pore area distribution plot of Sample 1, strain rate of 10^{-4} s^{-1} at ambient temperature

The properties of the trunk lid material are summarized in Table 2.8. As it was mentioned before, some differences depending on the sample location can be observed. Although these differences are not marked, they can be attributed to minor differences that the microstructure presented depending on the location. Since these differences do not vary largely from sample to sample, it can be assumed that the properties are distributed homogenously throughout the component.

Microalloyed steels and bake-hardening steels are usually used in automotive industry for vehicle closures [ASM Specialty Handbook, 1996]. The alloy composition, microstructure and mechanical properties of this material can describe either of these materials since both are very low carbon steels with carbide/nitride formers as Niobium and/or Titatium. Since the grain size of this material is not very fine as it usually is in microalloyed steels, it is presumed that this material is bake-hardening steel.

Table 2.8

Mechanical and structure properties of trunk lid material

	Mechanical Properties	***Zone 1***	***Zone 2***
10-4 s-1 Amb. Temp.	Young's Modulus (GPa)	175.9	173.5
	Yield Point (MPa)	252.2	261.5
	Ultimate Strength (MPa)	318.6	319.1
	Strain to failure (%)	24	25
	Energy Absorption ($J/m^3 *10^6$)	76.4	79.7
10-4 s-1 366K	Young's Modulus (GPa)	173	165.8
	Yield Point (MPa)	246.6	230.6
	Ultimate Strength (MPa)	293.5	266.2
	Strain to failure (%)	15	22
	Energy Absorption ($J/m^3 *10^6$)	70.4	66.5
10-2 s-1 Amb. Temp.	Young's Modulus (GPa)	124	158
	Yield Point (MPa)	314.9	319.2
	Ultimate Strength (MPa)	394.7	396.6
	Strain to failure (%)	23	24
	Energy Absorption ($J/m^3 *10^6$)	94.7	99.1
	Vickers Hardness	131.4	133.7
	Microstructure Properties		
	Grain Size (main) (μm)	14.7	13
	Grain aspect ratio (width/length)	0.43	0.39
	Particle size (μm)	1.29	1.21
	Particle density	0.061	0.081
	Distance Particle - Particle (μm)	2.2	1.2
	Particle area fraction	0.048	0.046
	Void size (μm)	1.92	0.77
	Void density	0.086	0.14
	Final void area fraction	0.23	0.13

2.4.4 Outer Doors

The Dodge Neon doors were also critical components in the side impact crash scenarios. The alloy element concentration was obtained using mass spectrometry and the results are presented in Table 2.9.

Table 2.9

Door material element concentration

Element	Concetration %
Fe	67.2
C	1.29
Mn	0.27
Ni	0.122
Cu	0.454
Ti	0.103
Cr	0.05
Al	2.31
Nb	0.004
V	0.003
N	0.492
Mg	0.089
Zn	0.036
Others	27.3

The material samples of the doors were extracted from different locations in the component in order to obtain grain size distribution along the vehicle part. The objective of this analysis is to map or distribute this characteristic in the finite element mesh as will be presented in the following chapters. Figure 2.32 shows the location of the samples in the door.

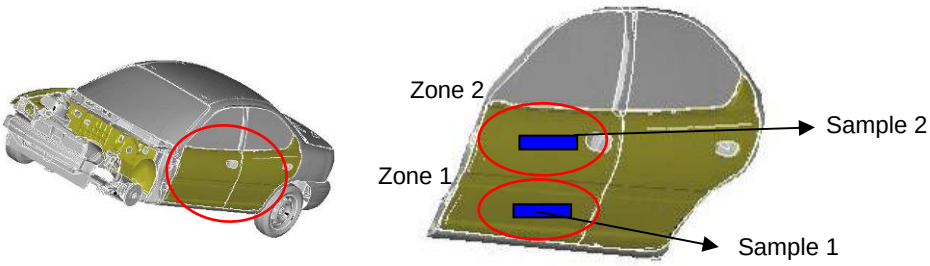

Figure 2.32. Sample location in the outer door.

The microstructure that corresponds to these locations is shown in Figure 2.33. Grain size distribution of these samples was determined and the values are shown in Figure 2.34.

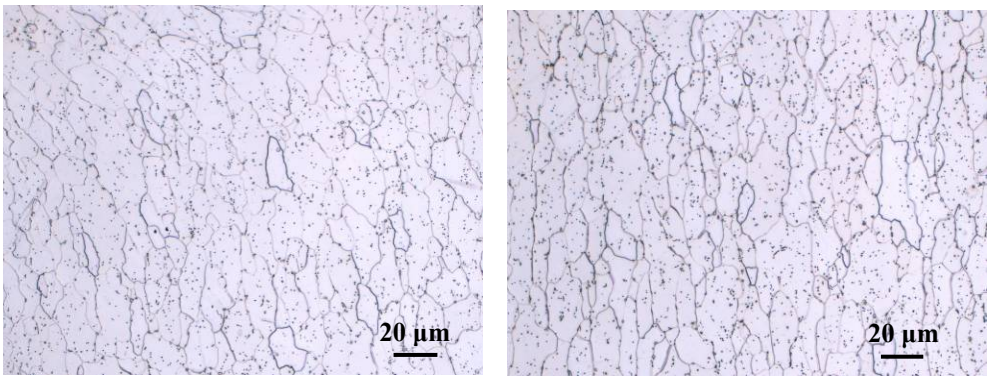

(a) (b)

Figure 2.33. Outer door material optical micrographs at two different locations (Refer to Fig. 2.30). (a) Sample 1; (b) Sample 2.

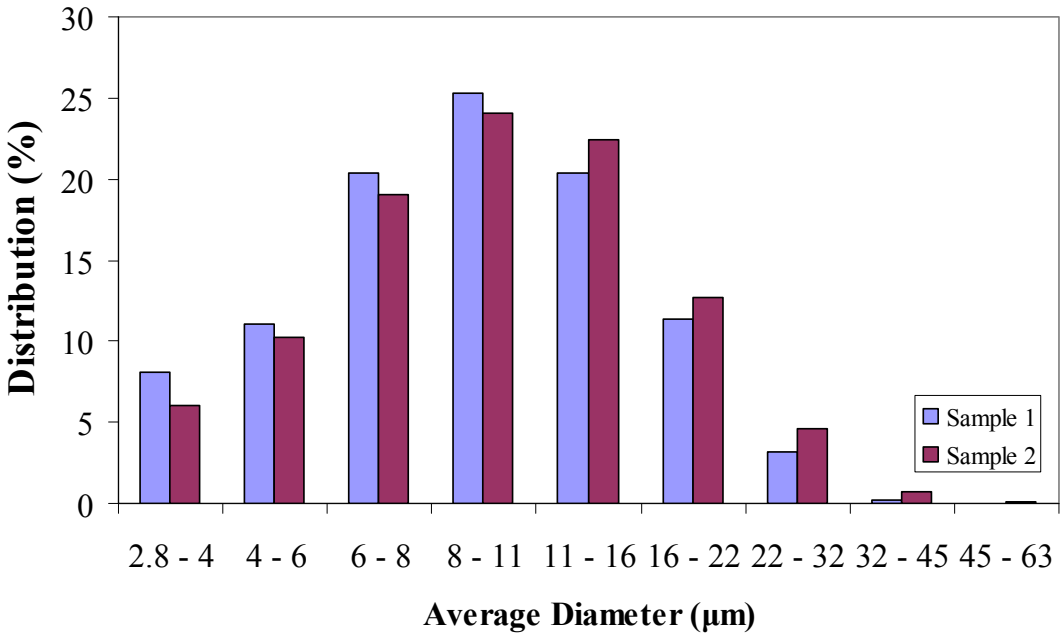

Figure 2.34. Grain size distribution of outer door Samples 1 and 2.

The microstructure of this material is similar to the trunk lid material. However, the chemical composition obtained does not correspond to this kind of steels since the carbon content is too high. It is possible that during the execution of the spectrometry of this material some human errors were committed [AISI, 2002].

The micrographs on Figure 2.33 are composed by a ferrite matrix with very fine precipitates throughout the ferrite grains. The ferrite grain sizes varied from 2.8 µm to 63 µm but the greatest distribution of grains corresponded to average diameters of 8 µm to 11 µm. Particle size was obtained from optical micrographs using ImageAnalyzer. The particle sizes obtained varied from 1.27 µm to 5 µm. The Vickers hardness of these samples is shown in Figure 2.35.

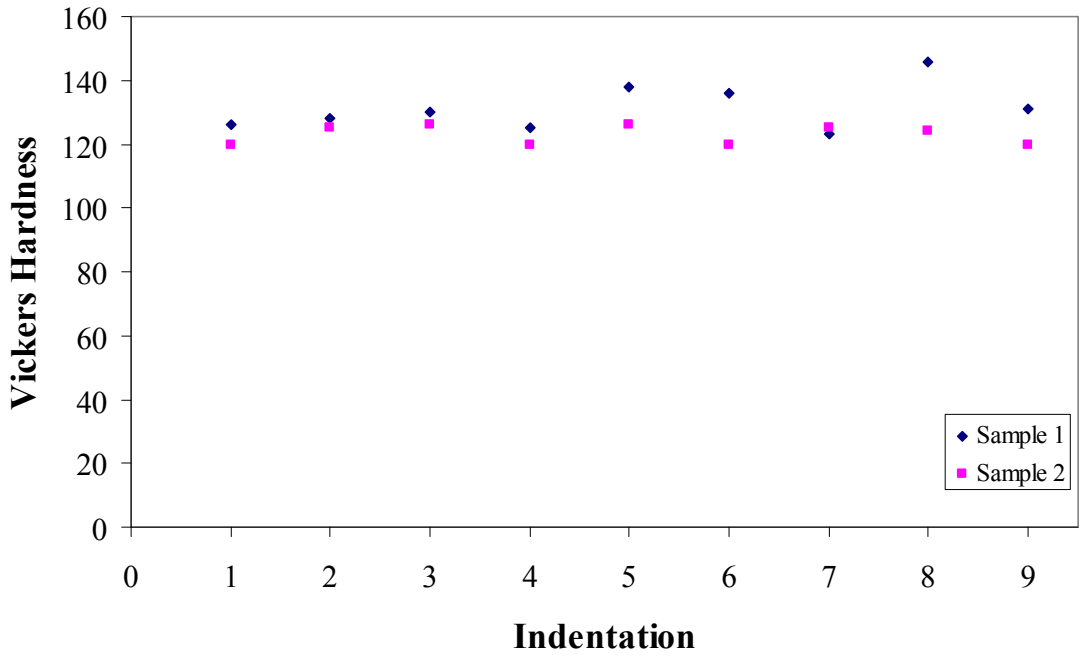

Figure 2.35. Vickers hardness distribution on outer door Samples 1 and 2.

The Vickers hardness values varied between 119 HV to 127 HV, giving a mean value of 123±3 HV. The hardness distribution was homogeneous as observed in Figure 2.35. Refer to Figure 2.6 for indentation locations.

Using the mean value of the Vickers hardness of these samples, the yield stress was obtained using Equation 2.3. A value of 359MPa was obtained. Tension results obtained for the Samples are shown in Figure 2.36.

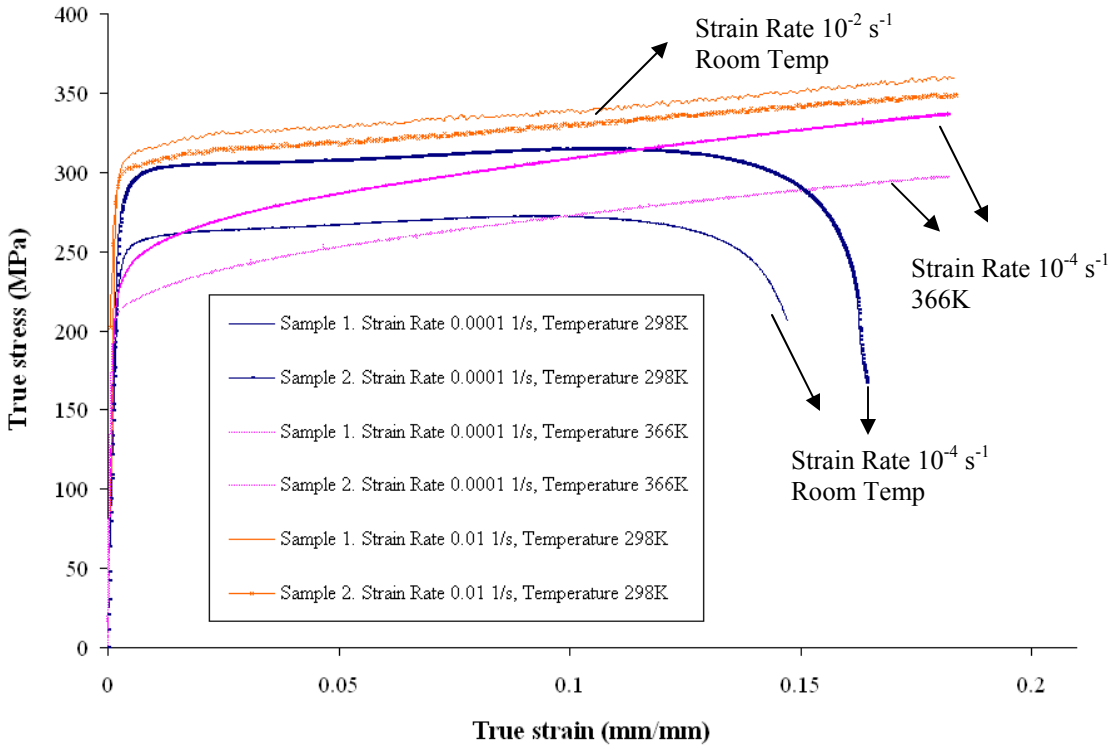

Figure 2.36. True Stress – True Strain behavior of outer door. Samples located in different zones (Refer to Fig. 2.32).

The yield point value is higher for the higher strain rate (10^{-2} s^{-1}) and is lower for a higher temperature. These results correspond to the predicted in the literature for higher strain rates and higher temperatures. The results obtained for the outer door material in the range for plain carbon steels. Differences in the stress – strain behavior between samples can be observed in Figure 2.36. A change in the slope of the plastic zone for high temperature is observed comparing to the rest of the conditions. This represents more hardening of the material at the higher temperature.

SEM images were taken to analyze the fractured surface of these samples. Figure 2.37 shows an image of the outer door material and Figure 2.38 shows the image analysis

results (object area). The porosity at failure was obtained using ImageAnalyzer. The pores area fraction was 0.11, the pore sizes varied from 0.58μm to 6μm.

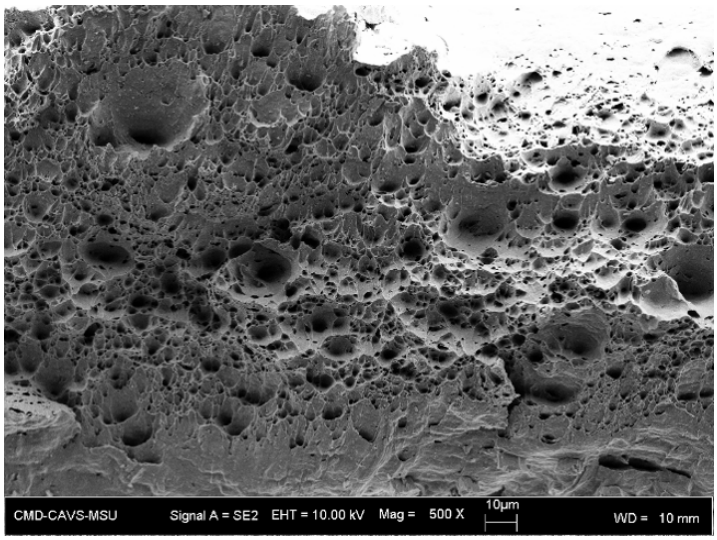

Figure 2.37. SEM image of outer door frame uniaxial tension specimen fracture surface at ambient temperature, strain rate of 10^{-4} s^{-1} for Sample 1.

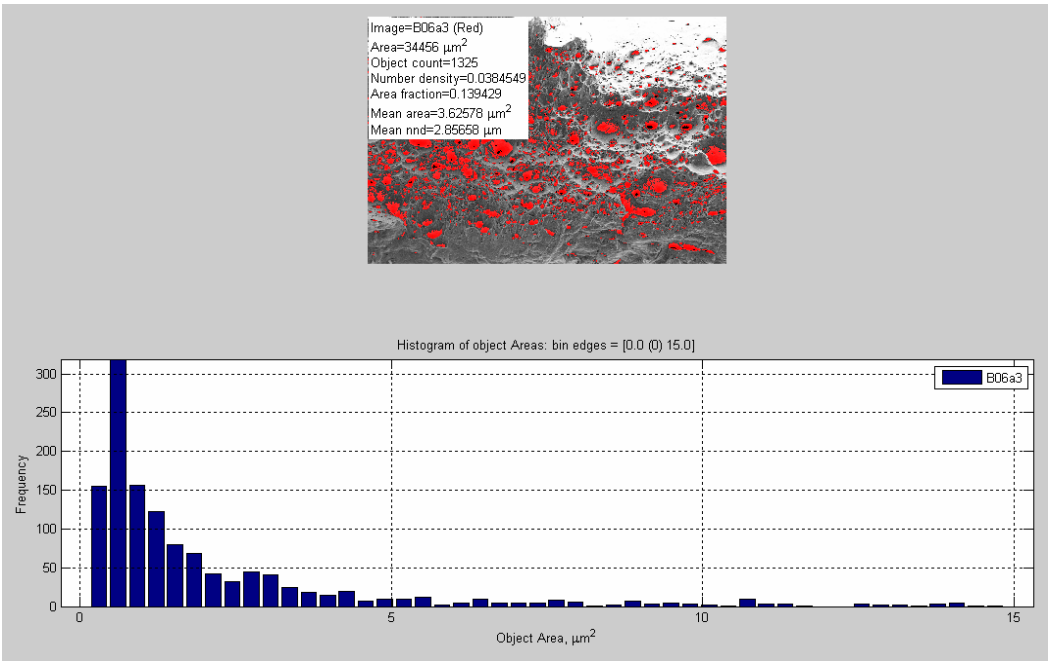

Figure 2.38. Image analysis results of outer door material with pore area distribution plot of Sample 1, strain rate of 10^{-4} s^{-1} at ambient temperature.

The microstructure and mechanical properties of this material describe either a microalloyed steel or a bake-hardneable steel similar to the trunk lid (both components are closures). The outer door microstructure-properties can be summarized in Table 2.10.

Table 2.10

Mechanical and structure properties of outer door material

	Mechanical Properties	***Zone 1***	***Zone 2***
10-4 s-1 Amb. Temp.	Young's Modulus (GPa)	152.3	134.4
	Yield Point (MPa)	283.1	242.3
	Ultimate Strength (MPa)	319.4	314.8
	Strain to failure (%)	17	17
	Energy Absorption ($J/m^3 *10^6$)	54.2	53.5
10-4 s-1 366K	Young's Modulus (GPa)	129.2	76.7
	Yield Point (MPa)	210.1	231.1
	Ultimate Strength (MPa)	337.4	298.4
	Strain to failure (%)	23	24
	Energy Absorption ($J/m^3 *10^6$)	77.6	71.6
10-2 s-1 Amb. Temp.	Young's Modulus (GPa)	129.2	76.7
	Yield Point (MPa)	280.6	280.8
	Ultimate Strength (MPa)	353	366.1
	Strain to failure (%)	23	22
	Energy Absorption ($J/m^3 *10^6$)	81.1	80.5
	Vickers Hardness	155.7	155.3
	Microstructure Properties		
	Grain Size (main) (μm)	13.99	14.9
	Grain aspect ratio (lentgh/with) (μm)	0.4	0.44
	Particle size (μm)	0.66	0.68
	Particle density	0.1	0.083
	Particle - Particle distance (μm)	2	1.3
	Particle area fraction	0.78	0.75
	Void size (μm)	0.53	0.58
	Void density	0.115	0.136
	Final void area fraction	0.1	0.11

2.45 Front Fenders

The Dodge Neon front fenders were also critical components in the front and offset impact crash scenarios. The alloy element concentration was obtained using mass spectrometry and the results are presented on Table 2.11.

Table 2.11

Front fender material element concentration

Element	Concetration %
Fe	99.6
C	0.0015
Mn	0.135
Al	0.036
Cr	0.02
Nb	0.029
W	0.015
Ti	0.016
V	0.0019
Cu	0.012
Sb	0.011
Others	0.122

Following the same procedure as the components presented before, the material samples of the front fenders were extracted from different locations. The objective of this analysis is to map or distribute this characteristic in the finite element mesh in future analysis. Figure 2.39 shows the location of the samples in the fender.

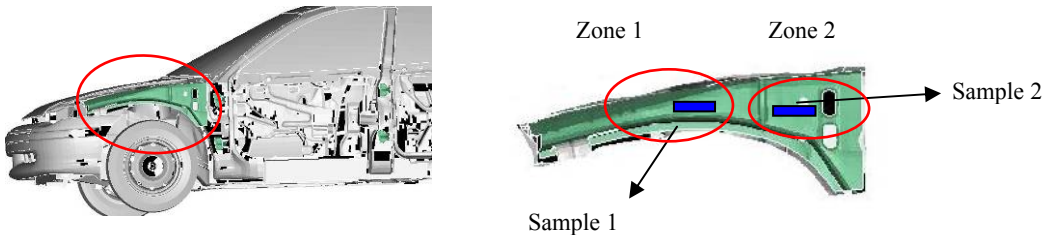

Figure 2.39. Sample location in the front fender.

The microstructure that corresponds to these locations is shown in Figure 2.40. Grain size distribution of these samples was executed and the values are shown in Figure 2.41.

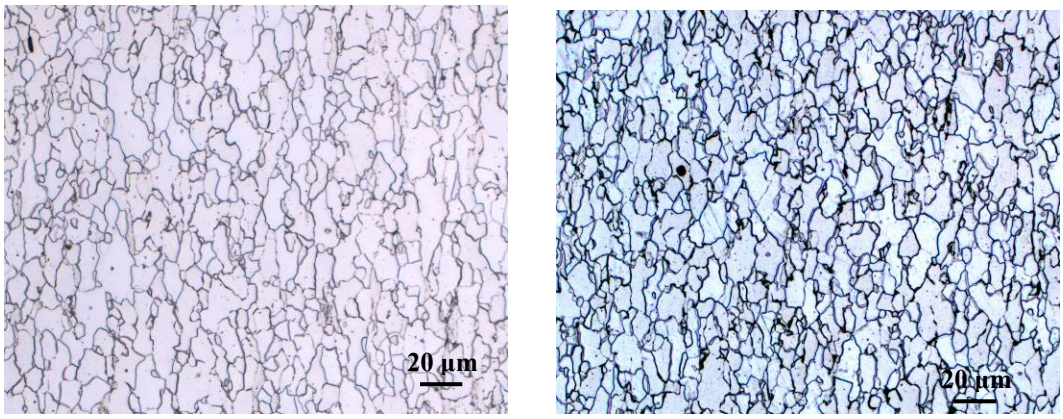

(a) (b)

Figure 2.40. Front fender material optical micrographs at two different locations (Refer to Fig. 2.38). (a) Sample 1; (b) Sample 2.

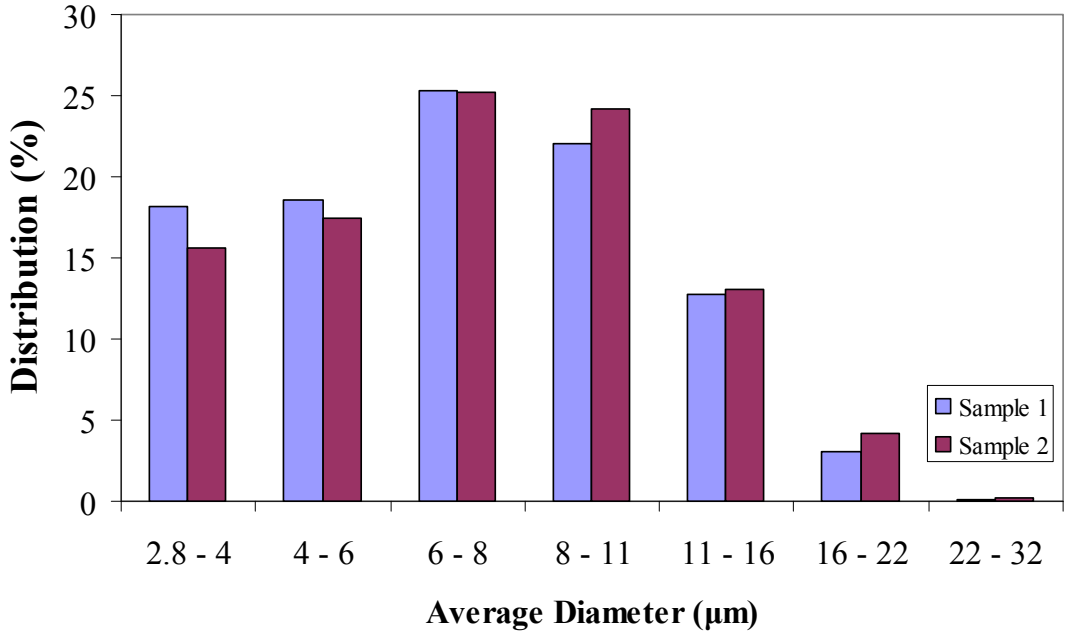

Figure 2.41. Grain size distribution of front fender Samples 1 and 2

The microstructure presents a ferrite matrix and some precipitates (darker phase). The microstructure was found to be similar to the suspension frame material. The ferrite grain sizes varied from 2.8 µm to 22 µm but the greatest distribution of grains corresponded to average diameters of 6 µm to 8 µm, which represents a fine grain.

Precipitates can be observed around grain boundaries. Since this material contains Nb, Ti and V, it is presumed that these precipitates are NbC, VC or TiC. Particle size was obtained from optical micrographs using ImageAnalyzer. The particle sizes obtained varied from 1 µm to 3 µm. The Vickers hardness of these samples is shown in Figure 2.42.

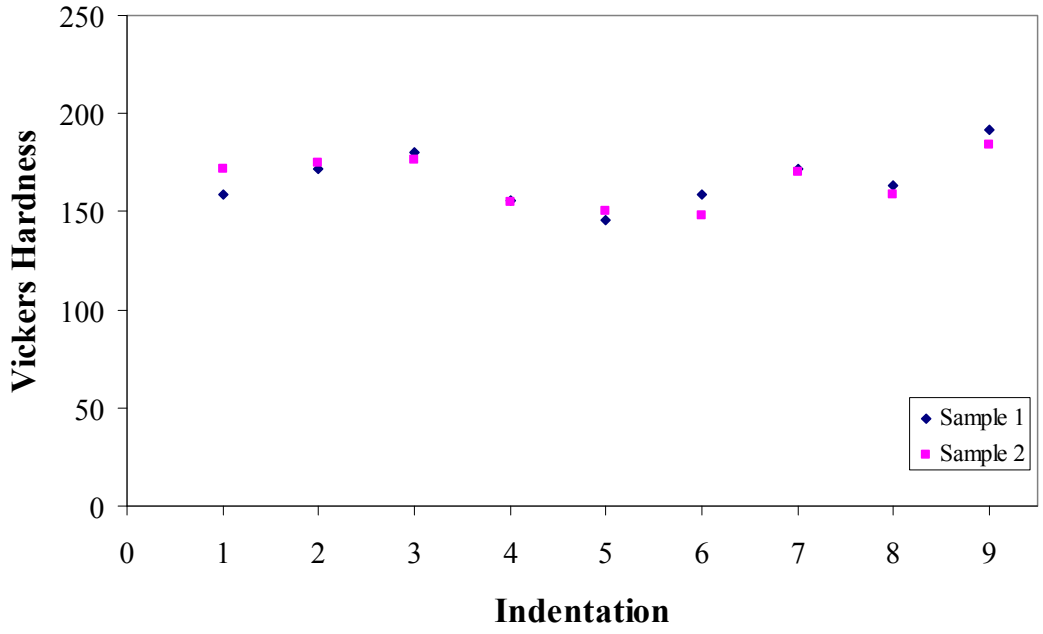

Figure 2.42. Vickers hardness distribution on front fender Samples 1 and 2

The Vickers hardness values varied between 155 HV to 192 HV, giving a mean value of 166±12 HV. The hardness distribution was homogeneous as observed in Figure 2.42. Refer to Figure 2.6 for indentation locations.

Using the mean value of the Vickers hardness of these samples, the yield stress was obtained using Equation 2.3. A value of 342MPa was obtained. Tension results obtained for the different samples are shown in Figure 2.43

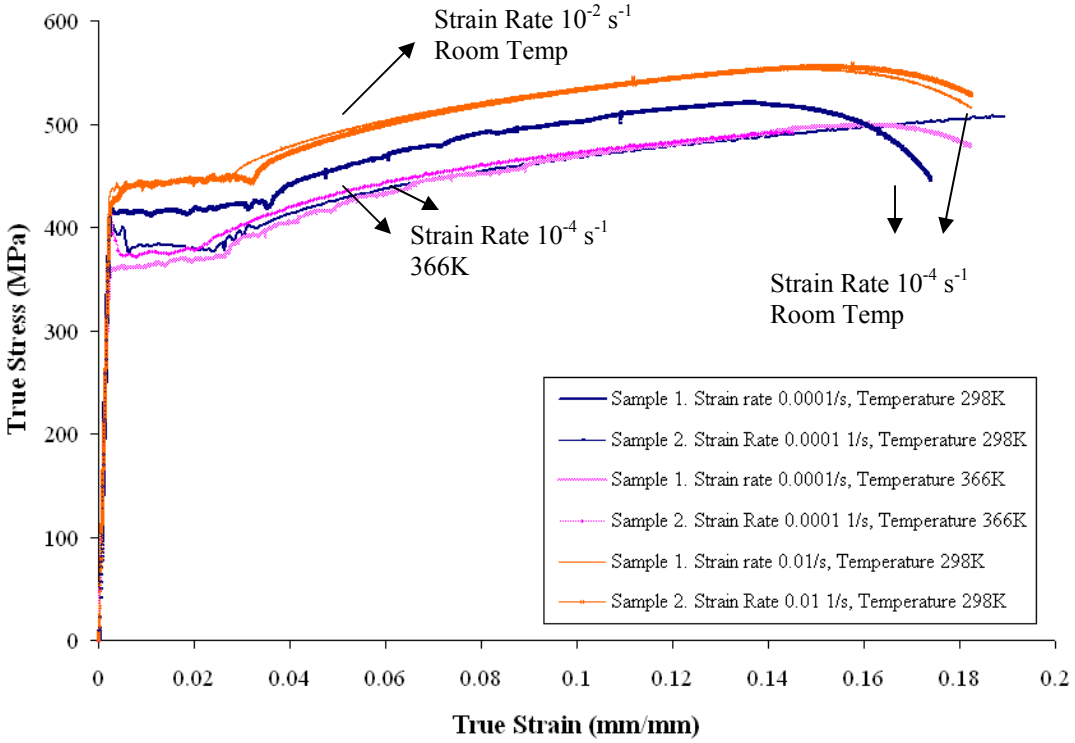

Figure 2.43. True Stress – True Strain behavior of front fender. Samples located in different zones (refer to Fig. 2.39)

The yield point at the higher strain rate (10^{-2} s^{-1}) was the highest. The yield at higher temperature was lower than at room temperature. These results correspond to the predicted in the literature for steels since they show strain rate and temperature dependence on yield point. The results obtained for the front fender material are not in the range for plain carbon steels. Slight differences are observed comparing the behavior of both Samples.

SEM images were taken to analyze the fractured surface of these samples. Figure 2.44 shows an image of the outer door material and Figure 2.45 shows the image analysis results (object area). The porosity at failure was obtained using ImageAnalyzer. The pores area fraction was 0.13, the pore sizes varied from 0.4 μm to 4 μm.

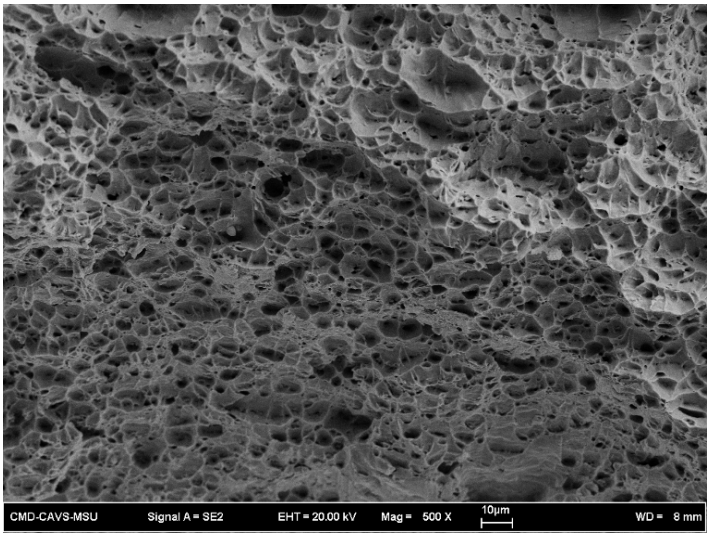

Figure 2.44. SEM image of front fender tension specimen fracture surface at ambient temperature and strain rate of 10^{-4} s^{-1} for Sample 1.

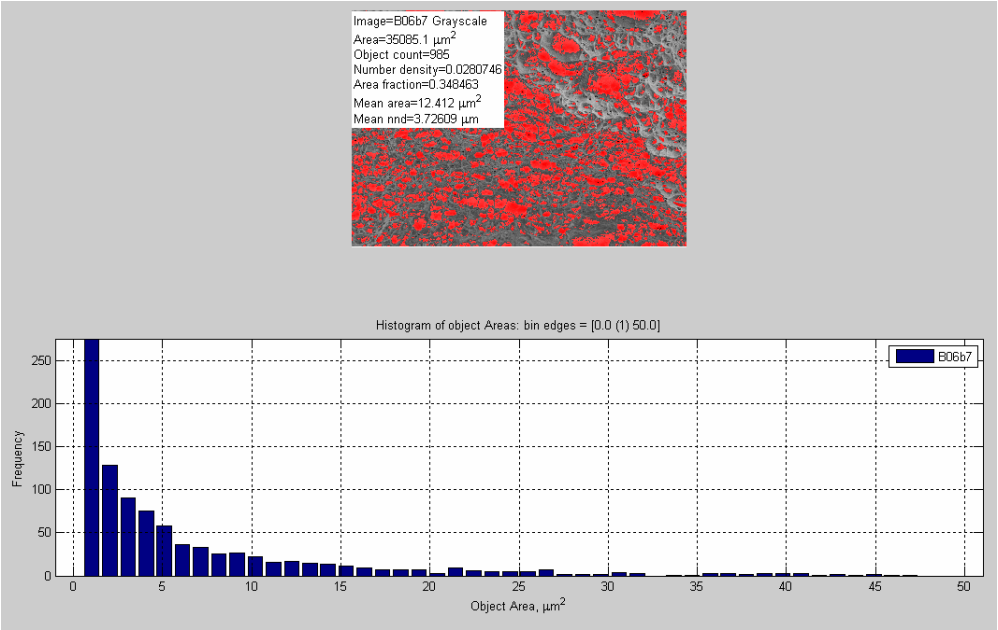

Figure 2.45. Image analysis results of front fender with pore area distribution plot of Sample 1, strain rate of 10^{-4} s^{-1} at ambient temperature

The alloy composition, microstructure and mechanical properties of this material describe a microalloyed steel [AISI, 2002].

From the stress – strain behavior of this material and the microstructure analyses, the properties shown in Table 2.12 were obtained.

Table 2.12

Mechanical and structure properties of front fender material

	Mechanical Properties	***Zone 1***	***Zone 2***
10-4 s-1 Amb. Temp.	Young's Modulus (GPa)	198.3	201.5
	Yield Point (MPa)	406.9	414.1
	Ultimate Strength (MPa)	507.8	519.6
	Strain to failure (%)	22	18
	Energy Absorption (J/m^3*10^6)	111.7	93.5
10-4 s-1 366K	Young's Modulus (GPa)	217.4	209.3
	Yield Point (MPa)	360.9	412.1
	Ultimate Strength (MPa)	497.7	491.5
	Strain to failure (%)	21	19
	Energy Absorption (J/m^3*10^6)	104.5	93.3
10-2 s-1 Amb. Temp.	Young's Modulus (GPa)	214.6	194.1
	Yield Point (MPa)	438.7	430.5
	Ultimate Strength (MPa)	553.1	555.7
	Strain to failure (%)	19	20
	Energy Absorption (J/m^3*10^6)	105	111.1
	Vickers Hardness	216.5	217.6
Microstructure Properties			
	Grain Size (main) (μm)	10.3	12.11
	Grain aspect ratio	0.3	0.39
	Particle size (μm)	0.66	0.68
	Particle density	0.081	0.082
	Distance Particle - Particle (μm)	3.2	2.9
	Particle area fraction	0.062	0.058
	Void size (μm)	0.43	0.43
	Void density	0.13	0.083
	Final void area fraction	0.13	0.12

As it was mentioned earlier, some differences in the mechanical properties are observed. These differences can be attributed to the variations on the microstructure (grain size, particle size, etc.). The differences are not marked; therefore it can be assumed that the properties are homogeneous throughout the fender.

2.4.6 Hood

The hood was also critical components in the front and offset impact crash scenarios. The alloy element concentration was obtained using mass spectrometry and the results are presented on Table 2.13.

Table 2.13

Hood material element concentration

Element	Concetration %
Fe	78.4
C	0.493
Si	1.32
Cu	0.294
Mn	0.159
Al	0.114
N	0.113
Ti	0.097
Nb	0.095
Ni	0.081
La	0.045
Co	0.043
Zn	0.036
Ta	0.035
S	0.03
P	0.023
Cr	0.02
Others	0.087

The material samples of the hood were extracted from different locations in the component in order to obtain grain size distribution along the vehicle part. Figure 2.46 shows the location of the samples in the hood.

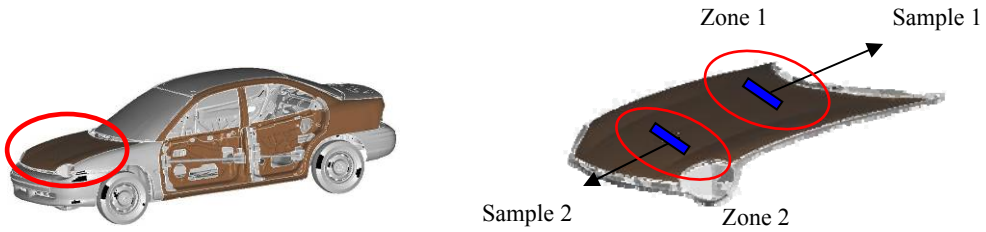

Figure 2.46. Sample location in the hood.

The microstructure that corresponds to these locations is shown in Figure 2.47. Grain size distribution of these samples was executed and the values are shown in Figure 2.48.

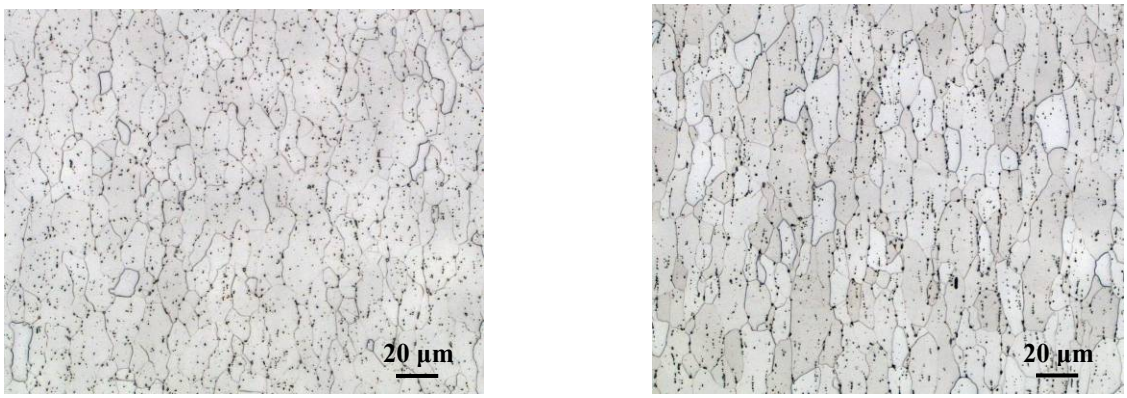

(a) (b)

Figure 2.47. Hood material optical micrographs at two different locations (Refer to Fig. 2.46). (a) Sample 1; (b) Sample 2.

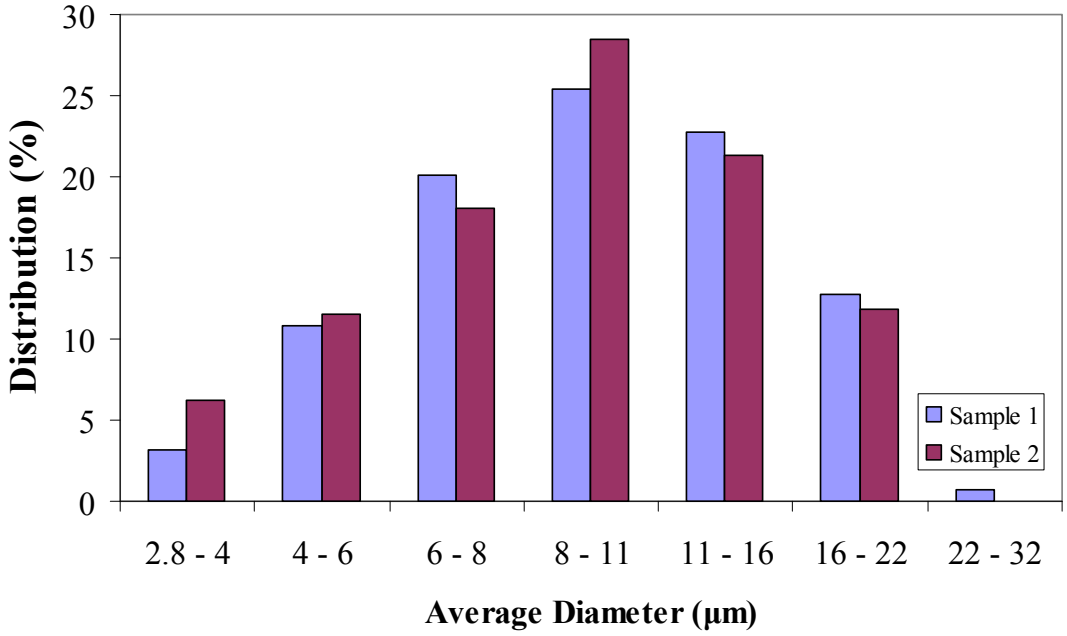

Figure 2.48. Grain size distribution of hood Samples 1 and 2.

This microstructure is similar to the trunk and the door. However, it can be observed that the chemical composition presents a medium content of carbon [ASM Handbook, 2002]. The microstructure of Figure 2.47 does not correspond to this carbon content on steels. Therefore, it is presumed that human errors were committed during the execution of the spectrometry.

The similarity with the trunk and door material was expected since these components are the automobile's closures [ASM Specialty Handbook, 1996]. The micrographs in Figure 2.47 show a ferrite matrix with very fine precipitates throughout the ferrite grains. The ferrite grain sizes varied from 2.8 µm to 22 µm but the greatest distribution of grains corresponded to average diameters of 11 µm to 8 µm. The precipitates are unevenly distributed inside the ferrite grains. The particle sizes obtained

varied from 0.6 μm to 3 μm. The Vickers hardness of these samples is shown in Figure 2.49.

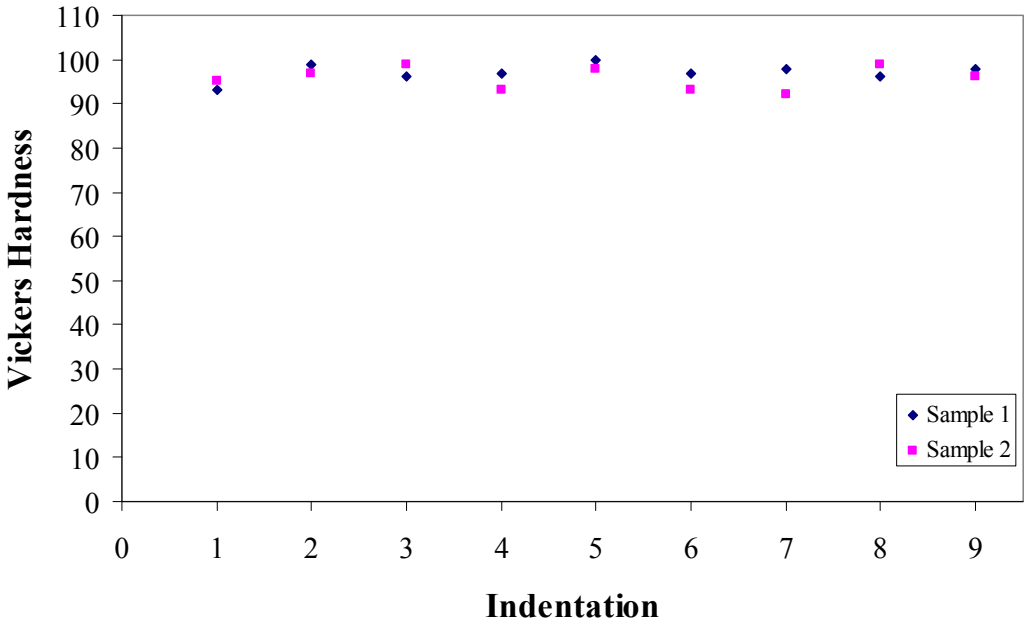

Figure 2.49. Vickers hardness distribution on hood Samples 1 and 2.

The Vickers hardness values varied between 95 HV to 100 HV, giving a mean value of 96±2 HV. The hardness distribution was homogeneous as observed in Figure 2.49. Refer to Figure 2.6 for indentation locations.

Using the mean value of the Vickers hardness of these samples, the yield stress was obtained using Equation 2.3. A value of 208MPa was obtained.

Tension experiments were performed and the behavior obtained of this material is shown in Figure 2.50.

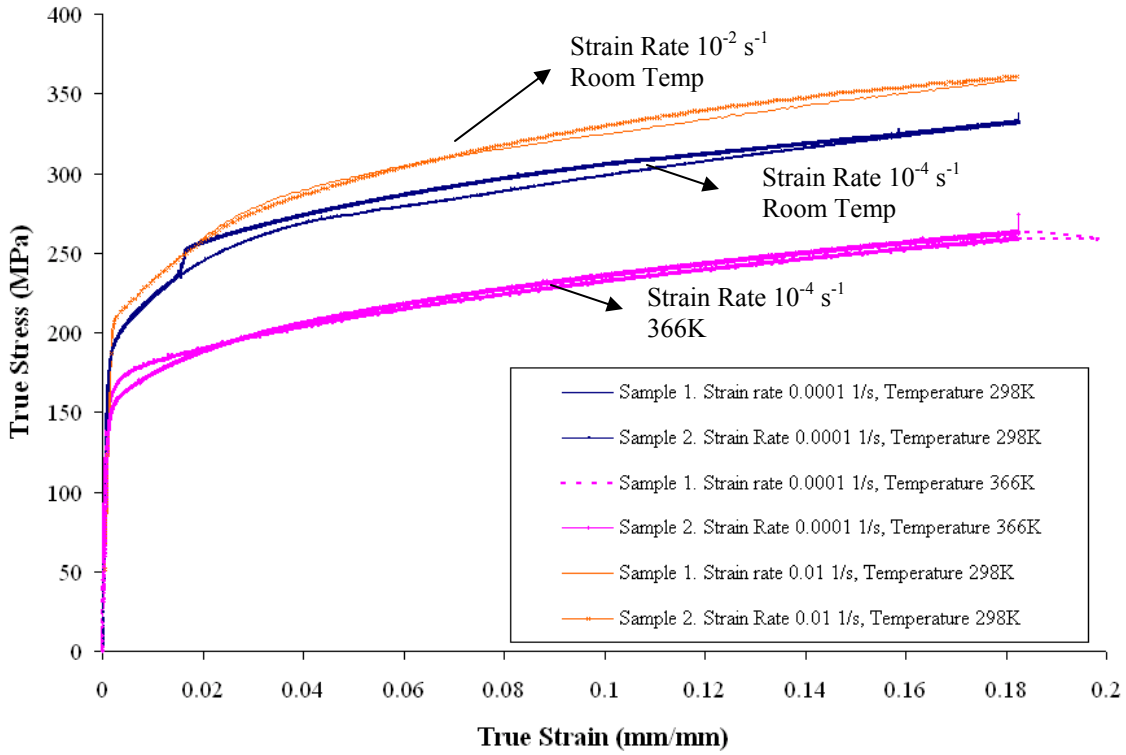

Figure 2.50. True Stress – True Strain behavior of hood. Samples located in two different zones (Refer to Fig. 2.46)

The yield points from Table 2.14 and from Figure 2.50 present strain rate and temperature dependence. This behavior is expected in steels as it been mentioned earlier in this chapter. The yield strength obtained from the hardness is differs between 10 to 20 MPa from the experimental value. The highest yield point corresponded to the higher strain rate (10^{-2} s^{-1}). The yield for the higher temperature was lower than at room temperature. These results correspond to the predicted in the literature for steels as the results obtained in previous sections of this chapter. There is almost no difference between the stress-strain behaviors of the samples in each condition.

SEM images were taken to analyze the fractured surface of these samples. Figure 2.51 shows an image of the outer door material and Figure 2.52 shows the image analysis

results (object area). The porosity at failure was obtained using ImageAnalyzer. The pores area fraction was 0.12, the pore sizes varied from 0.2 μm to 4 μm.

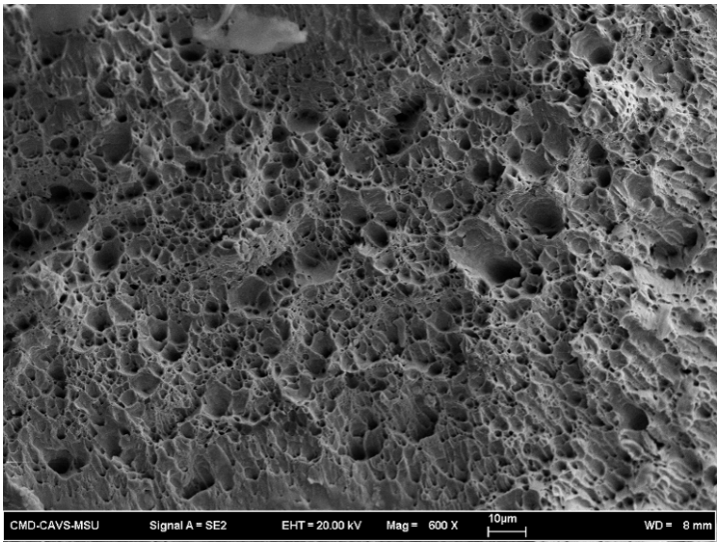

Figure 2.51. SEM image of hood tension specimen fracture surface at ambient temperature and strain rate of 10^{-4} s^{-1} for Sample 1.

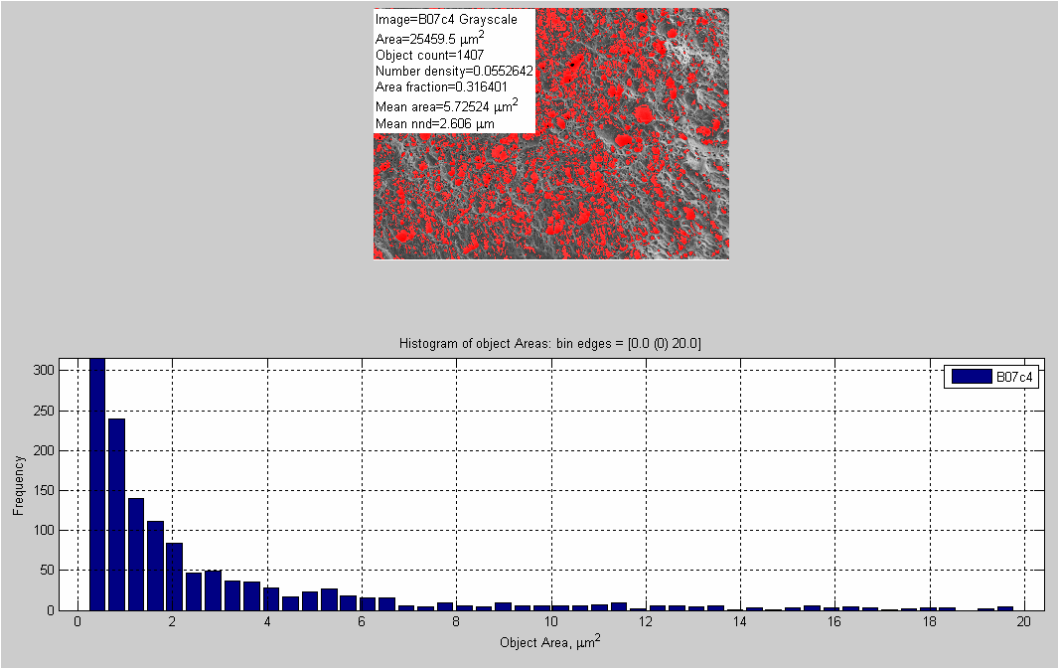

Figure 2.52. Image analysis results of hood with pore area distribution plot of Sample 1, strain rate of 10^{-4} s^{-1} at ambient temperature

The microstructure and mechanical properties of this material describe either microalloyed steel or bake-hardening steel. [AISI, 2002]. From the stress – strain curves and microstructure analyses, the properties shown in Table 2.14 were obtained.

Table 2.14

Mechanical and structure properties of hood material

	Mechanical Properties	***Zone 1***	***Zone 2***
10-4 s-1 Amb. Temp.	Young's Modulus (GPa)	181.7	178.8
	Yield Point (MPa)	154.5	148.6
	Ultimate Strength (MPa)	281.25	279.12
	Strain to failure (%)	28	27
	Energy Absorption (J/m^3*10^6)	78.75	75.3624
10-4 s-1 366K	Young's Modulus (GPa)	120.5	134.9
	Yield Point (MPa)	128.5	128.1
	Ultimate Strength (MPa)	219.6	223.5
	Strain to failure (%)	26	27
	Energy Absorption (J/m^3*10^6)	57.096	60.345
10-2 s-1 Amb. Temp.	Young's Modulus (GPa)	86.1	112.2
	Yield Point (MPa)	196.4	187
	Ultimate Strength (MPa)	303.5	301.7
	Strain to failure (%)	26	26
	Energy Absorption (J/m^3*10^6)	105	111.1
	Vickers Hardness	97.1	95.7
	Microstructure Properties		
	Grain Size (main) (μm)	14.8	12.4
	Grain aspect ratio	0.54	0.36
	Particle size (μm)	0.7	0.77
	Particle density	0.057	0.063
	Distance Particle - Particle (μm)	2.2	2.3
	Particle area fraction	0.052	0.065
	Void size (μm)	0.37	0.27
	Void density	0.129	0.184
	Final void area fraction	0.092	0.121

The structure-properties vary slightly depending on the location of the two samples. However, the variation is not considerable. This characteristic explains the similarities of the stress – strain behavior. It is assumed then that the properties are homogeneous throughout the hood.

2.4.7 Front Chassis

The front chassis was also a critical component the different impact crash scenarios. The alloy element concentration was obtained using mass spectrometry and the results are presented on Table 2.15.

Table 2.15

Front chassis material element concentration

Element	Concetration %
Fe	98.8
C	0.069
Mn	0.87
Si	0.11
Al	0.04
Cu	0.011
Nb	0.004
V	0.007
Ni	0.0073
Zn	0.034
N	0.014
Sb	0.0025
Se	0.017
Others	0.0142

The material samples of the front chassis were extracted from different locations in the component in order to obtain grain size distribution along the vehicle part as in the rest of the components studied earlier. Figure 2.53 shows the location of the samples in the front chassis.

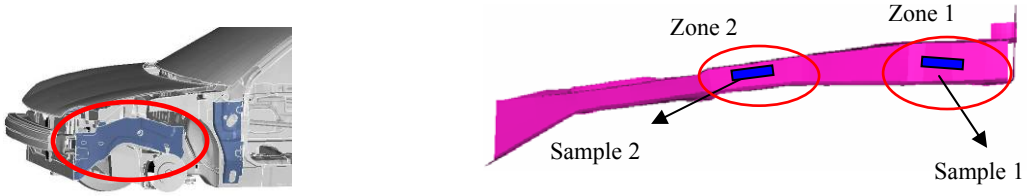

Figure 2.53. Sample location in the chassis rail

The microstructure that corresponds to these locations is shown in Figure 2.54. Grain size distribution of these samples was executed and the values are shown in Figure 2.55.

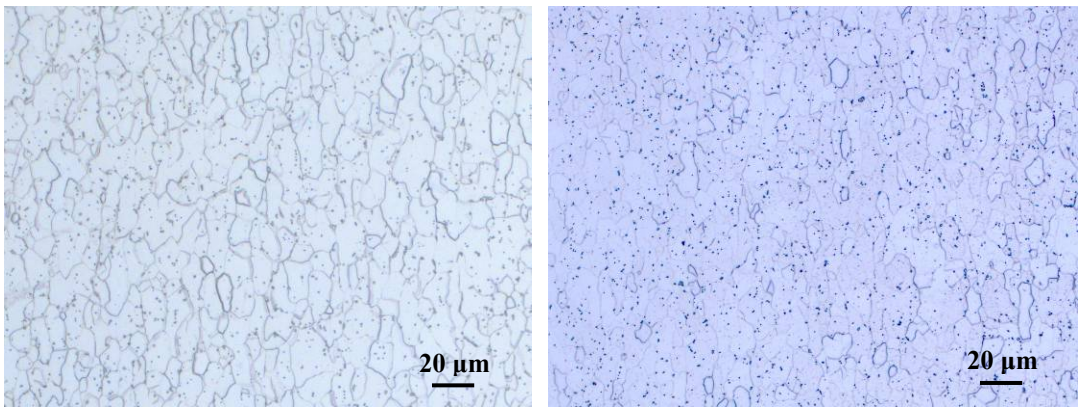

Figure 2.54. Front chassis material optical micrographs at two different locations (Refer to Fig. 2.52). (a) Sample 1; (b) Sample 2

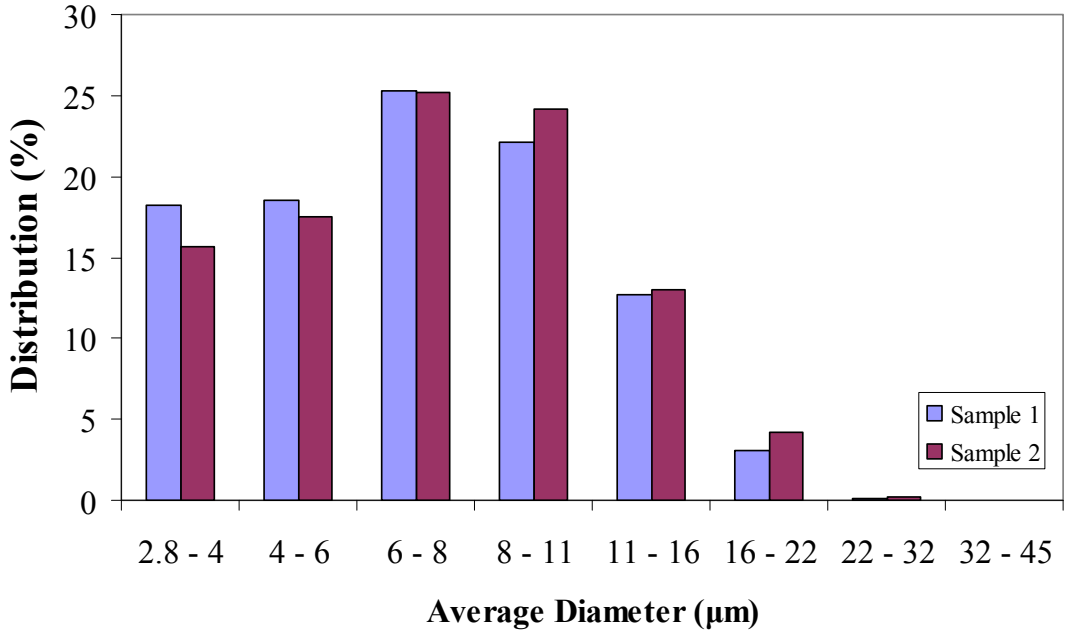

Figure 2.55. Grain size distribution of front chassis Samples 1 and 2

The microstructure of Figure 2.54 is composed of a ferrite matrix and fine precipitates. The ferrite grain sizes varied from 2.8 µm to 22 µm but the greatest distribution of grains corresponded to average diameters of 6 µm to 8 µm. The precipitates are observed unevenly distributed inside the ferrite grains. From the composition of Table 2.15, it is presumed that the particles are NbC or VC. Particle size was obtained from optical micrographs using ImageAnalyzer. The particle sizes obtained varied from 0.7 µm to 1.5 µm. The Vickers hardness of these samples is shown in Figure 2.56.

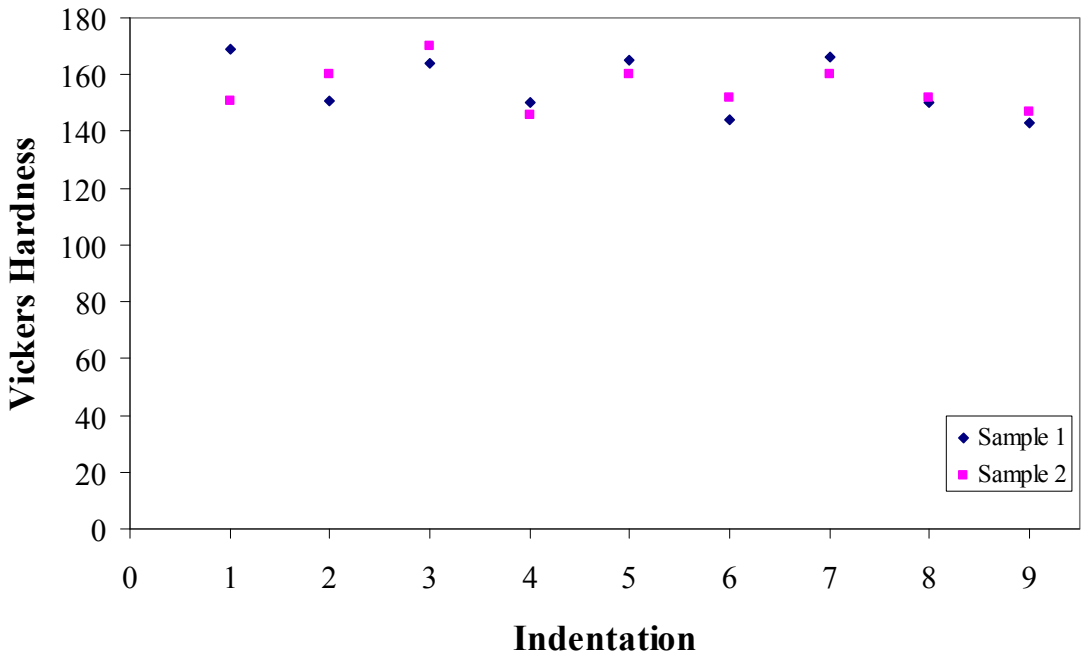

Figure 2.56. Vickers hardness distribution on chassis Samples 1 and 2

The Vickers hardness values varied between 143 HV to 165 HV, giving a mean value of 155±8 HV. The hardness distribution was homogeneous as observed in Figure 2.56. Refer to Figure 2.6 for indentation locations.

Using the mean value of the Vickers hardness of these samples, the yield stress was obtained using Equation 2.3. A value of 402 MPa was obtained. Tension results obtained for the samples are presented in Figure 2.57.

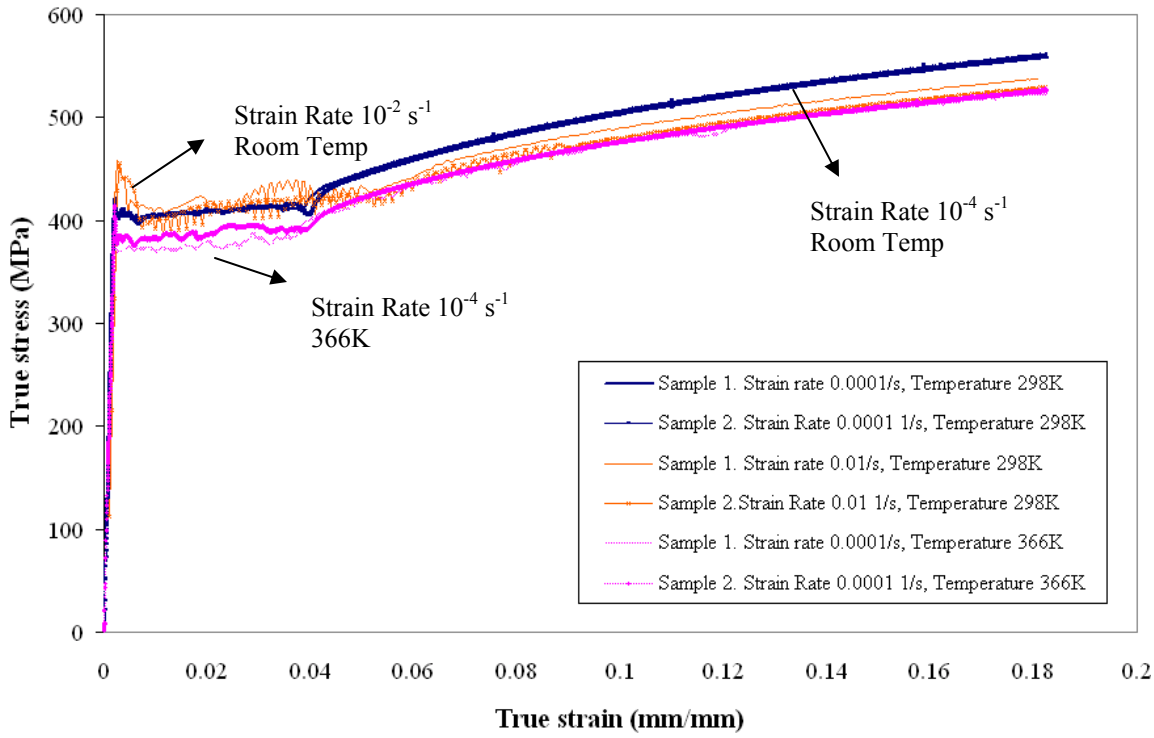

Figure 2.57. True Stress – True Strain behavior of front chassis rail. Samples located in two different zones (Refer to Fig. 2.53)

Strain rate and temperature dependence on yield can be observed in Figure 2.57. The yield point value is higher for the higher strain rate (10^{-2} s^{-1}). At the higher temperature, the yield strength was lower compared to that at room temperature. These results correspond to the predicted in the literature for steels. The results obtained for the front chassis material are higher than the values found in handbooks for plain carbon steels. The strain to failure for strain rate at ambient temperature was 10^{-4} s^{-1} was 25%, for 10^{-2} s^{-1} was 23% and for the high temperature test was 27%

SEM images were taken to analyze the fractured surface of these samples. Figure 2.58 shows an image of the outer door material and Figure 2.59 shows the image analysis results (object area). The porosity at failure was obtained using ImageAnalyzer. The pores area fraction was 0.2, the pore sizes varied from 0.3 μm to 3.2 μm.

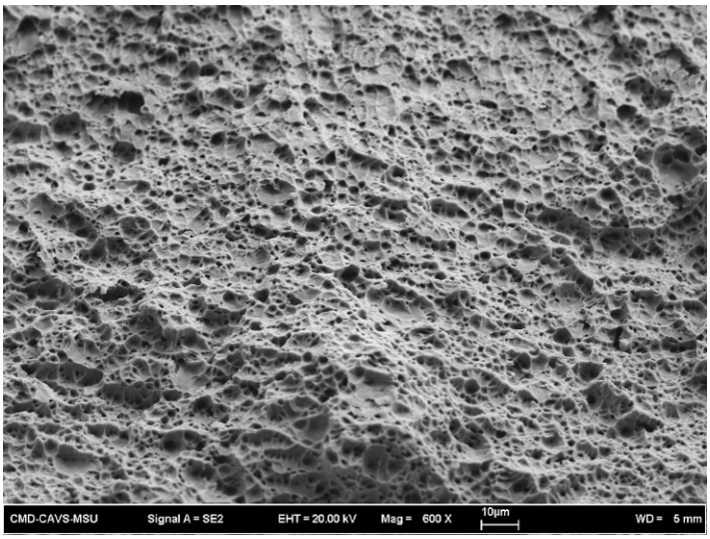

Figure 2.58. SEM image of chassis rail tension specimen fracture surface at ambient temperature and strain rate of 10^{-4} s^{-1} for Sample 1.

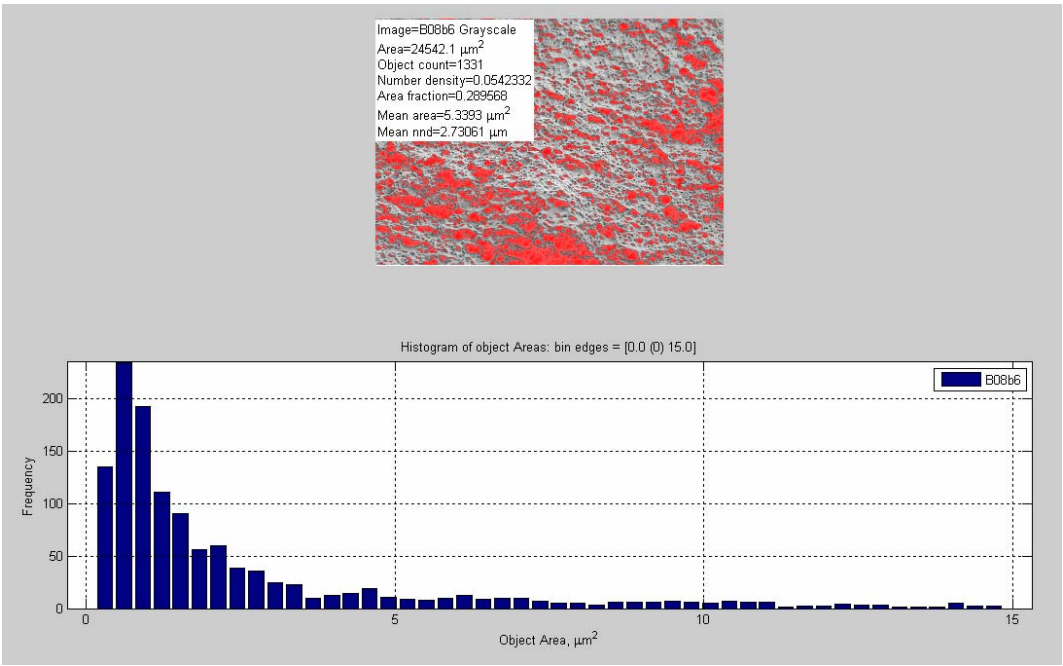

Figure 2.59. Image analysis results of chassis rail with pore area distribution plot of Sample 1, strain rate of 10^{-4} s^{-1} at ambient temperature

The alloy composition, microstructure and mechanical properties of this material describe microalloyed steel. [AISI, 2002]. From the stress – strain behavior and microstructure characteristics, the properties shown in Table 2.16 were obtained.

Table 2.16

Mechanical and structure properties of front chassis rail material

Mechanical Properties		***Zone 1***	***Zone 2***
10-4 s-1 Amb. Temp.	Young's Modulus (GPa)	218.4	225.9
	Yield Point (MPa)	413.1	409.1
	Ultimate Strength (MPa)	561.5	559.4
	Strain to failure (%)	26	25
	Energy Absorption (J/m^3*10^6)	145.99	139.85
10-4 s-1 366K	Young's Modulus (GPa)	233.6	237.3
	Yield Point (MPa)	371.6	324.1
	Ultimate Strength (MPa)	523.1	528.3
	Strain to failure (%)	24	24
	Energy Absorption (J/m^3*10^6)	125.544	126.792
10-2 s-1 Amb. Temp.	Young's Modulus (GPa)	206.7	209.9
	Yield Point (MPa)	417.7	429.4
	Ultimate Strength (MPa)	580.2	571.1
	Strain to failure (%)	29	27
	Energy Absorption (J/m^3*10^6)	105	111.1
	Vickers Hardness	155.7	155.3
Microstructure Properties			
	Grain Size (main) (μm)	6.31	7.47
	Grain aspect ratio	0.24	0.39
	Particle size (μm)	0.7	0.72
	Particle density	0.08	0.087
	Distance Particle - Particle (μm)	1.2	1.8
	Particle area fraction	0.024	0.03
	Void size (μm)	0.49	0.38
	Void density	0.33	0.28
	Final void area fraction	0.2	0.178

Some differences can be observed in the mechanical properties. These properties are not marked and can be attributed to small differences in the microstructure depending on the location.

2.4.8 Rear Floorboard

The rear floorboard was also a critical component the different impact crash scenarios. The alloy element concentration was obtained using mass spectrometry and the results are presented on Table 2.17.

Table 2.17

Rear floorboard material element concentration

Element	Concetration %
Fe	99.4
C	0.025
Mn	0.203
Ti	0.037
Zn	0.036
Cr	0.031
Al	0.031
Nb	0.027
Ni	0.017
W	0.016
Cu	0.014
Sb	0.013
Se	0.011
Others	0.057

The material samples of the rear floorboard were extracted from different locations in the component in order to obtain grain size distribution along the vehicle part

as in the components studied earlier. Figure 2.60 shows the location of the samples in the rear floorboard.

Figure 2.60. Sample location in the rear floorboard

The microstructure that corresponds to these locations is shown in Figure 2.61. Grain size distribution of these samples was executed and the values are shown in Figure 2.62.

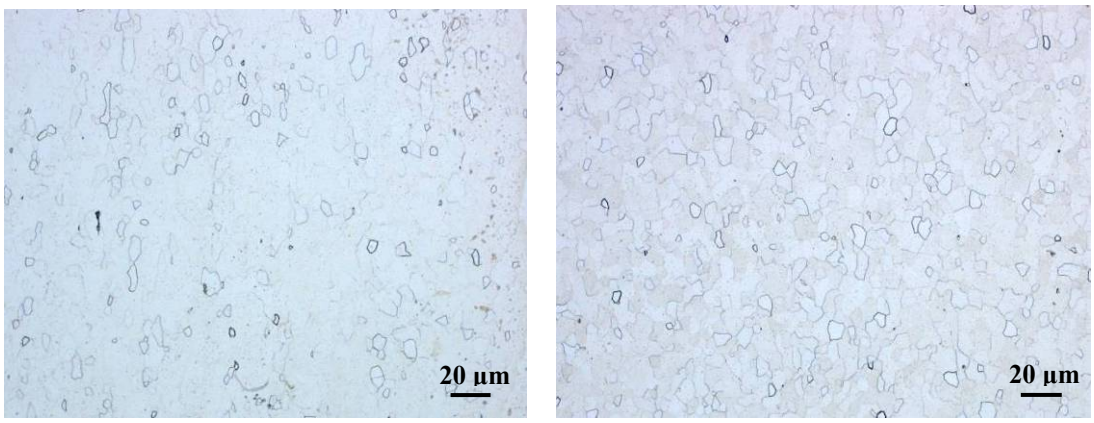

(a) (b)

Figure 2.61. Rear floorboard material optical micrographs at two different locations (Refer to Fig. 2.59). (a) Sample 1; (b) Sample 2

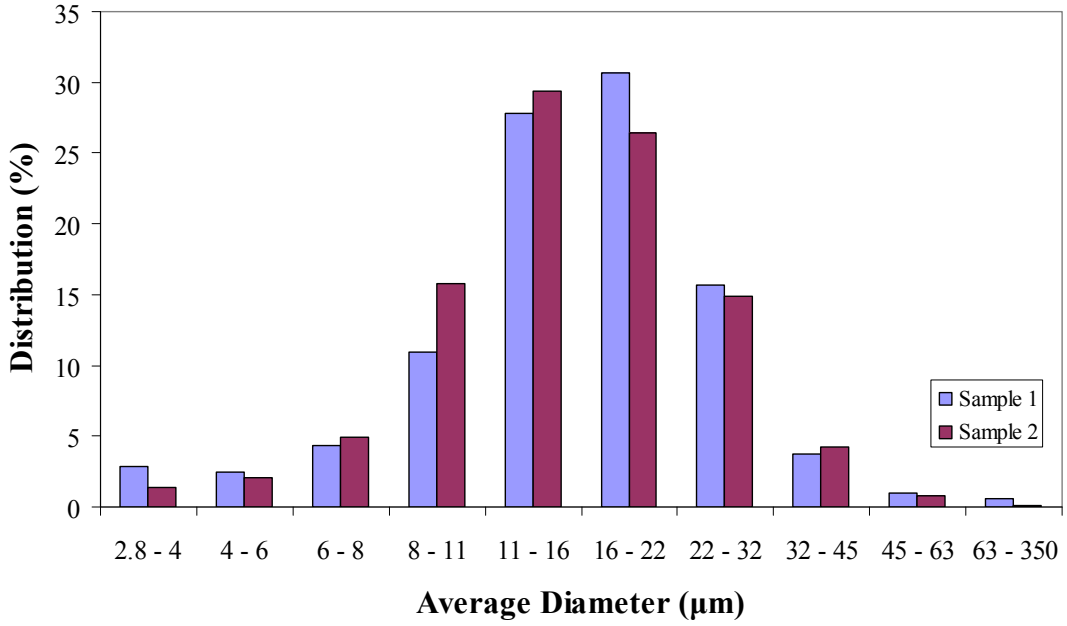

Figure 2.62. Grain size distribution of rear floorboard Samples 1 and 2

A ferrite matrix with an uneven distribution of precipitates throughout it can be observed in Figure 2.61. The ferrite grain sizes varied from 2.8 µm to 63 µm but the greatest distribution of grains corresponded to average diameters of 16 µm to 22 µm. Some yellow-colored inclusions were observed in the optical micrographs with sizes between 2 – 3 µm. The fine precipitates are presumed to be NbC or VC by observing the composition on Table 2.17. The yellow-colored particles can be a kind of nitride or carbonitride.

Further microstructure analysis has to be done in order to characterize the composition of these particles. Particle size of the very fine precipitates was obtained from optical micrographs using ImageAnalyzer. The particle sizes obtained varied from 0.5 µm to 1.5 µm. The Vickers hardness of these samples is shown in Figure 2.63.

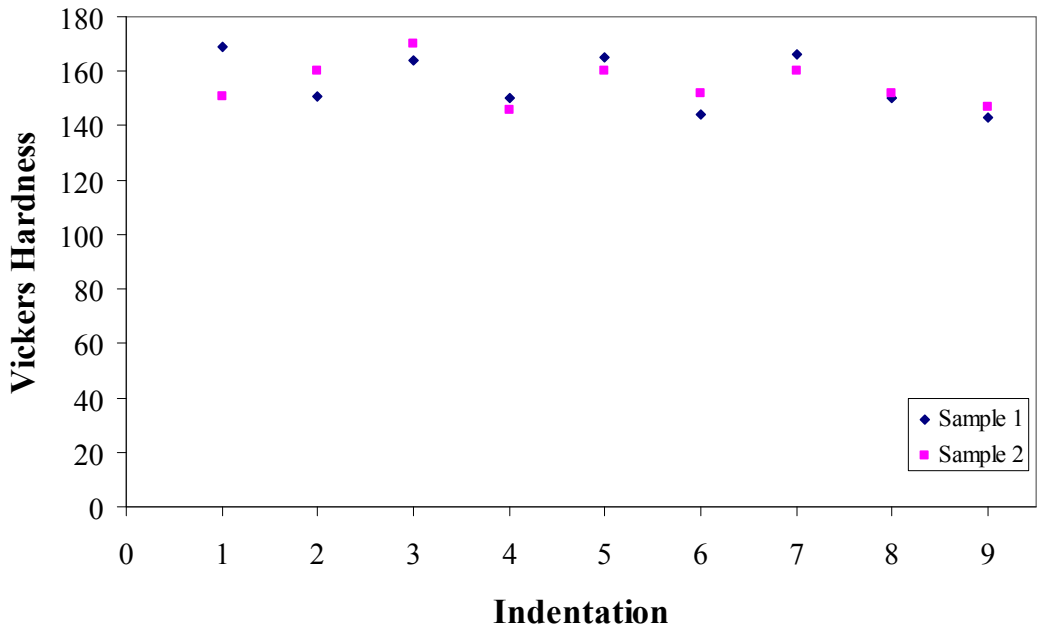

Figure 2.63. Vickers hardness distribution on rear floorboard Samples 1 and 2

The Vickers hardness values varied between 110 HV to 124 HV, giving a mean value of 117±4 HV. The hardness distribution was homogeneous as observed in Figure 2.63. Refer to Figure 2.5 for indentation locations.

Using the mean value of the Vickers hardness of these samples, the yield stress was obtained using Equation 2.3. A value of 402 MPa was obtained.

Tension results obtained for this material for all the conditions are shown in Figure 2.64.

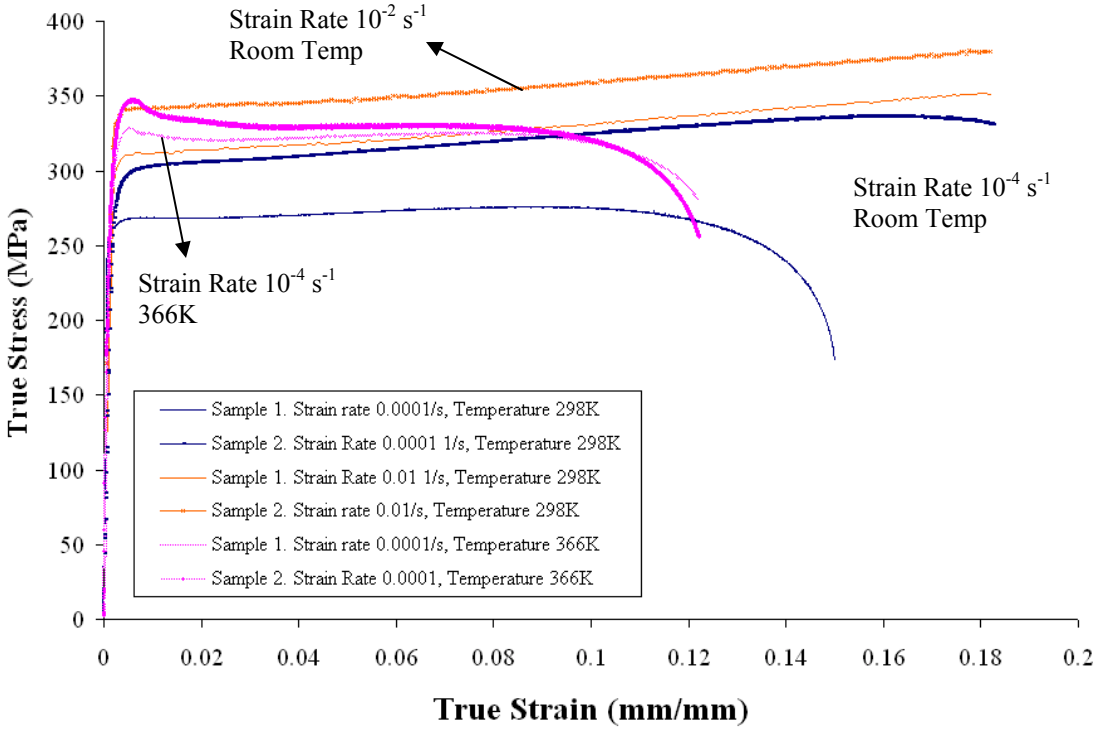

Figure 2.64. True Stress – True Strain behavior of rear floorboard. Samples located in different zones (Refer to Fig. 2.59)

The response obtained for this material presented some anomalies comparing to the expected or predicted in literature. Strain rate dependence on yield can be observed for the two locations. Variation in the stress-strain behavior depending on the location can also be observed. The high temperature response does not correspond to the expected results. Due to time constraints, material availability and faulty test equipment, new experiments could not be performed to corroborate results.

SEM images were taken to analyze the fractured surface of these samples. Figure 2.65 shows an image of the outer door material and Figure 2.66 shows the image analysis results (object area). The porosity at failure was obtained using ImageAnalyzer. The pores area fraction was 0.066, the pore sizes varied from 0.4 μm to 6 μm.

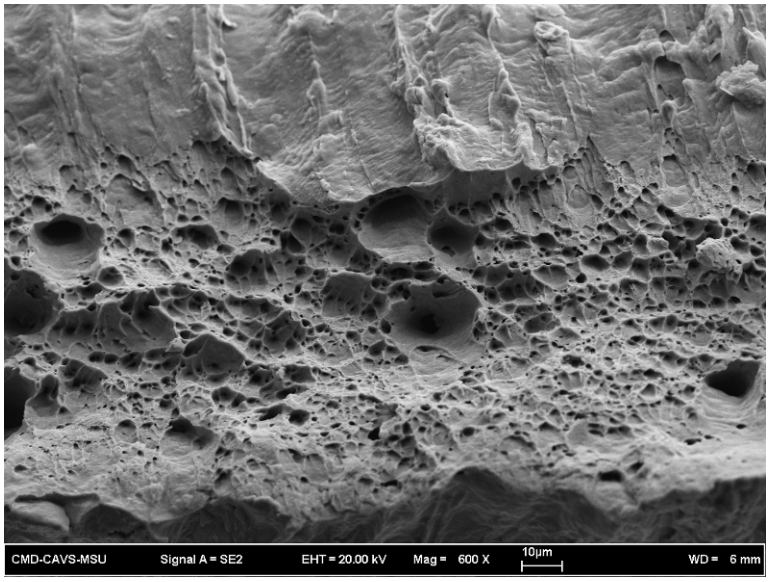

Figure 2.65. SEM image of rear floorboard tension specimen fracture surface at ambient temperature and strain rate of 10^{-4} s^{-1} for Sample 1.

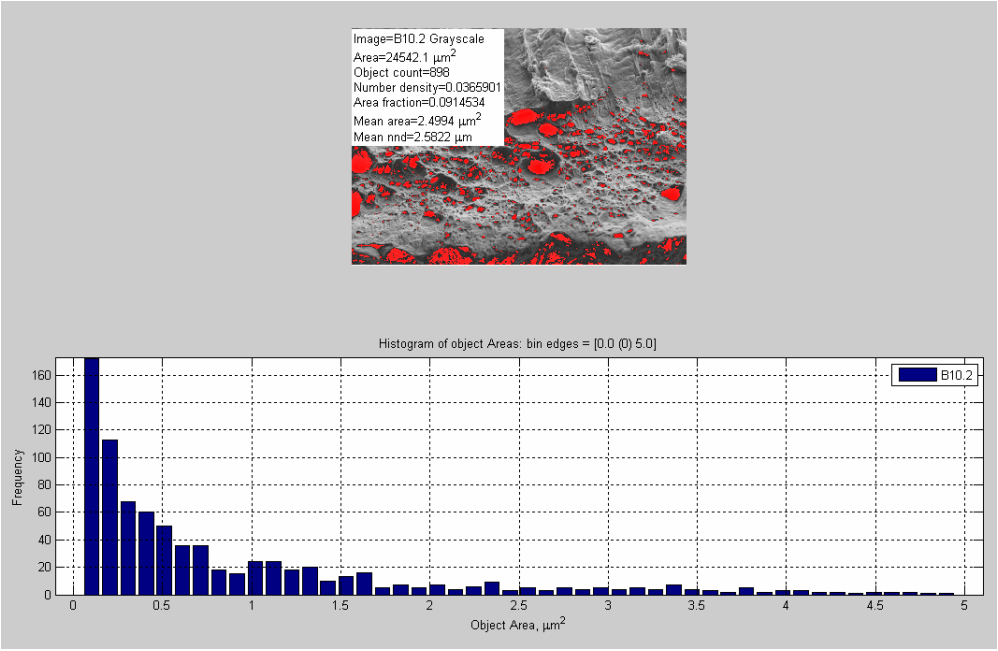

Figure 2.66. Image analysis results of rear floorboard with pore area distribution plot of Sample 1, strain rate of 10^{-4} s^{-1} at ambient temperature

The alloy composition, microstructure and mechanical properties of this material correspond to microalloyed steel. [AISI, 2002]. The rear floorboard properties are shown in Table 2.18 .

Table 2.18

Mechanical and structure properties of rear floorboard material

	Mechanical Properties	***Zone 1***	***Zone 2***
10-4 s-1 Amb. Temp.	Young's Modulus (GPa)	149.4	153.6
	Yield Point (MPa)	237.3	243.7
	Ultimate Strength (MPa)	275.9	336.9
	Strain to failure (%)	13	20
	Energy Absorption ($J/m^3 *10^6$)	35.867	67.38
10-4 s-1 366K	Young's Modulus (GPa)		
	Yield Point (MPa)	318.9	337
	Ultimate Strength (MPa)	328.5	347.1
	Strain to failure (%)	13	13
	Energy Absorption ($J/m^3 *10^6$)	42.705	45.123
10-2 s-1 Amb. Temp.	Young's Modulus (GPa)	119.2	133.5
	Yield Point (MPa)	304.8	330.9
	Ultimate Strength (MPa)	381.2	363.4
	Strain to failure (%)	25	27
	Energy Absorption ($J/m^3 *10^6$)	95.3	98.118
	Vickers Hardness	116.7	117.3
Microstructure Properties			
	Grain Size (main) (μm)	23	19.8
	Grain aspect ratio (width/length)	0.55	0.47
	Particle size (μm)	0.53	0.51
	Particle density	0.18	0.19
	Distance Particle - Particle (μm)	3.03	2.75
	Particle area fraction	0.02	0.014
	Void size (μm)	0.58	0.58
	Void density	0.065	0.059
	Final void area fraction	0.066	0.066

CHAPTER III

MATERIAL MODEL AND FINITE ELEMENT ANALYSIS

3.1 Plasticity – Damage Material Model

An overview of the physics involved in the Internal State Variable model used to define materials in finite element models is presented next.

3.1.1 Kinematics

In continuum mechanics, material deformation can be described using the total deformation gradient $\overline{F}$. The total deformation gradient is decomposed into an elastic $\overline{F}^{e}$, volumetric component of the plastic deformation gradient caused by damage evolution $\overline{F}_{v}^{P}$, and deviatoric component of the plastic deformation gradient due to the plastic deformation within the microstructure $\overline{F}_{d}^{p}$. The total deformation gradient can be written as follows

$$\overline{F} = \overline{F}^{e}\overline{F}_{v}^{P}\overline{F}_{d}^{p} \tag{3.1}$$

The expression above is the multiplicative decomposition of the total deformation gradient and is a modified version by Bammann and Aifantis of the former equation introduced by Lee [Bammann and Aifantis, 1989; Lee, 1969]. Figure 3.1 shows schematically the decomposition explained before.

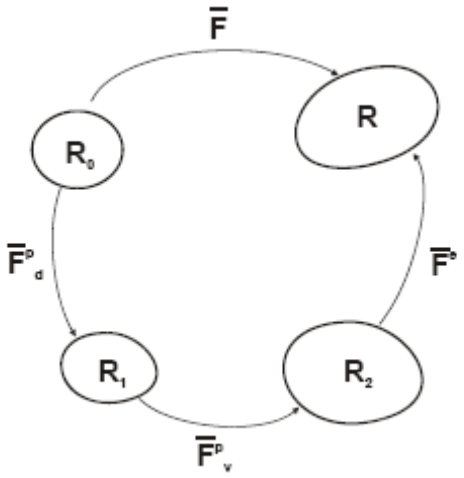

Figure 3.1. Schematic illustration of total deformation gradient and its multiplicative decomposition.

The Jacobian of $\bar{F}^{p}$ is related to change in volume or change in density as result of void growth and nucleation that causes the ductile failure of a material. This value must be positive.

$$J = \det \underline{F}_{v}^{P} = \frac{V_2}{V_0} = \frac{\rho_0}{\rho_2} \tag{3.2}$$

The volume and density, V_0 and ρ_0, correspond to the reference configuration. When the configuration changes from State 0 to State 2, an added volume from the voids is introduced to the total volume. The volume of the solid remains unchanged at its reference value since the material is unstressed in this configuration. This expression can be written as follows

$$V_2 = V_0 + V_V \tag{3.3}$$

Then, the damage, ϕ, can be defined as the ratio of the change in volume of an element in the elastically unloaded state (State 2) from its volume in the initial reference state to its volume in the elastically unloaded state

$$\phi = \frac{V_2 - V_0}{V_2} = \frac{V_V}{V_2} \tag{3.4}$$

Using this definition, Equation 3.2 can be written as

$$J = \det \underline{F}_V^P = \frac{1}{1-\phi} \tag{3.5}$$

Then, assuming that damage produces isotropic dilatation, the volumetric dilatation gradient can be determined by

$$\underline{F}_V^P = \frac{1}{(1-\phi)^{1/3}} \underline{I} \tag{3.6}$$

where $\underline{I}$ is the identity matrix.

The velocity gradient associated with the deformation gradient of Equation 3.1 is defined as

$$\underline{L} = \dot{\underline{F}}\,\underline{F}^{-1} \tag{3.7}$$

This velocity gradient can be expresses as

$$\underline{L} = \underline{L}^e + \underline{L}_V^p + \underline{L}_d^p \tag{3.8}$$

where the stretching or deformation and spin rates, $\underline{D}$ and $\underline{W}$ respectively, are defined as

$$\underline{D} = \frac{1}{2}\left(\underline{L} + \underline{L}^T\right) \tag{3.9}$$

$$\underline{W} = \frac{1}{2}\left(\underline{L} - \underline{L}^T\right) \tag{3.10}$$

The plastic volumetric rate of deformation is defined as

$$\underline{D}_V^P = \frac{\dot{\phi}}{3(1-\phi)} \underline{I} \tag{3.11}$$

The total deformation rate is expressed as (from3.8 and 3.9)

$$\underline{D} = \underline{D}^e + \underline{D}_V^P + \underline{D}_d^P \tag{3.12}$$

Thus, the damage parameter, ϕ, is related directly to the volumetric rate of deformation.

3.1.2 Kinetics: Elastic-Plastic Aspects

Assuming linear isotropic elasticity with respect to the natural configuration, taking the material derivative and moving forward to the current configuration, this assumption can be expressed as

$$\overset{\circ}{\underline{\sigma}} = \lambda(1-\phi)tr\left(\underline{D}^e\right)\underline{I} + 2\mu(1-\phi)\underline{D}^e - \frac{\dot{\phi}}{1-\phi}\underline{\sigma} \tag{3.13}$$

where λ is the Lamé constant, μ is the shear modulus, and the Cauchy stress $\underline{\sigma}$ can be obtained with the expression

$$\overset{\circ}{\underline{\sigma}} = \dot{\sigma} - \underline{W}^e\,\underline{\sigma} - \underline{\sigma}\underline{W}^e \tag{3.14}$$

From Equation 3.13, the elastic stretching can be written as

$$\underline{D}^e = \underline{D} - \underline{D}^P - \underline{D}^V \tag{3.15}$$

Bammann [1984] proposed a flow rule for the plastic deformation component of the total deformation rate, this rule is expressed as

$$\underline{D}_d^P = \sqrt{\frac{3}{2}}\,f(T)\sinh\left[\frac{\sqrt{\frac{3}{2}}\left\|\underline{\sigma}' - \sqrt{\frac{2}{3}}\underline{\alpha}\right\| - \{R + Y(T)\}\{1-\phi\}}{V(T)\{1-\phi\}}\right]\frac{\underline{\sigma}' - \sqrt{\frac{2}{3}}\underline{\alpha}}{\left\|\underline{\sigma}' - \sqrt{\frac{2}{3}}\underline{\alpha}\right\|} \tag{3.16}$$

where $\underline{\sigma}'$ is the deviatoric Cauchy stress, $\underline{\alpha}$ is a tensor variable and R is a scalar variable. Two internal state variables are present in the expression above, $\underline{\alpha}$ which is the kinematic hardening ISV and R which is the isotropic hardening ISV. The functions *f(T)*,

Y(T) and *V(T)* are related to yielding with Arrhenius-type temperature dependence. The temperature dependence of these variables will be explained in later paragraphs.

The internal state variables $\underline{\alpha}$ and *R*, are given by

$$\overset{\circ}{\underline{\alpha}} = \dot{\underline{\alpha}} - \underline{W}^e\,\underline{\alpha} + \underline{\alpha}\underline{W}^e = h(T)\underline{D}_d^P - \left[\sqrt{\frac{2}{3}}r_d(T)\left\|\underline{D}_d^P\right\| + r_s(T)\right]\sqrt{\frac{2}{3}}\|\underline{\alpha}\|\underline{\alpha} \tag{3.17}$$

$$\overset{\circ}{R} = H(T)\sqrt{\frac{2}{3}}\left\|\underline{D}_d^P\right\| - \left[\sqrt{\frac{2}{3}}R_d(T)\left\|\underline{D}_d^P\right\| + R_s(T)\right]R^2 \tag{3.18}$$

where *h(T)* represents the anisotropic hardening modulus and *H(T)* represents the isotropic hardening modulus. The variables r_s and R_s are scalar and describe the vacancy diffusion controlled static or thermal recovery, and r_d and R_d are scalar functions that describe the dynamic recovery.

The function *f(T)* determines when the rate dependence affects the initial yielding, *Y(T)* is the rate-independent yield stress and *V(T)* determines the magnitude of rate dependence on yielding. These functions can be determined from simple compression or tension tests with different strain rates and temperatures and are given by

$$V(T) = C_1 \exp\left(\frac{-C_2}{T}\right) \tag{3.19}$$

$$Y(T) = C_3 \exp\left(\frac{C_4}{T}\right) \tag{3.20}$$

$$f(T) = C_5 \exp\left(\frac{-C_6}{T}\right) \tag{3.21}$$

where C_1 through C_6 represent material properties.

The equations for hardening and recovering variables, R_s, r_s, R_d and r_d, are the following

$$r_d(T) = \left\{ C_7 \left(1 - C_{19} \left[\frac{4}{27} - \frac{J_3^2}{J_2^3} \right] - \right) \right\} \exp\left(\frac{-C_8}{T} \right) \tag{3.22}$$

$$h = \left\{ C_9 \left(1 + C_{20} \left[\frac{4}{27} - \frac{J_3^2}{J_2^3} \right] \right) \right\} \exp\left(\frac{-C_{10}}{T} \right) \tag{3.23}$$

$$r_s(T) = C_{11} \exp\left(\frac{-C_{12}}{T} \right) \tag{3.24}$$

$$R_d(T) = \left\{ C_{13} \left(1 - C_{21} \left[\frac{4}{27} - \frac{J_3^2}{J_2^3} \right] \right) \right\} \exp\left(\frac{-C_{14}}{T} \right) \tag{3.25}$$

$$H = \left\{ C_{15} \left(1 + C_{22} \left[\frac{4}{27} - \frac{J_3^2}{J_2^3} \right] \right) \right\} - C_{16} T \tag{3.26}$$

$$R_s(T) = C_{17} \exp\left(\frac{-C_{18}}{T} \right) \tag{3.27}$$

where C_7 to C_{22} represent material properties, and indexes *d* and *s* refer to dynamic and static respectively. The terms J_2 and J_3 are second and third deviatoric stress invariants and can be obtained by $J_2 = \frac{1}{2}\left(\underline{\sigma}' - \underline{\alpha}\right)^2$ and $J_3 = \frac{1}{3}\left(\underline{\sigma}' - \underline{\alpha}\right)^3$. The deviatoric stress $\underline{\sigma}'$ is expressed in indicial notation as $\sigma'_{ij} = \sigma_{ij} - \frac{1}{3}\sigma_{kk}\delta_{ij}$.

3.1.3 Damage Parameters. Void Nucleation, Growth and Coalescence

Engineering alloys fracture in a ductile manner when the pores or voids in the material nucleate, grow and coalesce. Figure 3.2 shows the damage framework that is limited to single void growth or void nucleation. Two different types of void coalescence are shown in Figure 3.3.

Figure 3.2. Damage framework with limiting cases of single void growth in (a) and by void nucleation.

The damage state of a material can be described in terms of void growth and nucleation [Horstemeyer and Gokhale, 1999]. The total damage evolution can be expressed as follows [Horstemeyer, 2000]

$$\phi = C\left(\phi_{pore} + \phi_{part}\right) \tag{3.28}$$

where C is a coalescence factor, ϕ_{pore} is the term related to the damage caused by voids nucleated from pre-existing pores and ϕ_{part} is the damage caused by void nucleated from inclusion particles and is expressed by

$$\phi_{part} = \eta \nu \tag{3.29}$$

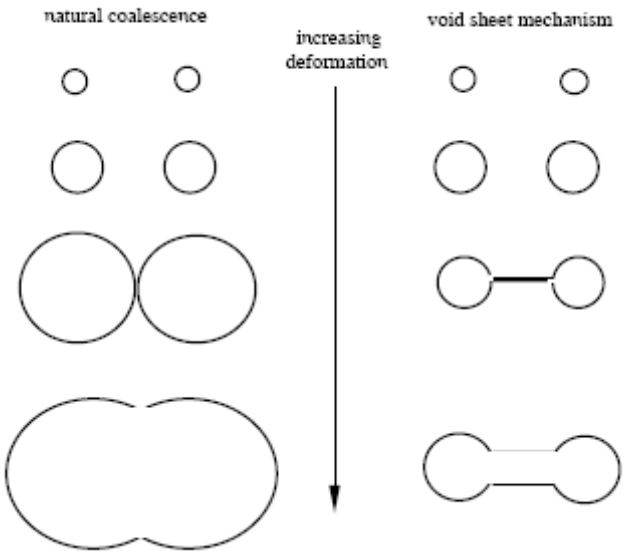

Figure 3.3. Two different void coalescence mechanisms observed in different materials

The term η in the expression above is the nucleation factor, defined as the number of pores nucleated per unit volume, and ν is the average of particles that have nucleated a void.

The void nucleation evolution equation is a function of a length scale parameter, stress state, strain rate and volume fraction of second phase materials. The void nucleation evolution is given by

$$\eta(T) = C_{coeff} \exp\left(\frac{\varepsilon(t) d^{1/2}}{K_{IC} f^{1/3}} \left\{ a\left[\frac{4}{27} - \frac{J_3^2}{J_2^3} \right] + b\frac{j_3}{J_2^{3/2}} + c\left\| \frac{I_1}{\sqrt{J_2}} \right\| \right\} \right) \exp\left(\frac{C_{T\eta}}{T} \right) \qquad (3.30)$$

where $\eta(T)$ is the void nucleation density, $\varepsilon(t)$ is the strain rate, C_{coeff} is a material constant and $C_{T\eta}$ is the temperature dependent material constant determined from experiments. The terms *a*, *b* and *c* relate to the volume fraction of nucleation events in the

material, f is the volume fraction of second phase particles and J_2 and J_3 are the second and third invariants of the deviatoric stress. The fracture toughness K_{IC} and the second phase particle size, d, are also included in this expression.

The damage state is also affected by void growth. McClintock [McClintock, 1968] proposed a void growth rule that is given by

$$\nu_v = \frac{4}{3}\left(R_0 \exp\left[\varepsilon(t) \frac{\sqrt{3}}{2(1-n)} \sinh\left(\sqrt{3}(1-n) \frac{\sqrt{2} I_1}{3\sqrt{J_2}} \right) \right] \right)^3 \tag{3.31}$$

where R_0 is the initial void radius, $\varepsilon\ (t)$ is the accumulated strain over the period of time t, and n is the strain-hardening exponent. In the expression above, void volume grows as the strain or/and the stress triaxiality increases. This model allows voids to grow in tension, but not in compression or torsion which complies with physical observations.

The damage caused by pre-existing voids, ϕ_{pore}, is modeled using the Cocks-Ashby model that is given in terms of void volume fraction rate

$$\dot{\phi}_{pores} = \left[\frac{1}{\left(1-\phi_{pores}\right)^m} - \left(1-\phi_{pores}\right) \right] \sinh\left\{ \frac{2(2m-1)\sigma_H}{(2m+1)\sigma_{vm}} \right\} \left\| D_d^p \right\| \tag{3.32}$$

where m is a material constant determined by $V(T)/Y(T)$.

The last term of Equation 3.29 (total damage), is the coalescence term C. This term arises with the multiplicative relation between nucleation and growth. Coalescence causes a discontinuity in the nucleation and growth evolution but allows for continuous

growth of total damage evolution, ϕ [Horstemeyer, 2000]. Thus, coalescence can be expressed as follows in a phenomenological manner

$$C = \left[C_{D1} + C_{D2}\eta\nu\right]\left(\frac{DCS_0}{DCS}\right)^Z \left(TC_{TC}\right) \tag{3.33}$$

where C_{D1}, C_{D2} and C_{TC} are material constants and DCS_0/DCS introduces the effect of grain size. The parameter Z normalizes the effect of DCS.

3.2. Material Constants

The plasticity model explained in the section above, proposed by Bammann, Chiesa and Johnson and then modified by Horstemeyer, requires a total of 53 material constants that can be determined from tension, compression, torsion and microstructure analysis experiments.

Mfit is a utility for fitting constants to material models for stress-strain data and fatigue life data. This fitting tool was developed at the Center for Advanced Vehicular Systems (CAVS) to make the task of finding 53 material constants more feasible. Mfit source code works with MATLAB subroutines to iterate and find the best constants fit for the equations. Once the constants are found, the model needs to be correlated using a finite element code. This process is described in the following sections.

3.2.1 Model Parameters in Mfit

A short explanation of the fitting process of the model to the experimental data, followed in this study, is given next.

With the experimental results presented in Chapter 2, the parameters necessary to define the ISV model explained in the section before can be found. A detailed list with the explanation of every constant is given in the Appendix.

Material tension data is comprised by an elastic part and a plastic part (refer to Chapter II). To begin, the experimental data is brought to the Mfit program to start the fitting process. The elastic part of the curve has to be described by introducing material mechanical properties as Young's modulus, Poisson ratio, and experimental conditions as strain rate and temperature. The microstructure properties are then specified in the model since most of the model parameters are affected by these properties. The microstructure properties that have an effect the material behavior are grain size, particle size, particle area fraction, and void size and area fraction. Figure 3.4 shows an Mfit window with the experimental data at two different temperatures of the front bumper material.

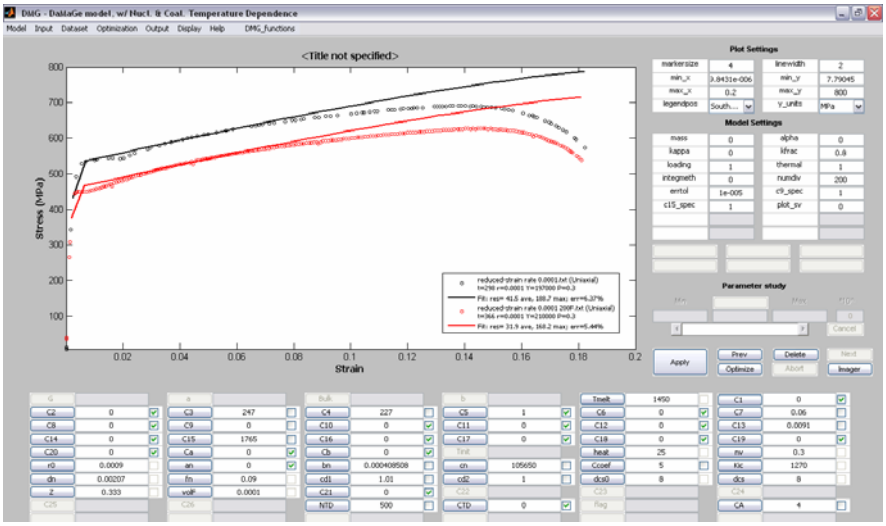

Figure 3.4. Mfit program with BCJ model constants. Front bumper tension experimental data at two different temperatures.

The plastic part of the material is governed by the yield parameters *f(T)*, *Y(T)* and *V(T)*; the hardening parameters h and H; and the recovery parameters *rs(T)*, *Rs(T)*, *rd(T)* and *Rd(T)*. The fitting process to obtain these parameters starts by setting *Y(T)*, which is the rate-independent yield parameter.

The hardening of the material can be isotropic or kinematic, or a combination, depending on the Baushinger[1] effect. If isotropic hardening is chosen, by example, the model parameter *h* can be set to zero, as well as parameters $r_d(T)$ and $r_s(T)$. This hardening type selection will reduce the constants to fit making the process easier. Recovery can also be neglected completely ($R_d(T)$ and $R_s(T)$ equal to zero) depending on the type of stress-strain curve of the material.

An approximation to parameter *H* can be obtained from the experimental data by obtaining the slope in the plastic section of the stress – strain curve, which will give an

[1] Phenomenon by which plastic deformation increases yield strength in the direction of plastic flow and decreases it in other directions [*Metals Handbook, Ninth Edition, Volume 8: Mechanical Testing. American Society for Metals]*

approximation to constant C_{15} from equation 3.26 (with no temperature dependence considered yet). The parameter *Rd* can also be approximated from this result, which will give a close value for constant C_{13}.

The rest of the constants can be obtained by *optimizing* in the Mfit tool until the model curve approaches to the experimental curve. The same process is followed to obtain the temperature and rate dependent constants.

Once the material constants are obtained, the model behavior has to be correlated in the simulation software as will be explained in the following section.

3.2.2 Material Model Correlation

All the analyses were performed in the finite element code Abaqus®. The validity of the material model constants obtained with Mfit can be correlated using only a unit cell cube (Figure 3.9) rather than a complete tension specimen. By doing this, the same results are obtained but the processing time is significantly reduced.

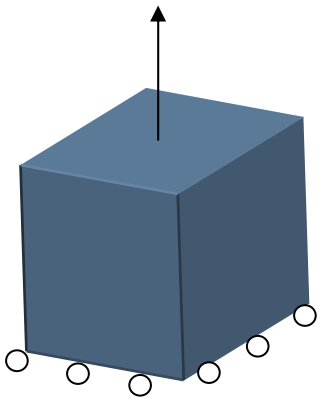

Figure 3.5. Unit cell used to correlate material model under tension conditions.

3.2.3 Front Bumper Material Model Correlation

The Dodge Neon bumper material constants at two different temperatures at the same strain rate (10^{-4} s^{-1}) were found with Mfit and correlated using Abaqus. The tension curves of the model and experiments are shown in Figure 3.10. The front bumper material constants can be found in the Appendix.

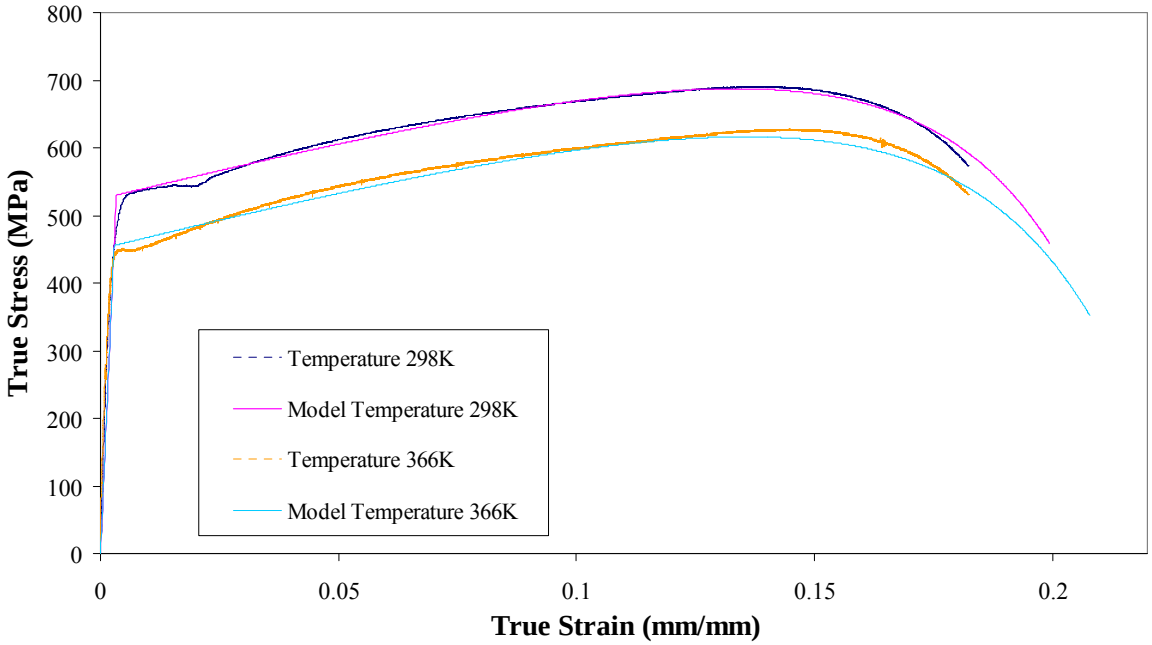

Figure 3.6. Front bumper tension curves showing the material model and experimental data.

The material model predicts accurately the experimental tension data. The damage can also be obtained from the Abaqus simulations as shown in Figure 3.7.The pore volume fraction at the failure point represents the damage of the material. For this case, the predicted damage of the material was 0.59 Pores/unit volume.

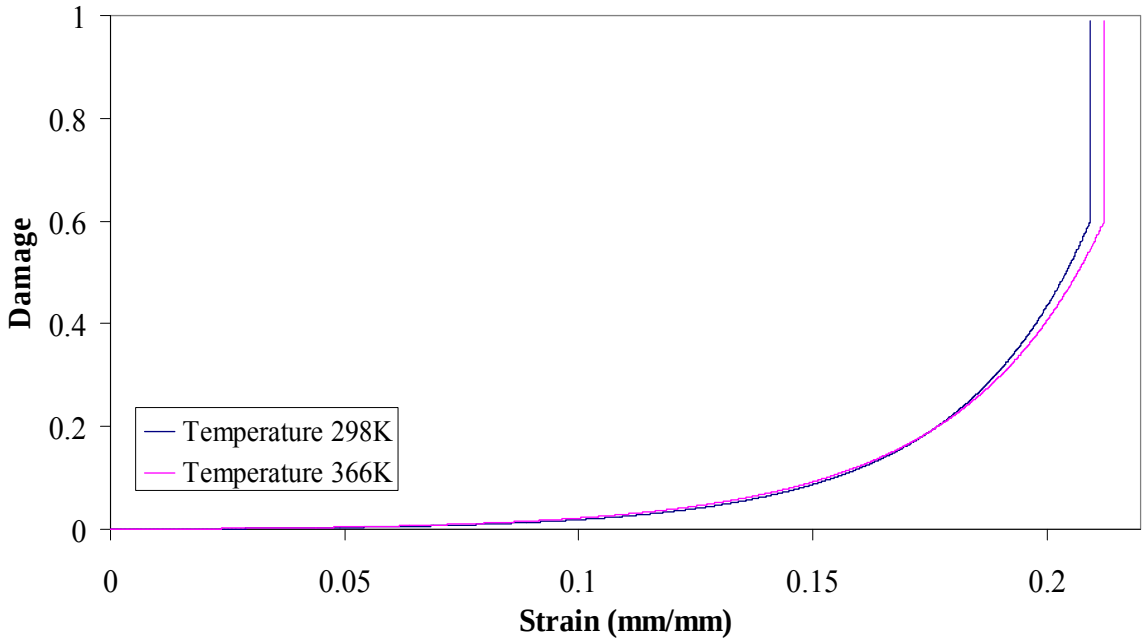

Figure 3.7. Front bumper damage curves from Abaqus simulations at two different temperatures.

CHAPTER IV

CONCLUSIONS AND RECOMMENDATIONS

Mechanical testing and microstructure analyses were performed in eight different Dodge Neon vehicle components. The material response of the front bumper was modeled using an Internal State Variable plasticity model that incorporates microstructure properties.

Different microstructure-properties were found for each vehicle component studied. For each component and its microstructure, a corresponding response o behavior under uniaxial tension was obtained. The tension tests showed strain rate and temperature dependence of the yield point clearly visible in the true stress – true strain curves. Very fine ferrite grain microstructures presented higher strength (yield strength) than other microstructures. This finding corresponds to the information found in the literature. Grain size distribution in the different components analyzed did not vary significantly between sites where the samples were extracted. However, some variations in the stress-strain behavior depending on location were observed. The difference in the behavior of the material depending on the location in the vehicle component affects the response during a crash.

Most of the materials characterized were found to be either microalloyed steel or bake-hardening steel. From literature, it was found that these types of steels are widely

used in automotive industry for body-in-white components such as suspensions and chassis, and closures such as outer doors, trunk lids and hoods.

Due to restrictions in material availability, more tension experiments could not be performed. In some cases, as in the rear floorboard, more high temperature experiments should be performed in order to corroborate and correct possible erroneous stress- strain responses. A deeper microstructure analysis is also recommended in order to obtain better understanding of precipitates and their composition.

New chemical composition analysis on the vehicle components are also recommended since some microstructures did not correspond to the chemical composition obtained. This issue was attributed to human errors during the execution of the spectrometries.

The yield strength found from mean Vickers hardness using equations, were in the same order of magnitude than the experimental result from stress –strain curves. However, these calculated values from hardness differed from the actual experimental values. It is important to mention that human errors could modify the actual reading of the indentation dimension, giving incorrect Vickers hardness and therefore incorrect yield values.

Plasticity constants of the front bumper material were found using the experimental results. The material model was correlated using finite element simulations in Abaqus. Uniaxial tension response was obtained and compared to the experimental true stress – true strain curve. The plasticity model predicted satisfactorily the front bumper material behavior under tension.

In future work, the correlated front bumper material model obtained in this research will be implemented in a full vehicle model. A crash simulation using this microstructure-based model will be performed to compare the model response with actual crash data. It is expected that both, the simulation and actual crash data behavior, present similar responses.

REFERENCES

Abaqus/Explicit User's Manual, Hibbitt, Karlsson & Sorensen, Inc. 2002

AISI, "Automotive Steel Design Manual", Rev. 6.1, American Iron and Steel Institute and Auto/Steel Partnership, Southfield, MI, 2002.

ASM Handbook, "Materials Characterization", Vol. 10, American Society for Metals, 2005.

ASM Specialty Handbook, "Carbon and Alloy Steels", American Society for Metals, 1996.

ASTM Standards, "Section 3: Metals test methods and analytical procedures", v. 03.01, American Society of Testing and Material, West Conshohocken, PA, 2000.

Avallone, E.A., Baumeister, T, "Mark's Standard handbook for mechanical engineers (10th Edition)", McGraw Hill, 1996.

Avner S., "Introduction to Physical Metallurgy", McGraw Hill, New York, 1988.

Bammann D. J., "An internal variable model of viscoplasticity", *Int. J. Eng. Sci*., v. 22, No.8-10, 1984, pp. 1041 – 1053.

Bammann D. J., "Modeling temperature and strain rate dependent large deformations of metals", ASME *Appl. Mech. Rev*., v. 43, No. 5, Part 2, 1990, pp. S312-S319.

Bammann D. J., Aifaintis E. C., "A damage model for ductile metals", *Nuc. Eng. & Des*., v. 116, 1989, pp. 355 – 362.

Bammann D. J., et al., "Failure in ductile materials using finite element methods", *Struc. Crashworhtiness and Failure*, Elsevier, London and New York, 1993.

Bhadeshia H., Honewcombe R., "Steels: Microstructure and Properties", Butterworth-Heinemann, London, 2006.

Cahoon J. R. et al., "Determination of yield strength from hardness measurements", *Met. Trans*. (2), 1971, pp. 1979 – 1983.

Cocks A. C. F., Ashby, M. F., "On creep fracture by void growth", *Prog. Mater. Sci*., v. 27, 1982, pp. 189 – 244.

Davies G., "Materials for automotive bodies", Elsevier, 2003.

Dieter G., "Mechanical Metallurgy", McGraw Hill, 3rd Edition, 1986.

Hamza K., Saitou K., "Design optimization of vehicle structures for crashworthiness using equivalent mechanism approximations", *J. Mech. Des*., v. 127, 2005, pp. 485 – 492.

Horstemeyer M. F., "From Atoms to Autos. A New Design Paradigm Using Microstructure-Property Modeling. Part 1: Monotonic Loading Conditions", *Sandia Nat. Labs*., Intern. Report SAND2000-8662, 2001

Horstemeyer M. F, Gokhale A. M., "A void-crack nucleation model for ductile metals", *Int. J. Solids and Struc*. 36, 1999, pp. 5029-5055.

Horstemeyer M. F. et al., "Modeling stress state dependent damage evolution in a cast Al-Si-Mg aluminum alloy", *Theo. & App. Fract. Mech.* 33, 2000, pp. 31-47.

Lathrop J. F., "BFIT – A program to analyze and fit the BCJ model parameters to experimental data. Tutorial and user's guide", *Sandia Nat. Labs*, Internal Report SAND 97-8218, 1996.

Lee E.H., "Elastic-plastic deformations at finite strains", *ASME J. Appl. Mech.*, v 36, 1969, pp. 1-6.

Máthis K, Rauch E.F., "Microstructural characterization of a fine-grained ultra low carbon steel", *Mat. Sci. & Eng.*, A 462, 2007, pp. 248-252.

McClintock F. A., "A criterion for ductile fracture by void growth of holes", ASME, J. *Appl. Mech.*, v. 35, 1968, pp. 363 - 371.

Roylance D., "Finite Element Analysis", *Dept. of Mat. Sci. and Eng. MIT*, Cambridge, 2001.

Simulia, "Abaqus Unified FEA. Complete Solution for Realistic Simulation", 2008.

Tabor D., "Hardness of metals", Oxford, 1951.

Ugural A.C., Fenster S.K., Advanced Strength and Applied Elasticity, 3rd ed, Prentice Hall, 1995.

Van Slycken J., Verleysen P., Degrieck J., "Crashworthiness characterization and modeling of high-strength steels for automotive applications", *Proc. IMechE v.220 Part D: J. Automobile Eng.*, 2006, pp. 391 – 400.

Zaouk A.K., Marzougui D., and Bedewi N.E., "Development of a Detailed Vehicle Finite Element Model, Part I: Methodology," *IJCrash*, 5-1, 2000, pp. 25-35

Zaouk A.K., Marzougui D., and Kan C.D., "Development of a Detailed Vehicle Finite Element Model, Part II: Material Characterization and Component Testing," *IJCrash*, 5-1, 2000, pp. 37-50.

APPENDIX A

FRONT BUMPER MATERIAL CONSTANTS

Table A.1

Front bumper plasticity constants at room temperature

Material Constant	Value	Description
C3	530	Constant term in Y(T)
C13	0.0091	Constant term in Rd(T)
C15	1740	Constant term in H
cn	5.50E+05	Triaxiality constant in nucleation model
Ccoef	5	Coefficient constant in nucleation model
NTD	500	Nucleation Temperature Dependence
nv	0.3	McClintock damage constant
r0	0.0002	Initial void radius
Kic	1270	Fracture toughness
dn	0.0005	Average size of particles
fn	0.06	Particles volume fraction related to nucleation
dcs	8	Reference grain size or dendrite cell size
dcs0	8	Grain size or dendrite cell size
volF	0.0001	Initial void volume fraction
G	75769	Shear modulus

Table A.2

Front bumper plasticity constants at 366K

Material Constant	Value	Description
C3	248	Constant term in Y(T)
C4	227	Temperature dependent term in Y(T)
C13	0.0091	Constant term in Rd(T)
C15	1770	Constant term in H
cn	5.43E+05	Triaxiality constant in nucleation model
Ccoef	5	Coefficient constant in nucleation model
NTD	500	Nucleation Temperature Dependence
nv	0.3	McClintock damage constant
r0	0.0002	Initial void radius
Kic	1270	Fracture toughness
dn	0.0005	Average size of particles
fn	0.06	Particles volume fraction related to nucleation
dcs	8	Reference grain size or dendrite cell size
dcs0	8	Grain size or dendrite cell size
volF	0.0001	Initial void volume fraction
G	80384	Shear modulus

APPENDIX B

CONTROLLED ROLLING PROCESS AND HIGH STRENGTH LOW ALLOY STEELS

Controlled rolling is a procedure in which the various stages id rolling are temperature controlled, with the amount of reduction in each pass predetermined and the finishing temperature precisely defined. Controlled rolling is used in microalloyed steels to provide optimal mechanical properties at room temperature [ASM Specialty Handbook, 1996].

The use of controlled rolling has resulted in improved combinations of strength and toughness and further reductions of carbon content of microalloyed HSLA steels. This reduction in carbon content improves toughness and weldabilty [ASM Specialty Handbook, 1996].

The basic objective of controlled rolling is to refine austenite grains during the rolling process so fine ferrite grains are produced during cooling. During hot rolling, the undissolved carbonitrides of vanadium and niobium pin austenite grain boundaries and therefore retard the austenite grain growth [ASM Specialty Handbook, 1996].

In microalloyed steels, carbides and carbonitrides of Nb, Ti, and V will precipitate progressively during controlled rolling as the temperature falls. The primary effect of these dispersions is control grain size, but dispersion strengthening will also take place [Bhadeshia and Honeycombe, 2006]

There are three different controlled rolling methods:

- Conventional controlled rolling
- Recrystallization controlled rolling
- Dynamic recrystallization controlled rolling

Conventional controlled rolling is based on the deformation (pancaking) of austenite grains. Recrystallization controlled rolling is used for thicker sections and

involves recrystallization of austenite at successively low temperatures. Dynamic recrystallization controlled rolling is used when there is insufficient time for recrystallyzation between rolling passes.

The general process of controlled rolling is summarized in Figure B.1

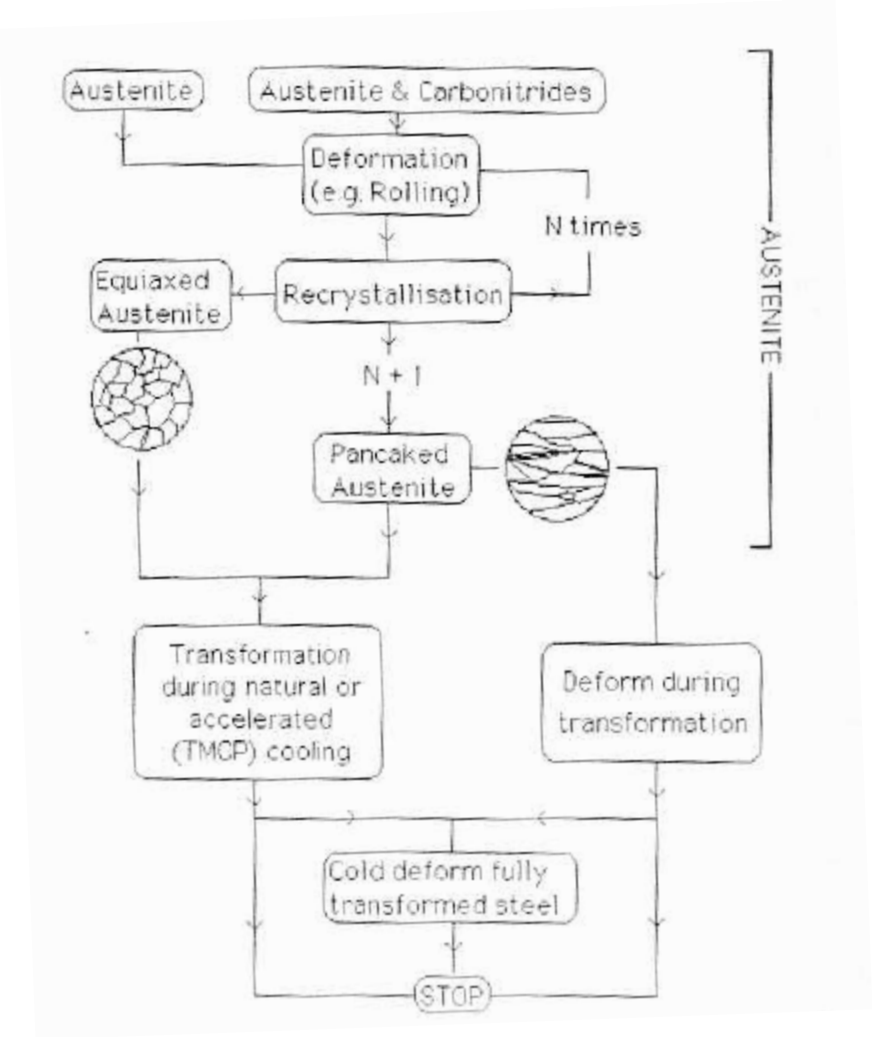

Figure B.1. Controlled rolling process.